[redacted]

Radiative transfer modeling in the coupled atmosphere-ocean system and its application to the remote sensing of ocean color imagery

by

Banghua Yan

RECOMMENDED:

Dr. John Olson

Dr. Brenton Watkins

Dr. Hans Nielsen

Dr. Knut Stamnes, Chairman, Advisory Committee

Dr. Brenton Watkins, Head, Physics Department

APPROVED:

Dr. David M. Woodall, Dean of CSEM

Dr. Joseph Kan, Dean of the Graduate School

5-6-01

Date

Radiative transfer modeling in the coupled atmosphere-ocean system and its application to the remote sensing of ocean color imagery

A

THESIS

Presented to the Faculty

of the University of Alaska Fairbanks

in Partial Fulfillment of the Requirements

for the Degree of

DOCTOR OF PHILOSOPHY

By

Banghua Yan, B.S., M.S.

Fairbanks, Alaska

August 2001

Abstract

Ocean color is the radiance emanating from the ocean due to scattering by chlorophyll pigments and particles of organic and inorganic origin. Thus, it contains information about chlorophyll concentrations which can be used to estimate primary productivity. Observations of ocean color from space can be used to monitor the variability in marine primary productivity, thereby permitting a quantum leap in our understanding of oceanographic processes from regional to global scales. Satellite remote sensing of ocean color requires accurate removal of the contribution by atmospheric molecules and aerosols to the radiance measured at the top of the atmosphere (TOA). This removal process is called "atmospheric correction". Since about 90% of the radiance received by the satellite sensor comes from the atmosphere, accurate removal of this portion is very important. A prerequisite for accurate atmospheric correction is accurate and reliable simulation of the transport of radiation in the atmosphere-ocean system. This thesis focuses on this radiative transfer process, and investigates the impact of particles in the atmosphere (aerosols) and ocean (oceanic chlorophylls and air bubbles) on our ability to remove the atmospheric contribution from the received signal. To explore these issues, a comprehensive radiative transfer model for the coupled atmosphere-ocean system is used to simulate the radiative transfer process and provide a physically sound link between surface-based measurements of oceanic and atmospheric parameters and radiances observed by satellite-deployed ocean color sensors. This model has been upgraded to provide accurate radiances in arbitrary directions as required to analyze satellite data. The model is then applied to quantify the uncertainties associated with several commonly made assumptions invoked in atmospheric correction algorithms. Since atmospheric aerosols consist of a mixture of absorbing and non-absorbing components that may or may not be soluble, it

becomes a challenging task to model the radiative effects of these particles. It is shown that the contribution of these particles to the TOA radiance depends on the assumptions made concerning how these particles mix and grow in a humid environment. This makes atmospheric correction a very difficult undertaking. Air bubbles in the ocean created by breaking waves give rise to scattered light. Unless this contribution to the radiance leaving the ocean is correctly accounted for, it would be mistakenly attributed to chlorophyll pigments. Thus, the findings in this thesis make an important contribution to the development of an adequate radiative transfer model for the coupled atmosphere-ocean system required for development and assessment of algorithms for atmospheric correction of ocean color imagery.

Contents

List of Figures

Acknowledgments

I would like to thank Professor Knut Stamnes, chairman of my graduate advisory committee. Through my entire graduate studies, Dr. Stamnes has given me continual support, warm encouragement and excellent guidance. I have benefited a lot from his academic insights into scientific issues, as well from his academic guidance. My sincere thanks are also extended to other members of my graduate advisory committee: Dr. John Olson, Dr. Brenton Watkins, Dr. Hans Nielsen. A lot of valuable comments and suggestions about the revision of the thesis come from them.

I thank the physics department for its strong mathematical and physical education. Special thanks are due to Dr. Jerry Harrington and Dr. Glenn Shaw and Dr. Peter Olson for the valuable insights they provided into the physics and mathematics of atmospheric science during the courses I took as part of my graduate education. My sincere thanks are due to Dr. Bingquan Chen for his valuable suggestions and discussions through the entire graduate studies. Thanks are also due to Ms. Wei Li for her valuable discussions and cooperation through the entire graduate studies. Thanks are due to Dr. Jakob Stamnes for his valuable discussions and suggestions for the research of the thesis, and to Dr. Sichee Tsay for his valuable discussions on aerosol issues.

I thank Dr. Fuzhong Weng for his understanding and for his supporting my work on the thesis while working on his project about microwave remote sensing of land emissivity which is totally different from the thesis. Without his kindness and encouragement, it would be very difficult for me to finish the thesis in such a short time. Thanks are due to Mr. Karl Idar Gjerstad for his cooperation in comparison between the DISORT and MC codes. I am grateful to the international student advisor, Ms. Marilynn Griffin, the secretary of the physics department,

Ms. Norma Pfeiffer, for their constant help with practical issues related to my graduate studies. Thanks are extended to my fellow graduate students, Xiaozhen Xiong, Qiuqing Zhang, Hans Eide, Jennifer Delamere, Rune Storvold, F. M. Schulz and to many other friends for their help.

For my family, I am especially grateful to my dear husband, Songhu Yan, for his continual support of my hard work on the thesis during most of my spare time during the past nearly two years; to my very lovely and thoughtful daughter, Nanfei Yan, for her understanding and support during my hard studies on the thesis. It is this invaluable support from my family that encourages me to finish my thesis. I would like to thank my parents, and my oldest sister, Yanjun Huang, and my oldest brother-in-law, Mingyuan Wei, for their constant support for my graduate studies. Without their support, it is impossible for me to arrive at this thesis.

The success of this thesis is due to the support and encouragement from all of my committee members, from my many friends, from many members of my big family. I would like to dedicate this thesis to whoever helped and supported me.

Chapter 1

Introduction

1.1 Historical perspective of the satellite remote sensing of the ocean color

The ocean color is the radiance emanating from the ocean due to scattering by phytoplankton, sediments, and dissolved organic matter. Phytoplankton consists of small, single-celled ocean plants. These plants consitute the base of the oceanic food web and produce organic carbon through photosynthesis. Phytoplankton contains chlorophyll *a* (the dominant photosynthetic pigment) which absorbs strongly in the blue and red regions of the visible spectrum [1]; this process provides the energy needed for photosynthesis and production of organic carbon. The rate at which photosynthesis proceeds is known as primary productivity. Different types of phytoplankton that contains different concentrations of chlorophyll have the effect of changing the color of water to green hues from the deep blue of its pure state so that oceans appear as different colors to sensitive satellite instruments. Thus, the observation of ocean color reveals the variability in the distribution and concentration of phytoplankton and the extent of primary productivity, and there-

fore permits a quantum leap in our understanding of oceanographic processes from regional to global scales. Satellite observations provide the rapid, global coverage required for studies of ocean productivity worldwide and play an important role in the remote sensing of ocean color.

The possibility of remote sensing of ocean color was first recognized early in 1970 by Clark, Ewing and Lorenzen [1] who showed that the chlorophyll concentration in the surface waters of the ocean could be deduced from aircraft measurements of the spectrum of upward light from the sea. This work led the National Aeronautics and Space Administration (NASA) in 1972 to begin aircraft investigations to determine whether useful ocean color measurements could be made from spacecraft, whether ocean color could be detected through the scattering atmosphere, and whether other interfering effects, such as the direct specular reflectance of the sun (glint) from the water surface, could be avoided or corrected for [2, 3]. The results were sufficiently encouraging that in 1973 NASA agreed to fly an ocean color sensor, to be called the Coastal Zone Color Scanner (CZCS), on Nimbus-G, which was scheduled for launch in 1978. The CZCS Experiment, a "proof-of-concept" experiment, used a conventional multi-channel scanning radiometer devoted to the measurement of ocean color [4]. The CZCS contained four bands in the visible at 443, 520, 550 and 670 nm with bandwidths of 20 nm, one band in the near-infrared (NIR) at 750 nm with a bandwidth of 100 nm, and a thermal infrared band (10.5 to 12.5 μm) to measure sea surface temperature. The algorithm for atmospheric correction in CZCS was based upon the single scattering approximation [5] although we know that this approximation is valid only when the atmosphere is pretty clear and the aerosol concentration is low. It was shown that satellite ocean color measurements could be reliably used to derive products such as chloroplyll and sediment concentrations. This provided justification for future ocean color missions such as the Sea-viewing Wide Field-of-view Sensor (SeaWiFS) and the

Moderate Resolution Imaging Spectrometer (MODIS) [6].

The algorithms developed to analyze CZCS data were a considerable step forward from those available earlier and included corrections for atmospheric backscatter, limb brightness and "gelbstoffe" [6]. As there were no NIR bands in CZCS (except for the broad band channel at 750 nm), the atmospheric correction algorithm relied on the channel at 670 nm where the water-leaving radiance is assumed to be zero. This assumption of zero water-leaving radiance is thought to be valid only when the chlorophyll concentration is low enough. Nevertheless, CZCS demonstrated the need for good radiometric sensors and more reliable algorithms for atmospheric correction. With the recent and upcoming launch of new sensors with improved spectral resolution a new era in ocean color remote sensing is arriving. These new sensors include SeaWiFS launched aboard the SeaStar satellite in 1997, MODIS launched by NASA in 2000, MERIS to be launched on ENVISAT by the European Space Agency (ESA) in 2001, and the upcoming Global Imager (GLI) aboard the Japanese Advanced Earth Observation Satellite II (ADEOS-II). SeaWiFS is a multi-channel scanning radiometer devoted to measurements of ocean color. It possesses a higher radiometric sensitivity as well as more bands in the visible and NIR regions than CZCS: 6 bands in the visible at 412, 443, 490, 510, 555 and 670 nm with bandwidths of 20 nm, and 2 bands in the NIR at 765 and 865 nm with bandwidth of 40 nm. Such characteristics of SeaWiFS make the remote sensing of the ocean color possible and realistic.

The optical properties of the ocean waters are tightly coupled to the abundance of pigments in algal cells. In many situations, phytoplankton species and their derivatives, detrital products (mainly particulate, but also dissolved), play a predominant role in determining the optical properties of oceanic waters. Such waters are classified as 'Case I' waters as opposed to 'Case II' waters for which sediments, or dissolved yellow substances, make an important or dominant con-

tribution to the optical properties [7, 79]. Open ocean waters, as a rule, form Case I waters. In the absence of terrigeneous influx (along arid coasts) and of resuspended sediments from the shelf, coastal waters can also, and often do, belong to Case I [79]. More than 98 % of the world ocean waters, ranging from oligotropic to locally eutrophic waters, are presumably of this category. This emphasizes the significance of understanding Case I waters. Thus, Case I ocean waters constitute the focus of our study below.

1.2 Development of algorithms for atmospheric correction of ocean color imagery

The retrieval of the ocean color is currently based on the following steps: 1) an aerosol model is selected from a suit of candidate aerosol models and a corresponding aerosol optical depth at NIR wavelengths is estimated; 2) the atmospheric contribution to the TOA radiance at visible wavelengths is extrapolated from the NIR wavelengths and removed from the satellite-measured radiance; 3) since the water-leaving radiance at visible wavelengths (ocean color) carries information about both absorption and scattering processes that can be used to infer the optical properties of the water, a suitable bio-optical model can then be used to convert the optical properties into other parameters of interest such as chlorophyll concentration, colored dissolved organic matter, and inorganic particle concentration. The combination of 1) and 2) is called atmospheric correction of ocean color imagery, a process aimed at quantifying and removing the contribution from atmospheric molecules and aerosols to the TOA radiances in the visible region. Thus, a key step in the retrieval of ocean color is to develop a reliable and accurate algorithm for atmospheric correction of ocean color imagery.

Away from both sun glitter and whitecaps, the satellite-observed reflectance at wavelength λ, $\rho_t(\lambda)$, can be written as [6]

$$\rho_t(\lambda) = \rho_{path}(\lambda) + t(\lambda)\rho_w(\lambda) \tag{1.1}$$

where t(λ) is the diffuse transmittance, $\rho_w(\lambda)$ is the reflectance resulting from the multiple scattering by oceanic chlorophyll species, and

$$\rho_{path}(\lambda) = \rho_r(\lambda) + \rho_a(\lambda) + \rho_{ra}(\lambda). \tag{1.2}$$

Here ρ_r is the reflectance resulting from multiple scattering by air molecules (Rayleigh scattering) in the absence of aerosols, ρ_a is the reflectance resulting from multiple scattering by aerosols in the absence of the air molecules, and ρ_{ra} is the interaction term between molecular and aerosol scattering. The reflectance is defined as the radiance normalized by the extraterrestrial solar irradiance, i.e. $\rho = \pi I / F_0 \cos\theta_0$, where I is the radiance, F_0 is the extraterrestrial solar irradiance, and θ_0 is the solar zenith angle.

Based upon this model, Gordon and his co-workers developed an operational algorithm for atmospheric correction of SeaWiFS ocean color imagery. This algorithm utilizes the black pixel assumption in the NIR, i.e., $\rho_w(\lambda_{NIR}) = 0.0$. Thus,

$$\rho_{path}(\lambda_{NIR}) = \rho_t(\lambda_{NIR}) \tag{1.3}$$

where λ_{NIR} is the wavelength in the NIR region, e.g., for the SeaWiFS sensor, λ_{NIR} = 765 or 865 nm.

Since this algorithm is based upon the CZCS algorithm in the single scattering approximation, it uses the ratio $\varepsilon_{ss}(\lambda_i, 865)$ determined by

$$\varepsilon_{ss}(\lambda, 865) = \rho_{as}(\lambda)/\rho_{as}(865) \tag{1.4}$$

where $\rho_{as}(\lambda)$ is the aerosol reflectance in the single scattering case.

To obtain the atmospheric contribution in the multiple scattering approximation, a second ratio $\kappa[\lambda, \rho_{as}(\lambda)]$, the ratio of the aerosol reflectance in the multiple scattering case to that in the single scattering case, is introduced

$$\kappa[\lambda, \rho_{as}(\lambda)] = \frac{\rho_a(\lambda) + \rho_{ra}(\lambda)}{\rho_{as}(\lambda)}. \tag{1.5}$$

Based upon these two ratios, an aerosol model and a corresponding aerosol optical depth are estimated from a group of values of these two ratios determined from a suit of candidate aerosol models [6] with some additional approximations (e.g., an exponential relationship of $\varepsilon_{ss}(\lambda, 865)$ is assumed between the visible and NIR regions). A flow chart of this atmospheric correction algorithm is shown in Fig. 1.1. In this figure, L_m is the radiance measured by satellite sensor at the top-of-atmosphere in presence of sun glitter and whitecaps; τ_{oz} is the optical depth due to ozone; P, W and T are the pressure, wind speed and temperature of sea surface, respectively; T_w is the water temperature and ΔT is the air-sea temperature difference (indicating the atmospheric stability); θ, Φ and θ_0 are the viewing, azimuthal and solar angle, respectively. More explanations about the variables in the figure can be found in reference [6].

This algorithm is expected to work well for cases where only weakly-absorbing aerosols are present over Case I waters. It plays a central role in the application of SeaWiFS imagery to the ocean, and it is also considered to be a prototype algorithm for MODIS. However, this algorithm has some limitations. It to assumed that over the wavelength range between 412 and 865 nm the coefficient $\varepsilon_{ss}(\lambda, 865)$, defined above as the single scattering aerosol reflectance ($\rho_{ss}(\lambda)$) at wavelength λ to that at 865 nm, can be considered to be an exponential function of (865-λ). Although this exponential relationship works well for the weakly-absorbing aerosols proposed by Shettle and Fenn [9], it is not valid for strongly absorbing aerosols. Also, the algorithm utilizes the ratio of aerosol reflectances at different wavelengths

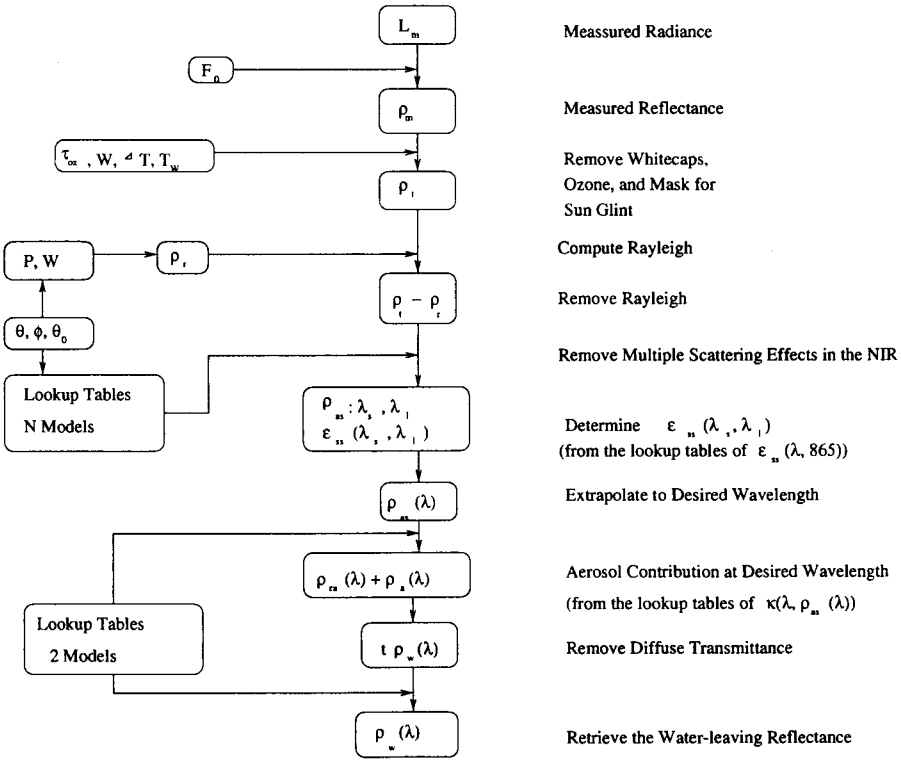

Figure 1.1 A flow diagram of the operational algorithm for atmospheric correction of SeaWiFS imagery developed by Gordon et al., where N models represent a group of candidate aerosol models (after Gordon, 1996) .

in the single scattering approximation to determine that pair of aerosol models that best account for the observed reflectances in the two near-infrared (NIR) bands. This pair is estimated by averaging the reflectances of all candidate pair of aerosol models, the so-called averaging method [6]. Our simulations show that this method may incur a large deviation of the estimated aerosol model from the actual aerosols in the presence of strongly absorbing aerosols.

To decrease the impact of such factors on the accuracy of atmospheric correction, a generalized algorithm for atmospheric correction was presented by Yan et al. [10]. This new algorithm utilizes $\varepsilon_{ms}(\lambda, 865)$, the ratio of the aerosol reflectance ($\rho_{ms}(\lambda)$) at wavelength λ to that at 865 nm in the presence of multiple scattering, and lookup tables of the $\varepsilon_{ms}(\lambda_{vis}, 865)$ instead of the exponential function of $\varepsilon_{ms}(\lambda, 865)$ in the range between 412 and 865 nm, where λ_{vis} is the wavelength in the visible region. For the SeaWiFS sensor, λ_{vis} = 412, 443, 490, 510, 555 nm. The simulation results show that this algorithm is effective in selecting a proper aerosol model, and effective in reducing the error to retrieve the water-leaving radiance at the visible wavelengths for both strongly-absorbing and weakly-absorbing aerosols for a given vertical distribution of the aerosol. Unfortunately, the vertical distribution of atmospheric aerosols is unknown. In this situation, it has been shown that an algorithm using either $\varepsilon_{ss}(\lambda, 865)$ or $\varepsilon_{ms}(\lambda, 865)$ will fail for strongly absorbing aerosols [11]. One important reason is that the $\epsilon_{ss}(\lambda, 865)$ or $\epsilon_{ms}(\lambda, 865)$ are sensitive to the vertical distribution of the aerosol in the visible bands but insensitive in the NIR bands. Optical properties of aerosols retrieved in the NIR bands fail to contain information about the vertical distribution of the aerosol, and this leads to a large error in the atmospheric correction in the visible bands due to uncertainty in the vertical distribution of the aerosol.

Antoine and Morel proposed a new ratio $\rho_{path}(\lambda)/\rho_r(\lambda)$ to do atmospheric correction of ocean color imagery [12, 13]. This ratio depicts the relative increase

in reflectance brought about by the progressive addition of aerosols within an atmosphere initially free from aerosols. Their simulations show that this algorithm is able to perform the correction for atmospheres containing several aerosol types, including absorbing ones, through their identification in the near-infrared, and through the detection of the absorption by means of appropriate assumptions about the marine signals at 510 and 705 nm. This ratio is not sensitive to the vertical distribution of the aerosol and thus leads to improved atmospheric correction in the visible bands.

These algorithms make some improvements in the estimation of the optical properties of strongly absorbing aerosols. However, when the chlorophyll concentration is sufficiently high, a serious problem exists due to the violation of the black-pixel assumption (BPA), according to which the water-leaving radiance (L_w) at near-infrared (NIR) wavelengths is negligible, because the BPA is widely used in all of the above atmospheric correction algorithms. At NIR wavelengths, the water-leaving radiance is proportional to the chlorophyll concentration, so when the chlorophyll concentration is sufficiently high, it is large enough so that its effect is non-negligible on atmospheric correction of ocean color. It has been known that the inappropriate application of the black pixel assumption is partly responsible for the excessively high chlorophyll observations made from SeaWiFS and for some of the observed underestimates of water-leaving radiance for the blue wavelengths [14]. It is obviously important to investigate the validity of this assumption. Chen et al. studied the validity of this assumption for different oceanic chlorophyll concetrations [15]. Simulated results show that for common open-ocean aerosol loadings (aerosol optical depth in the range 0.08-0.11) the water-leaving radiance at NIR wavelengths (e.g., 865 nm) is usually large enough that it cannot be ignored. The impact of the non-negligible values of water-leaving radiance at NIR wavelengths on atmospheric correction depends on (i) the magnitude of the chlorophyll particle

concentration; (ii) the particle types in the near-surface ocean water as well as their physical properties, such as the particle geometrical shape and its refractive index which in turn decide the particle phase function; (iii) the aerosol optical optical depth; and (iv) sun-satellite geometry. The simulations demonstrated a need for a new approach to atmospheric correction of ocean color imagery to obtain reliable and accurate results for open ocean waters when chlorophyll particle concentrations are sufficiently high or the aerosol optical depth is sufficiently small. Siegel et al. made an attempt to relax the BPA [16] for SeaWiFS imagery on the basis of a bio-optical model for the water-leaving reflectance derived from an empirical model for NIR remote sensing reflectance [17, 18, 19]. It was found that this approach led to a significant increase in the water-leaving reflectance for the violet and blue bands for chlorophyll concentrations larger than 2 $mg{\cdot}m^{-3}$ [16].

1.3 Uncertainties affecting the accuracy of the atmospheric correction of ocean color imagery

Progress is being made in the development of algorithms for atmospheric correction of ocean color imagery. However, it is still a vexing problem to develop a good algorithm for atmospheric correction of ocean color imagery because the algorithm needs to work in a large variety of atmospheric and oceanic situations: a large variation of atmospheric aerosols with time and space and a large variation of oceanic chlorophyll concentrations ranging from 0.01 and 100.0 $mg{\cdot}m^{-3}$ [21]. The high variability of atmospheric aerosols makes it a difficult and challenging problem to retrieve accurately the weak ocean color signal (a few of percent of the satellite-measured radiance [21]) from the satellite-measured radiance. A few percent error in the TOA reflectance in the NIR bands will lead to a non-negligible error in

the retrieval of ocean color. From the following analyses one will see that there are considerable uncertainties in the computation of optical properties of candidate aerosol models for use in retrieval of the aerosol model and optical depth. There are also many uncertainties associated with assumptions used in the current algorithms for atmospheric correction of ocean color imagery. These existing uncertainties would impair the accuracy of the atmospheric correction of ocean color imagery if the error caused by them are not properly corrected.

1.3.1 Accuracy of the optical properties of the candidate aerosol models

Current algorithms for atmospheric correction of ocean color imagery [6, 10, 11, 13, 22, 23] are commonly based on the use of reflected radiances at NIR wavelengths to identify an aerosol model and a corresponding optical depth from a suite of candidate models. These candidate models generally include 12 aerosol models used for non-absorbing or weakly absorbing aerosols, i.e., Coastal, Maritime, Tropospheric aerosols at relative humidity (RH) of 50, 70, 90 and 99 %, respectively, and 4 Urban aerosol models for strongly absorbing aerosols at RH of 50, 70, 90 and 99 %, respectively [9]. These 16 candidate aerosol models consist of several types of particles, each having its own characteristic chemical composition, size distribution and hygroscopicity [9]. The following questions then arise: How do we compute the optical properties of such a multi-component mixture of dry aerosol particles? And can we predict how these optical properties change with an increase in the humidity of the air in which the particles are suspended?

The computation of optical properties of candidate models in current algorithms for SeaWiFS imagery [6, 11, 13, 22, 23] are based on the approach constructed by Shettle and Fenn [9]. In order to save computational resources (com-

puters were much less powerful in the 1970's than today!), Shettle and Fenn decided to combine the different aerosol species into an effective single-component model by averaging the refractive indices of the multi-component aerosol mixture. This approach, which we shall refer to as the single-component (SC) approach below, seemed to be a reasonable choice at that time. To account for the change in optical properties with changing relative humidity Shettle and Fenn used the SC approach to compute and tabulate the change in particle size and refractive index as a function of relative humidity. These tables provided a convenient set of optical properties which have been used extensively for a variety of purposes [6, 11, 13, 22, 23].

However, the changes in the optical properties depend on how the particles grow and mix when they are exposed to humidity. Therefore, a more realistic approach would be to treat each aerosol component separately, and compute its change in size and refractive index with relative humidity. The optical properties of a multi-component mixture would be obtained by first computing the optical properties of each component, and then obtain the optical properties of the mixture as the concentration-weighted-average of the optical properties of each aerosol component [24]. For convenience we refer to this procedure as the multi-component (MC) approach below. d'Almeida *et al.* also discussed the MC approach: each component is characterized by a specific log-normal distribution and a wavelength-dependent refractive index, and then these two quantities enable the computation of the optical properties of the components, and finally the addition of the component properties, weighted by their respective mixing ratios, yields the optical properties of the aerosol type in question [25]. Since the optical properties of candidate aerosol models contribute significantly to the accuracy of the atmospheric correction of ocean color imagery, accurate computation of the optical properties of the candidate aerosol models adopted for atmospheric correction purposes be-

comes a matter of considerable importance. In view of the sparcity of observational data the SC approach has been used by the atmospheric community for a variety of purposes. Thus, it is important to assess the accuracy of the SC approach compared to the MC approach and the resulting effect on the atmospheric correction of ocean color imagery.

1.3.2 The validity of the bio-optical model for computing the NIR water-leaving radiance

As mentioned above, the inappropriate application of the black pixel assumption is partly responsible for the excessively high chlorophyll estimates inferred from SeaWiFS data, and for some of the observed underestimates of the water-leaving radiance at blue wavelengths [14]. Thus, Siegel et al. made an attempt to remedy this inappropriate application of the black pixel assumption for SeaWiFS imagery [16], on the basis of a bio-optical model for the water-leaving reflectance derived from semi-emprical model of NIR remote sensing reflectance [17, 18, 19].

However, uncertainties in the above bio-optical model lead to errors in the atmospheric correction used for ocean color retrieval. There are two sources of uncertainty in the model. One is related to the specification of the input parameters to the model, the optical or physical properties. In the current model the NIR water-leaving reflectance is modeled as a function of the spectral absorption and backscattering coefficients of the upper ocean. It is well known that there are some uncertainty in the input optical parameters especially in the backscattering coefficient due to insufficient measurements and to the variation of the optical properties of oceanic particulates in time and space [26, 27, 28, 29, 30, 31, 32, 33]. Detailed observations and analyses are required to reduce this uncertainty in input optical parameters. The other uncertainty is theoretical in nature, and is

related to the methodology used to develop the model. The current model for the NIR water-leaving reflectance is based upon the bio-optical model for the remote sensing reflectance developed by Gordon et al. [17, 18, 34]. The model for the remote sensing reflectance is derived using the two-stream approximation (by disregarding the azimuthal dependency a two-stream approximation to the radiative transfer equation can be developed) [34]. In applications to the computation of the TOA water-leaving radiances in the NIR, the bi-directional reflectance properties of oceanic waters is ignored, i.e., the isotropic (Lambertian) assumption is used to determine the values of the water-leaving reflectance [16].

Zaneveld derived an exact expression for the remote sensing reflectance just beneath the surface of the ocean from the equation of radiative transfer [35, 36]. The results show that the remote sensing reflectance depends on the inherent optical properties and two shape factors that depend on the radiance distribution and the volume scattering function. Morel studied the bi-directional reflectance of oceanic waters in the range between 450 and 600 nm and confirmed the importance of the bi-directional character of the ocean reflectance by a comparison of modeled and measured upward radiance fields [14]. Chen *et al.* investigated the optical characteristics of the NIR (as well as visible) water-leaving radiances and arrived at similar conclusions [15]. These results imply that theoretically the isotropic assumption used in the methodology for the current bio-optical model for remote sensing reflectance as well as water-leaving radiance is questionable. It is important to evaluate the effect of the isotropic assumption on the ocean color retrieval, i.e., to study the performance of the bio-optical model used in computing the TOA water-leaving radiances in the NIR for the SeaWiFS operational algorithm for atmospheric correction.

1.3.3 Violation of black assumption in the NIR bands due to oceanic air bubbles

In addition to the violation of the black assumption due to high chlorophyll concentrations, oceanic air bubbles can efficiently scatter light and thus contribute to the upwelling radiance emanating from the ocean, because they may exist in oceanic waters with a number density in the range of $10^4 - 10^7$ m^{-3} [37, 38, 39, 40, 41]. The impact of oceanic air bubbles on the ocean color has been recognized. Mobley et al. and Bukata discussed qualitatively the optical properties of bubble clouds [21, 42]. Stramski concentrated on light scattering by submerged bubbles in quiescent seas and presented results of scattering and backscattering coefficients at 550 nm in comparison with scattering and backscattering coefficients of bubble-free sea water as estimated from the chlorophyll-based bio-optical models for Case 1 waters [43]. Zhang and co-workers found that air bubbles in the ocean are strong scatterers that contribute significantly to the upwelling radiance, and showed that through enhanced backscattering over the whole visible domain the oceanic air bubbles will influence the remote sensing of ocean color by affecting atmospheric correction as well as optical and biological properties derived from color ratios [44, 45]. They concluded that for high bubble concentrations the assumption that there is negligible water-leaving radiance in the NIR would be invalid. Flatau et al. derived apparent optical properties of oceanic air bubbles (i.e. the remote sensing reflectance) for the whole solar spectrum and showed that the optical effects of submerged microbubbles on the remote sensing reflectance of the ocean are significant [46]. Thus, we need a quantitative assessment of the impact of oceanic air bubbles on atmospheric correction of ocean color imagery.

1.4 Extension of the DISORT code for the coupled atmosphere-ocean system to yield radiances at arbitrary polar angles

Remote sensing of ocean color requires an acurate description of the radiative transfer process throughout the atmosphere-ocean system. A good radiative transfer model for this coupled atmosphere-ocean system is required to interpret the data and to provide a physically sound link between the surface-based measurements of oceanic and atmospheric parameters and the radiances observed by the satellite-deployed ocean color sensors. One of the most commonly used methods for solving radiative transfer problems involving anisotropic scattering is the discrete ordinate method. Since its introduction by Chandrasekhar in the 1940's [47], it has been utilized by many investigators to study the transfer of radiation in planetary atmospheres [48] $\sim$ [60]. The discrete ordinate radiative transfer (DISORT) method has been implemented numerically into a code written in FORTRAN that solves the radiative transfer equation in a medium with a uniform index of refraction [61, 62]. To satisfy the need for applications of radiative transfer theory in oceanography and climate-changes studies that involve two subsystems with different indices of refraction, such as the atmosphere-ocean system, Jin and Stamnes extended the discrete-ordinate method to solve the radiative-transfer equation pertinent for a system consisting of two strata with different indices of refraction [63, 64]. This method can be used to provide consistent solutions for the radiances at the quadrature points (i.e. the discrete ordinates) throughout the coupled atmosphere-ocean system. Also, it may be applied to other systems that need to consider the change in the index of refraction between two strata such as the atmosphere-sea ice ocean system by Jin et al. [63]

However, the existing methodology does not solve for the radiances at arbitrary polar angles, and a very high number of discrete ordinates ('streams' or quadrature points) may be required to get the radiance at small polar angles. Unfortunately, the CPU time required to compute multiply-scattered radiances with the discrete ordinate method is proportional to the third power of the number of streams. It is difficult to compute accurate radiances at very small or zero (zenith upward direction) polar angles with a reasonable computational expense. Thus, it is desirable to extend the DISORT methodology for the coupled atmosphere-ocean system to compute radiances in arbitrary directions. This would make the method more suitable for applications to remote sensing of ocean color and other situations in which a change in the index of refraction between two strata occurs. The iteration of the source-function technique is considered to be better than other interpolation methods to obtain the radiation fields at arbitrary polar angles (other than just the quadrature angles), and it has been successfully applied to multi-layered media with a uniform index of refraction [55, 64, 65]. One important task in this study, is to develop the methodology required to compute the angular distribution of the radiance in the coupled atmosphere-ocean system by using the iteration of the source-function technique.

1.5 Objective of this study

From the above description one sees the that atmospheric correction of ocean color imagery is a non-trivial task, and both aerosols and the black pixel assumption in the NIR play a critical role in this context. Although one of the main goals in remote sensing of the ocean color imagery is to develop a reliable algorithm for the atmospheric correction, the overall objective for this thesis is to focus on quantifying the uncertainties in algorithms for atmospheric correction of

ocean color imagery. These uncertainties are due to: 1) the performance of the bio-optical model for the NIR remote sensing reflectance used in computing the top-of-atmosphere water-leaving radiance at the NIR wavelengths; 2) the black pixel assumption at the NIR wavelengths; 3) the optical properties of candidate aerosol models computed by the SC approach. These uncertainties are numerically assessed by employing the DISORT radiance transfer model for the coupled atmosphere-ocean system developed by Jin and Stamnes [63, 64] and extended as part of this thesis to provide radiances at arbitrary polar angles. According to this overall objective, the thesis consists of five parts as follows:

1. Extension of the radiance expressions to apply at arbitrary polar angles in the DISORT code for the coupled atmosphere-ocean system

2. Comparison of irradiances between the DISORT code for the coupled atmosphere-ocean system and a Monte Carlo model

3. Evaluation of the performance of the bio-optical model for the NIR remote sensing reflectance: implication for ocean color retrieval

4. The role of oceanic air bubbles in atmospheric correction of ocean color imagery

5. Pitfalls in atmospheric correction of ocean color imagery: How should aerosol optical properties be computed?

Based upon this approach, the thesis contains seven chapters including the Introduction.

In Chapter 2 of this thesis ("Extension of the radiance expressions to apply at arbitrary polar angles in the DISORT code for the coupled atmosphere-ocean system") the iteration of the source-function technique is used to derive analytic

expressions for the radiance at arbitrary polar angles and at arbitrary levels the coupled atmosphere-ocean system. The performance of the methodology is tested by applying it to three cases for which molecules and aerosols are included in the atmosphere and oceanic chlorophyll pigments in the ocean.

In Chapter 3 ("Comparison of irradiances between the DISORT code for the coupled atmosphere-ocean system and a Monte Carlo model") four test cases are used for comparison purposes. These four test cases include 1) Test Case 1: aerosol and molecular atmosphere over pure water; 2) Test Case 2: aerosol and molecular atmosphere over water containing 1.0 $mg \cdot m^{-3}$ of chlorophyll pigments distributed uniformly within the first three layers beneath the atmosphere-ocean interface; 3) Test Case 3: a pure molecular scattering atmosphere over pure water; 4) Test Case 4: a pure molecular scattering atmosphere over water containing 1.0 $mg \cdot m^{-3}$ of chlorophyll pigments distributed uniformly within the first three layers beneath the atmosphere-ocean interface.

Chapter 4 ("Evaluation of abio-optical model for the remote sensing reflectance at near-infrared wavelengths: implication for ocean color retrieval") is focused on the performance of the bio-optical model. For this purpose the NIR radiance at nadir and the bi-directional characteristics of the remote sensing reflectance are evaluated. Based upon these analyses, the TOA reflectance deviation in the NIR caused by the isotropic assumption is simulated by computating the NIR remote sensing reflectance and the water-leaving radiance. From this deviation, one may assess the effect of the isotropic assumption, which is used in operational algorithms, on the accuracy of the atmospheric correction of ocean color imagery.

Chapter 5 ("The role of oceanic air bubbles in atmospheric correction of ocean color imagery") expands upon previous studies of oceanic air bubbles by assessing the effect of bubbles on the water-leaving radiance as well on atmospheric correction of ocean color imagery. Specific questions addressed include: How do oceanic

air bubbles affect the black pixel assumption in the NIR region? and What is the contribution of oceanic air bubbles to the TOA water-leaving reflectance at the visible wavelengths, where it may be mistakenly attributed to chlorophyll unless it is properly identified and removed?

In Chapter 6 ("Pitfalls in atmospheric correction of ocean color imagery: How should aerosol optical properties be computed?") two commonly used approaches to compute the optical properties of a multi-component aerosol mixture are discussed, i. e., the single-component (SC) and the multi-component (MC) approaches. Based upon the discussion of the physical difference between the two approaches, computations based on Mie theory and radiative transfer are used to show that the two approaches result in top-of-the-atmosphere radiances that differ more than the water-leaving radiance.

The last chapter, Chapter 7 ("Discussion and conclusions"), contains a summary of the whole thesis.

Chapter 2

Extension of the radiance expressions to apply at arbitrary polar angles in the DISORT code for the coupled atmosphere-ocean system

2.1 Introduction

One of the most commonly used methods for solving the radiative transfer equation involving anisotropic scattering is the discrete ordinate method. Since its introduction by Chandrasekhar in the 1940's [47], it has been utilized by many investigators to study the transfer of radiation in planetary atmospheres [48] ~ [60]. As a results of these efforts, the discrete ordinate radiative transfer (DISORT) method has been implemented numerically into a code written in FORTRAN and satisfactorily used to solve the radiative-transfer problem in vertically inhomoge-

neous media with a uniform index of refraction [61, 62]. Furthermore, to satisfy the need for applications of the DISORT code in oceanography and climate-changes studies involving two or more subsystems with different indices of refraction, such as the radiative transfer within the atmosphere-ocean system, Jin and Stamnes developed a comprehensive methodology based on the discrete-ordinate method, for solving the radiative-transfer equation pertinent for a system consisting of two strata with different indices of refraction [63, 64]. This method provides radiances at the discrete ordinates, i.e. the quadrature points and at arbitrary levels in the coupled atmosphere-ocean system. The code may be applied to other systems that need to consider the change in the index of refraction between two strata. However, Jin and Stamnes did not provide solutions of the radiation field at arbitrary polar angles, and a very high number of quadrate angles or streams is required to get accurate radiances at a small polar angles. Unfortunately, the CPU time for computing multiply-scattered radiances with the discrete ordinate method is proportional to the third power of the number of streams, and it is difficult to achieve accurate radiances at arbitrary polar angles, in general, and at a very small or zero (zenith upward direction) polar angle, in particular, at a reasonable expense. Due to this limitation, the existing DISORT methodology should be extended for application to the coupled atmosphere-ocean system. The iteration of the source-function technique is considered to be the best way among available interpolation methods to obtain the radiation fields at arbitrary polar angles rather than just at the quadrature angles. It has been successfully applied to multi-layered media with a uniform index of refraction [55, 64, 65]. Its principle is straight-forward as follows.

In slab geometry the radiance can be expressed as a Fourier cosine series [64]

$$I(\tau, \mu, \Delta\phi) = \sum_{m=0}^{2N-1} I^m(\tau, \mu) \cos m(\Delta\phi) \tag{2.1}$$

where $\Delta\phi = \phi - \phi_0$ is the azimuthal angle ϕ measured relative to that of the incident solar beam, ϕ_0. The Fourier components $I^m(\tau,\mu)$ are independent of each other, and each satisfies the radiative transfer equation in the form

$$\mu\frac{dI^+(\tau,\mu)}{d\tau} = I^+(\tau,\mu) - S^+(\tau,\mu) \tag{2.2}$$

$$-\mu\frac{dI^-(\tau,\mu)}{d\tau} = I^-(\tau,\mu) - S^-(\tau,\mu) \tag{2.3}$$

where we have omitted the 'm' superscript. We have done the usual diffuse-direct splitting, so that $I^+(\tau,\mu)$ and $I^-(\tau,\mu)$ are the upward and downward diffuse radiances (intensities), and $S(\tau,+\mu)$ and $S(\tau,-\mu)$ are the upward and downward source functions (see below).

Using an integrating factor, we readily obtain from Eqs. (2.2) and (2.3)

$$\frac{d}{d\tau}\left[I^+(\tau,\mu)e^{-\frac{\tau}{\mu}}\right] = \left[\frac{dI^+(\tau,\mu)}{d\tau} - \frac{1}{\mu}I^+(\tau,\mu)\right]e^{-\frac{\tau}{\mu}} = -\frac{S^+(\tau,\mu)}{\mu}e^{-\frac{\tau}{\mu}} \tag{2.4}$$

$$\frac{d}{d\tau}\left[I^-(\tau,\mu)e^{\frac{\tau}{\mu}}\right] = \left[\frac{dI^-(\tau,\mu)}{d\tau} + \frac{1}{\mu}I^-(\tau,\mu)\right]e^{\frac{\tau}{\mu}} = \frac{S^-(\tau,\mu)}{\mu}e^{\frac{\tau}{\mu}}. \tag{2.5}$$

For a slab of thickness τ_b with a uniform index of refraction, the solutions of the upward and downward radiances $[I^{\pm}(\tau,\mu)]$ may easily be obtained by integrating Eqs. (2.4) and (2.5). This approach shows that if we know the source function $S^{\pm}(\tau',\mu)$, we can find the radiance at arbitrary polar angles by integrating it. This approach is commonly referred to as the 'iteration of the source-function technique (ISFT)'.

In the coupled atmosphere-ocean system, however, there are different indices of refraction in the two media. Thus, the refraction and reflectance at the interface must be taken into account when evaluating the source function, and when integrating expressions Eqs. (2.4) and (2.5) to obtain the radiances at arbitrary

polar angles. To take into account the region of total reflectance in the ocean, additional angular quadrature points are required, compared with those used in the atmosphere and in the refractive region of the ocean that communicates directly with the atmosphere. These circumstances imply that the integrations required to obtain radiances at arbitrary polar angles in the coupled atmosphere-ocean system are somewhat complicated though they are quite straight-forward in principle. This explains why the radiances at arbitrary polar angles in the coupled atmosphere-ocean system have not yet been derived and implemented even though the solutions at quadrature points have been available for a few years. The purpose of this chapter is to use the ISFT to derive expressions for the radiation fields at arbitrary polar angles in the atmosphere-ocean system.

In the following sections, we first derive the expressions of the upward and downward radiances at arbitrary polar angles in a homogeneous slab (see section 2.2). Then we extend these expressions to apply in a layered atmosphere-ocean system (see section 2.3). Finally we perform some tests to verify the performance of the derived analytic expressions for the radiances at arbitrary polar angles (see section 2.4).

2.2 Radiance expressions at arbitrary polar angles in a homogeneous slab

For convenience, for the coupled atmosphere-ocean system, we introduce the f ollowing notation:

a) τ_0 is the optical depth at the top of atmosphere

b) τ_a is the optical depth just above the surface of ocean

c) ${\tau_a}^+$ is the optical depth just below the surface of oecan where ${\tau_a}^+ = \tau_a + \varepsilon$

with $\varepsilon \to 0$

d) τ_b is the optical depth at the bottom of the ocean

e) $\mu = \mu^a$ in the atmosphere and $\mu = \mu^o$ in the ocean where $\mu^o = \sqrt{1 - \frac{(1-(\mu^a)^2)}{{m_{rel}}^2}}$.

f) $\rho_s(\mu; m_{rel})$ and $\mathcal{T}(\mu; m_{rel})$ are the specular reflectance and transmittance of the *basic* (or *invariant*) radiance $\tilde{I}^{\pm} = \frac{I^{\pm}}{m_r^2}$, where m_r is the real part of the local refractive index, which has the value $m_r = m_{ra} \approx 1.0$ in the air, and $m_r = m_{ro} \approx 1.34$ in the ocean. The relative refractive index is defined as $m_{rel} = m_{ro}/m_{ra}$.

We integrate Eq. (2.4) from τ_b to τ and Eq. (2.5) from τ_0 to τ ($\tau_0 \leq \tau \leq \tau_b$) such that

$$\int_{\tau_b}^{\tau} d(I^+(\tau,\mu)e^{-\frac{\tau}{\mu}}) = \int_{\tau_b}^{\tau} (-\frac{S^+(\tau,\mu)}{\mu} e^{-\frac{\tau}{\mu}}) d\tau \tag{2.6}$$

and

$$\int_{\tau_0}^{\tau} d(I^-(\tau,\mu)e^{\frac{\tau}{\mu}}) = \int_{\tau_0}^{\tau} (\frac{S^-(\tau,\mu)}{\mu} e^{\frac{\tau}{\mu}}) d\tau. \tag{2.7}$$

Here $\mu = \mu^a$ in the atmosphere and $\mu = \mu^o$ in the ocean. Since the integrals in Eqs. (2.6) and (2.7) apply in the entire atmosphere-ocean system ($\tau_0 \leq \tau \leq \tau_b$), a key step is to obtain the expressions for the upward and downward source functions in the atmosphere and in the ocean.

By applying the discrete-ordinate approximation, we may obtain the following expressions for the atmosphere and ocean (see Appendix A for details):

$$\begin{aligned} S^{\pm}{}_{air}(\tau,\mu^a) &= \sum_{j=1}^{N_1} C_{-j}\tilde{g}_{-j}(\pm\mu^a)e^{k_j{}^a\tau} + \sum_{j=1}^{N_1} C_j\tilde{g}_j(\pm\mu^a)e^{-k_j{}^a\tau} + \tilde{Z}_0(\pm\mu^a)e^{-\frac{\tau}{\mu_0}} \\ &\quad + \tilde{Z}_{01}(\pm\mu^a)e^{\frac{\tau}{\mu_0}} \end{aligned} \tag{2.8}$$

$$S^{\pm}{}_{ocn}(\tau,\mu^o) = \sum_{j=1}^{N_2} C_{-j}\tilde{g}_{-j}(\pm\mu^o)e^{k_j{}^o\tau} + \sum_{j=1}^{N_2} C_j\tilde{g}_j(\pm\mu^o)e^{-k_j{}^o\tau} + \tilde{Z}_{02}(\pm\mu^o)e^{-\frac{\tau}{\mu_{0m}}} \tag{2.9}$$

where the variables, e.g., $\tilde{g}_j(\pm\mu^a)$, $\tilde{g}_j(\pm\mu^o)$, $\tilde{Z}_0(\pm\mu^a)$, $\tilde{Z}_{01}(\pm\mu^a)$, $\tilde{Z}_{02}(\pm\mu^o)$, $X_0^{\pm}(\mu)$, $X_{01}^{\pm}(\mu)$ and $X_{02}^{\pm}(\mu)$, etc., are defined in Appendix A.

Here we need to explain carefully how the quadrature is constructed. In the air, we use $N = N_1$ qudrature angles in each hemisphere, and the corresponding qudrature points and weights are denoted by $\mu_i = \mu_i^a$ and $w_i = w_i^a$ $(i = 1, \cdots, N_1)$. Since the refractive index in the ocean, $m_{ro} = 1.34 > m_{ra}$, light incident on the air-ocean interface from above at the qudrature points $\mu_i^a (i = 1, \cdots, N_1)$ that span 2π steradians in the air, will be refracted into a cone less than 2π steradians in the ocean. Light in the ocean that is scattered out of this cone will suffer total reflection when it strikes the interface from below. To represent this light we must add additional quadrature angles. We therefore set $N = N_2 > N_1$ in the ocean where the additional points $(N_2 - N_1)$ cover the total reflection region. Thus, in the ocean we use $N = N_2$ qudrature angles in each hemisphere, and the corresponding qudrature points and weights are denoted by $\mu_i = \mu_i^o$ and $w_i = w_i^o$ $(i = 1, \cdots, N_2)$ [64].

With these expressions for the source functions, we may consider the integrals in Eqs. (2.6) and (2.7) and derive solutions of the upward and downward radiances at any optical depth within the entire atmosphere-ocean system. Since the line-of-sight (LOS) changes direction across the interface, we discuss the solutions according to the position of the optical depth.

2.2.1 Upward Radiances

Considering Eq. (2.6), i.e.,

$$\int_{\tau_b}^{\tau} d(I^+(\tau,\mu)e^{-\frac{\tau}{\mu}}) = \int_{\tau_b}^{\tau} (-\frac{S^+(\tau,\mu)}{\mu} e^{-\frac{\tau}{\mu}}) d\tau \tag{2.10}$$

one notes that the upper limit of this integral, τ, applies to an arbitrary optical depth within the entire atmosphere-ocean system, i.e., τ lies between τ_0 and τ_b. Since the line-of-sight (LOS) changes direction across the interface between the

atmosphere and ocean, this must be taken into account in the integral of the upward radiances when $\tau \leq \tau_a$.

2.2.1.1 Upward radiances in the ocean ($\tau_b \geq \tau \geq \tau_a{}^+$)

Since there is no change in the LOS when $\tau \geq \tau_a{}^+$, the integrand in Eq. (2.10) is a continuous function, and we easily obtain the following solution of the upward radiances by using Eq. (2.9) for the source function:

$$I^+(\tau,\mu^o) = I^+(\tau_b,\mu^o)e^{-\frac{(\tau_b-\tau)}{\mu^o}} + \sum_{j=-N_2}^{N_2} \frac{C_j\tilde{g}_j(+\mu^o)}{(1+k_j{}^o\mu^o)}\left\{e^{-k_j{}^o\tau} - e^{-\left[k_j{}^o\tau_b+\frac{(\tau_b-\tau)}{\mu^o}\right]}\right\} \quad (2.11)$$

where $C_0\tilde{g}_0(\pm\mu^o) = \tilde{Z}_{02}(\pm\mu^o)$

$k_{-j}{}^o = -k_j{}^o (j > 0)$

$k_0{}^o = \frac{1}{\mu_{0m}}$ where $\mu_{0m} = \sqrt{1 - \frac{(1-(\mu_0{}^a)^2)}{m_{rel}{}^2}}$ and μ_0 is the cosine of the solar incident angle.

2.2.1.2 Upward radiances in the atmosphere ($\tau_0 \leq \tau \leq \tau_a$)

When $\tau_0 \leq \tau \leq \tau_a$, the integrand in Eq. (2.10) is not a continuous function due to the change in the LOS across the interface between the atmosphere and ocean. Thus, the integral of Eq. (2.10) from τ_b to τ is completed by considering three sub-integrals as follows: (1) τ_b to $\tau_a{}^+$, (2) $\tau_a{}^+$ to τ_a and (3) τ_a to τ. After some algebra, we find the expression for the radiance at arbitrary polar angles in the atmosphere ($\tau_0 \leq \tau \leq \tau_a$) (see Appendix B.1 for details):

$$I^+(\tau,\mu^a) = I^+(\tau_a,\mu^a)e^{-(\tau_a/\mu^a-\tau/\mu^a)} + e^{\tau/\mu^a}\int_\tau^{\tau_a}\frac{d\tau'}{\mu^a}e^{-\tau'/\mu^a}S^+{}_{air}(\tau',\mu^a) \quad (2.12)$$

where

$$I^+(\tau_a,\mu^a) = I^-(\tau_a,\mu^a)\rho_s(-\mu^a,m_{rel}) + \left[\frac{I^+(\tau_a{}^+,\mu^o)}{m_{rel}{}^2}\right]\mathcal{T}_s(+\mu^o,m_{rel}). \quad (2.13)$$

We need to quantify the second term on the right side of Eq. (2.12) as follows. We define

$$I^{+}_{air}(\tau,\mu^{a}) = e^{\tau/\mu^{a}} \int_{\tau}^{\tau_a} \frac{d\tau'}{\mu^{a}} e^{-\tau'/\mu^{a}} S^{+}{}_{air}(\tau',\mu^{a}). \tag{2.14}$$

Then by substituting Eq. (2.8) into Eq. (2.14), we obtain

$$\begin{aligned} I^{+}_{air}(\tau,\mu^{a}) &= \sum_{j=-N_1}^{N_1} \frac{C_j \tilde{g}_j(+\mu)}{(1+k_j{}^{a}\mu^{a})} \{e^{-k_j{}^{a}\tau} - e^{-\left[k_j{}^{a}\tau_a + \frac{(\tau_a-\tau)}{\mu^{a}}\right]}\} \\ &\quad + \frac{\tilde{Z}_{01}(+\mu^{a})}{(1+k_0{}^{a}\mu^{a})} \left[e^{k_0{}^{a}\tau_a - \frac{(\tau_a-\tau)}{\mu^{a}}} - e^{k_0{}^{a}\tau}\right] \end{aligned} \tag{2.15}$$

where $k_0{}^{o} = \frac{1}{\mu_{0m}}$

$-k_j{}^{o} = k_{-j}{}^{o} (j > 0)$

$C_0 \tilde{g}_0(-\mu^{o}) = \tilde{Z}_0(-\mu^{o})$.

The second term on the right side of the equation is due to reflectance of the attenuated solar beam by the ocean surface.

2.2.2 Downward radiances

Equation (2.7), i.e.,

$$\int_{\tau_0}^{\tau} d(I^{-}(\tau,\mu)e^{\frac{\tau}{\mu}}) = \int_{\tau_0}^{\tau} (\frac{S^{-}(\tau,\mu)}{\mu} e^{\frac{\tau}{\mu}}) d\tau, \tag{2.16}$$

applies within the entire atmosphere-ocean system, i.e., for τ values lying between τ_0 and τ_b. However, the line-of-sight changes direction across the interface between the atmosphere and ocean, and this must be taken into account in the integral for the downward radiance when $\tau \geq \tau_a{}^{+}$.

2.2.2.1 Downward radiances in the atmosphere ($\tau_0 \leq \tau \leq \tau_a$)

Since the integrand in Eq. (2.16) is continuous in this region, we easily obtain by using Eq. (2.8)

$$I^-(\tau,\mu^a) = I^-(\tau_0,\mu^a)e^{-\frac{(\tau-\tau_0)}{\mu^a}} + \sum_{j=-N_1}^{N_1} \frac{C_j\tilde{g}_j(-\mu^a)}{(1-k_j{}^a\mu^a)}\left\{e^{-k_j{}^a\tau} - e^{-\left[k_j{}^a\tau_0+\frac{(\tau-\tau_0)}{\mu^a}\right]}\right\}$$
$$+\frac{\tilde{Z}_{01}(-\mu^a)}{(1+k_0{}^a\mu^a)}\left\{e^{k_0{}^a\tau} - e^{k_0{}^a\tau_0-\frac{(\tau-\tau_0)}{\mu^a}}\right\} \tag{2.17}$$

where $k_0{}^o = \frac{1}{\mu_{0m}}$

$-k_j{}^o = k_{-j}{}^o (j > 0)$

$C_0\tilde{g}_0(-\mu^o) = \tilde{Z}_{01}(-\mu^o)$.

2.2.2.2 Downward radiances in the ocean ($\tau_b \geq \tau \geq \tau_a{}^+$)

The integrand in Eq. (2.16) is discontinuous due to the change in LOS across the interface between the atmosphere and ocean. So, Eq. (2.16) is integrated in the following three region along the LOS direction as follows: (1) τ_0 to τ_a, (2) τ_a to $\tau_a{}^+$ and (3) $\tau_a{}^+$ to τ ($\tau_b \geq \tau \geq \tau_a{}^+$).

We obtain after some algebra (see Appendix B.2 for details):

$$I^-(\tau,\mu) = I^-(\tau_a{}^+,\mu^o)e^{(\tau_a{}^+/\mu^o-\tau/\mu^o)} + e^{-\tau/\mu^o}\int_{\tau_a{}^+}^{\tau}\frac{d\tau'}{\mu^o}e^{\tau'/\mu^o}S^-{}_{ocn}(\tau',\mu^o) \tag{2.18}$$

where in the refraction region,

$$\frac{I^-(\tau_a{}^+,\mu^o)}{m_{rel}{}^2} = \left[\frac{I^+(\tau_a{}^+,\mu^o)}{m_{rel}{}^2}\right]\rho_s(+\mu^o,m_{rel}) + I^-(\tau_a,\mu^a)\Gamma_s(-\mu^a,m_{rel}) \tag{2.19}$$

and in the totally-reflected region

$$I^-(\tau_a{}^+,\mu^o) = I^+(\tau_a{}^+,\mu^o). \tag{2.20}$$

The second term on the right side of Eq. (2.18) is evaluated as follows. We define

$$I^-_{ocn}(\tau,\mu) = e^{-\tau/\mu^o}\int_{\tau_a{}^+}^{\tau}\frac{d\tau'}{\mu^o}e^{\tau'/\mu^o}S^-{}_{ocn}(\tau',\mu^o). \tag{2.21}$$

By substituting Eqs. (2.9) into Eqs. (2.21), we obtain

$$I^{-}_{ocn}(\tau,\mu) = \sum_{j=-N_2}^{N_2} \frac{C_j \check{g}_j(-\mu^o)}{(1-k_j{}^o\mu^o)} \{e^{-k_j{}^o\tau} - e^{-\left[k_j{}^o\tau_a{}^+ + \frac{(\tau-\tau_a{}^+)}{\mu^o}\right]}\} \qquad (2.22)$$

where $k_0{}^o = \frac{1}{\mu_{0m}}$

$-k_j{}^o = k_{-j}{}^o (j > 0)$

$C_0\tilde{g}_0(-\mu^o) = \tilde{Z}_{02}(-\mu^o)$.

The above expressions yield radiances at arbitrary polar angles in the coupled atmosphere-ocean system where each stratum (atmosphere or ocean) is assumed to be a homogeneous slab in which the optical properties specified by the single-scattering albedo and the phase function are assumed to be constant throughout the slab. Below we extend these expressions to apply to an atmosphere-ocean system divided into a number layers so as to approximate the behavior of a vertically inhomogeneous slab.

2.3 Radiance expressions at arbitrary polar angles in a multi-layered medium

For the multi-layered atmosphere-ocean system, we assume that

1) the atmosphere is divided into L_1 layers and the ocean is divided into L_2 layers, and

2) the corresponding optical depth at the interfaces of these layers are

$\tau_0, \tau_1, ..., \tau_{L_1}, \tau_{L_1+1}, .., \tau_{L_p}, .., \tau_{L_1+L2}$ $(0 \leq L_p \leq L_1 + L_2)$.

Then we may evaluate the integral of the source functions in this stratified medium by integrating layer-by-layer as follows $(\tau_{(p-1)} \leq \tau \leq \tau_p,\ 1 \leq p \leq L_1 + L_2)$ [64]:

$$\int_{\tau}^{\tau_{L_1+L_2}} \frac{d\tau'}{\mu} S^+(\tau',\mu) e^{-\frac{(\tau'-\tau)}{\mu}} = \int_{\tau}^{\tau_p} \frac{d\tau'}{\mu} e^{-\frac{(\tau'-\tau)}{\mu}} S^+{}_p(\tau',\mu) + \sum_{n=(p+1)}^{L_1+L_2} \int_{\tau_{n-1}}^{\tau_n} \frac{d\tau'}{\mu} e^{-\frac{(\tau'-\tau)}{\mu}} S^+{}_n(\tau',\mu) \quad (2.23)$$

and

$$\int_{\tau_0}^{\tau} \frac{d\tau'}{\mu} S^-(\tau',\mu) e^{-\frac{(\tau-\tau')}{\mu}} = \int_{\tau_{p-1}}^{\tau} \frac{d\tau'}{\mu} e^{-\frac{(\tau-\tau')}{\mu}} S^-{}_p(\tau',\mu) + \sum_{n=1}^{p-1} \int_{\tau_{n-1}}^{\tau_n} \frac{d\tau'}{\mu} e^{-\frac{(\tau-\tau')}{\mu}} S^-{}_n(\tau',\mu) \quad (2.24)$$

where $\mu = \mu^a$ and $S^{\pm}(\tau,\mu) = S^{\pm}{}_{air}(\tau,\mu^a)$ in the atmosphere and $\mu = \mu^o$ and $S^{\pm}(\tau,\mu) = S^{\pm}{}_{ocn}(\tau,\mu^o)$ in the ocean.

Expressions for the upward and downward source functions in this multi-layered medium can be derived and substituted into Eqs. (2.23) and (2.24) to arrive at expressions for the radiance at arbitrary polar angles. For the clarity, we omit the algebra and only list the results here. The coefficients $C_0, \tilde{g}_0(+\mu^o), k_j{}^o$, etc., in the following expressions have the same meaning as before except that they apply to the multi-layered medium.

2.3.1 Upward radiances

2.3.1.1 Upward radiances in the ocean ($\tau_b \geq \tau \geq \tau_a{}^+$)

$$I^+(\tau,\mu^o) = I^+(\tau_b,\mu^o) e^{-\frac{(\tau_b-\tau)}{\mu^o}} + I^+_{ocn01}(\tau,\mu^o) + I^+_{ocn02}(\tau,\mu^o) \quad (2.25)$$

where

$$I^+_{ocn01}(\tau,\mu^o) = \sum_{j=-N_2}^{N_2} \frac{C_{jp}\tilde{g}_{jp}(+\mu^o)}{(1+k_{jp}{}^o\mu^o)} \{e^{-k_{jp}{}^o\tau} - e^{-\left[k_{jp}{}^o\tau_p + \frac{(\tau_p-\tau)}{\mu^o}\right]}\} \quad (2.26)$$

$$I^+_{ocn02}(\tau,\mu^o) = \sum_{n=(p+1)}^{L_1+L_2}\{\sum_{j=-N_2}^{N_2}\frac{C_{jn}\tilde{g}_{jn}(+\mu^o)}{(1+k_{jn}{}^o\mu^o)}e^{-\left[k_{jn}{}^o\tau_{n-1}+\frac{(\tau_{n-1}-\tau)}{\mu^o}\right]} - e^{-\left[k_{jn}{}^o\tau_n+\frac{(\tau_n-\tau)}{\mu^o}\right]}\}. \tag{2.27}$$

2.3.1.2 Upward radiances in the atmosphere ($\tau_a \geq \tau \geq \tau_0$)

$$I^+(\tau,\mu^a) = I^+(\tau_a,\mu^a)e^{-(\tau_a/\mu^a-\tau/\mu^a)} + I^+_{air01}(\tau,\mu^a) + I^+_{air02}(\tau,\mu^a) + I^+_{air03}(\tau,\mu^a) \tag{2.28}$$

where

$$\begin{aligned} I^+_{air01}(\tau,\mu^a) &= \sum_{j=-N_1}^{N_1}\frac{C_{jp}\tilde{g}_{jp}(+\mu^a)}{(1+k_{jp}{}^a\mu^a)}\{e^{-k_{jp}{}^a\tau} - e^{-k_{jp}{}^a\tau_p-\frac{(\tau_p-\tau)}{\mu^a}}\} \\ &\quad + \frac{\tilde{Z}_{01p}(+\mu^a)}{(1+k_{0p}{}^a\mu^a)}\{e^{k_{0p}{}^a\tau_p-\frac{(\tau_p-\tau)}{\mu^a}} - e^{k_{0p}{}^a\tau}\} \end{aligned} \tag{2.29}$$

$$I^+_{air02}(\tau,\mu^a) = \sum_{n=(L_1+1)}^{L_1+L_2}\sum_{j=-N_1}^{N_1}\frac{C_{jn}\tilde{g}_{jn}(+\mu^a)}{(1+k_{jn}{}^a\mu^a)}\{e^{-\left[k_{jn}{}^a\tau_{n-1}+\frac{(\tau_{n-1}-\tau)}{\mu^a}\right]} - e^{-\left[k_{jn}{}^a\tau_n+\frac{(\tau_n-\tau)}{\mu^a}\right]}\} \tag{2.30}$$

$$I^+_{air03}(\tau,\mu^a) = \sum_{n=(L_1+1)}^{L_1+L_2}\frac{\tilde{Z}_{01n}(+\mu^a)}{1-k_{0n}{}^a\mu^a}\{e^{k_{0n}{}^a\tau_{n-1}-\frac{(\tau_{n-1}-\tau)}{\mu^a}} - e^{k_{0n}{}^a\tau_n-\frac{(\tau_n-\tau)}{\mu^a}}\}. \tag{2.31}$$

2.3.2 Downward Radiances

2.3.2.1 Downward radiances in the atmosphere ($\tau_a \geq \tau \geq \tau_0$)

$$I^-(\tau,\mu^a) = I^-(\tau_0,\mu^a)e^{-\frac{(\tau-\tau_0)}{\mu^a}} + +I^-_{air01}(\tau,\mu^a) + I^-_{air02}(\tau,\mu^a) + I^-_{air03}(\tau,\mu^a) \tag{2.32}$$

where

$$\begin{aligned} I^-_{air01}(\tau,\mu^a) &= \sum_{j=-N_1}^{N_1}\frac{C_{jp}\tilde{g}_{jp}(-\mu^a)}{(1-k_{jp}{}^a\mu^a)}\{e^{-k_{jp}{}^a\tau} - e^{-\left[k_{jp}{}^a\tau_0+\frac{(\tau-\tau_0)}{\mu^a}\right]}\} \\ &\quad + \frac{\tilde{Z}_{01p}(-\mu^a)}{(1+k_{0p}{}^a\mu^a)}\{e^{k_{0p}{}^a\tau} - e^{k_{0p}{}^a\tau_0-\frac{(\tau-\tau_0)}{\mu^a}}\} \end{aligned} \tag{2.33}$$

$$I^-_{air02}(\tau,\mu^a)=\sum_{n=1}^{p-1}\{\sum_{j=-N_1}^{N_1}\frac{C_{jp}\tilde{g}_{jp}(-\mu^a)}{(1-k_{jn}{}^a\mu^a)}\{e^{-\left[k_{jn}{}^a\tau_n+\frac{\tau-\tau_n}{\mu^a}\right]}-e^{-\left[k_{jn}{}^a\tau_{n-1}+\frac{(\tau-\tau_{n-1})}{\mu^a}\right]}\}\} \tag{2.34}$$

$$I^-_{air03}(\tau,\mu^a)=\sum_{n=1}^{p-1}\frac{\tilde{Z}_{01n}(-\mu^a)}{(1+k_{0n}{}^a\mu^a)}\{e^{k_{0n}{}^a\tau_n+\frac{(\tau_n-\tau)}{\mu^a}}-e^{k_{0n}{}^a\tau_{n-1}+\frac{\tau_{n-1}-\tau}{\mu^a}}\}. \tag{2.35}$$

2.3.2.2 Downward radiances in the ocean ($\tau_b \geq \tau \geq \tau_a{}^+$)

$$I^-(\tau,\mu^o)=I^-(\tau_a{}^+,\mu^o)e^{(\tau_a{}^+/\mu^o-\tau/\mu^o)}+I^-_{ocn01}(\tau,\mu^o)+I^-_{ocn02}(\tau,\mu^o) \tag{2.36}$$

where

$$I^-_{ocn01}(\tau,\mu^o)=\sum_{j=-N_2}^{N_2}\frac{C_{jp}\tilde{g}_{jp}(-\mu^o)}{(1-k_{jp}{}^o\mu^o)}\left\{e^{-k_{jp}{}^o\tau}-e^{-\left[k_{jp}{}^o\tau_{p-1}+\frac{(\tau-\tau_{p-1})}{\mu^o}\right]}\right\} \tag{2.37}$$

and

$$I^-_{ocn02}(\tau,\mu^o)=\sum_{n=L_1+2}^{p-1}\sum_{j=-N_2}^{N_2}\frac{C_{jn}\tilde{g}_{jn}(-\mu^o)}{(1-k_{jn}{}^o\mu^o)}\left[e^{-\left[k_{jn}{}^o\tau_n+\frac{(\tau-\tau_n)}{\mu^o}\right]}-e^{-\left[k_{jn}{}^o\tau_{n-1}+\frac{(\tau-\tau_{n-1})}{\mu^o}\right]}\right] \tag{2.38}$$

2.4 Performance tests of the modeling

The above expressions for the upward and downward radiances at arbitrary polar angles have been implemented successfully in the DISORT code for the ocean-atmosphere system [63]. We designed three cases to test the performance of the radiance expressions following in part the approach outlined in reference [65]. In the following computations, unless otherwise stated, the Maritime aerosol model at relative humidity of 90 % (Maritime-90) [9] with a homogeneous distribution of aerosol particles from the surface of the ocean to the height of 4 km above the surface is included in the atmosphere. In the ocean we adopt a chlorophyll

concentration of 1.0 $mg \cdot m^{-3}$ (homogeneously distributed from the surface of the ocean to a depth of 10 m. The solar zenith angle is 45° and the relative azimuthal angle is 0°.

An important feature of these expressions is that when evaluated at the quadrature points they yield results identical to the expressions obtained using the quadrature scheme. This will be demonstrated by the first test which gives a comparison of the angular distribution of the radiance computed with these two schemes (a theoretical proof is provided in Appendix C). Figure 2.1 shows this comparison at four levels in the atmosphere-ocean system: a) at the top-of-atmosphere, b) just above the surface of the ocean and c) just below the surface of the ocean, and d) at a level in the ocean. The good agreement implies not only that the methodology may provide accurate results at the arbitrary polar angles, but also that it can be used for realistic case studies (e.g. the ocean color).

The second test is designed to test how the new methodology can be used to obtain a higher accuracy compared to a cubic spline method used to interpolate or extrapolate the angular distribution of the intensity based upon the intensities computed at the discrete quadrature angles. First, the DISORT code for the coupled atmosphere-ocean system is used to compute the intensities at the same four layers as in Fig. 2.1 from the quadrature scheme with $N = 48$ streams. The intensity values computed at these angles are considered as "benchmark" values. Then the intensities at these angles at these four layers are computed with the ISFT and with a spline interpolation with the number of stream sets between 4 and 48 respectively. In the spline interpolation, the radiance field has been interpolated separately in each hemisphere to avoid the problems associated with spline interpolation at discontinuities. The intensity values obtained either by the ISFT or by the spline interpolation are compared to the "benchmark" values at all four layers. The average absolute error for each stream number is computed for each scheme.

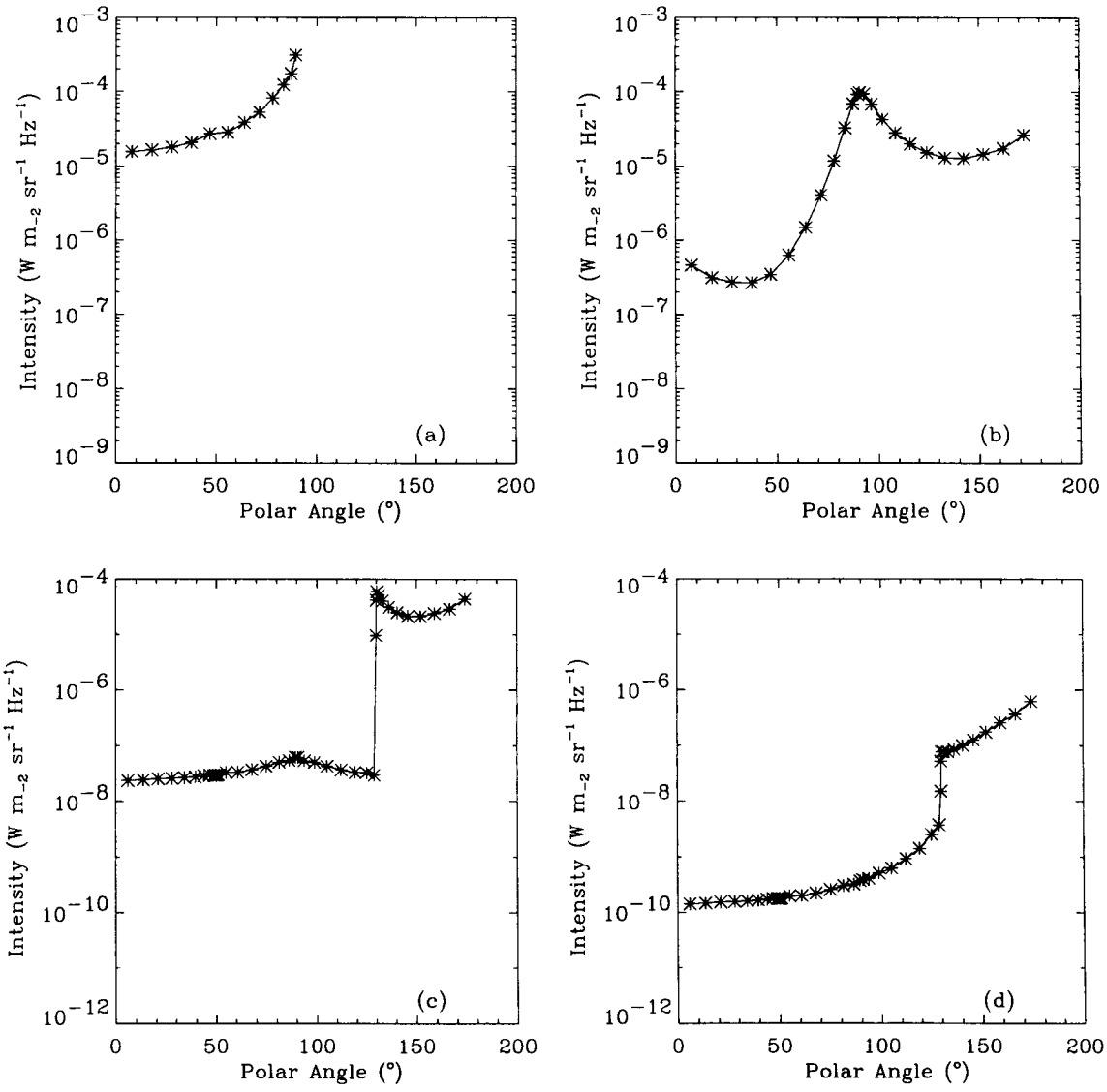

Figure 2.1 Comparison of the radiances at 865 nm as a function of the polar angle computed using the iteration of the source function technique with results from using the quadrature scheme. The solid line is obtained from the analytic expression using iteration source function technique and the asterisks denote the values of the intensities at the quadrature angles using the quadrature scheme. (a) At the top-of-atmosphere. (b) Just above the surface of the ocean. (c) Just below the surface of the ocean. (d) In the ocean.

Figure 2.2 shows such an absolute error in the computation of the intensity as a function of the number of streams N when the chlorophyll concentration is pretty high (10.0 mg m^{-3}) in the ocean. The results in Fig. 2.2 demonstrate that the ISFT method computes the radiance with much higher accuracy than the spline interpolation scheme. They also show that when the number of streams is larger than 16, the intensity error incurred by the ISFT is small and relatively stable.

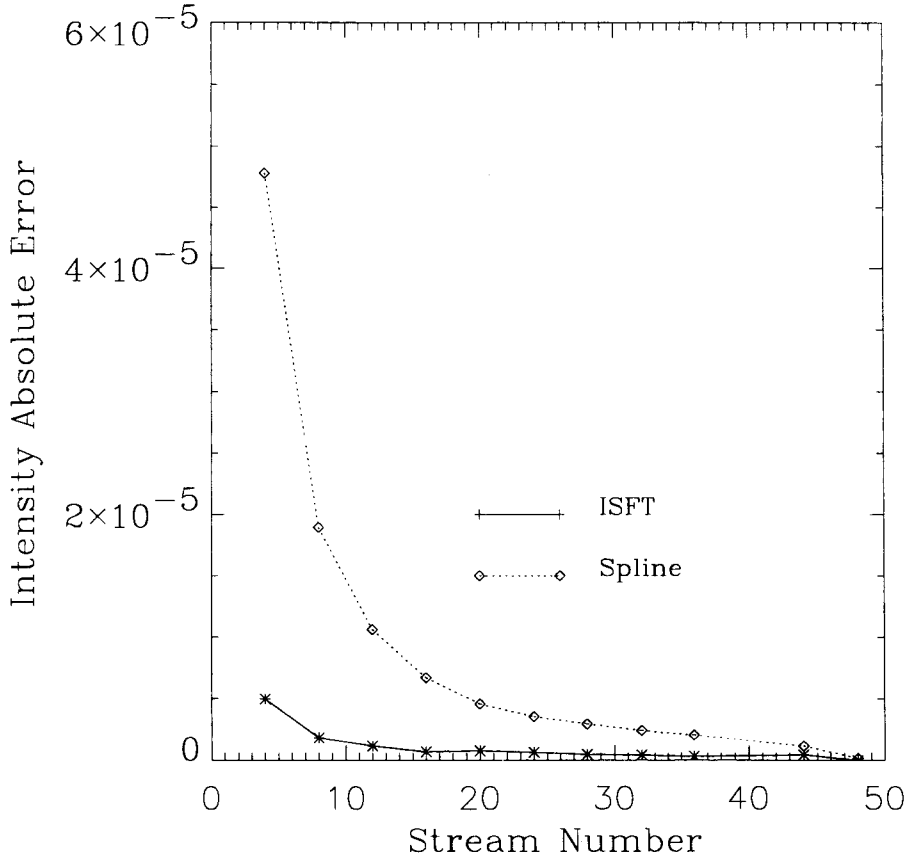

Figure 2.2 Intensity absolute error at 443 nm as a function of the number of the streams employed in the DISORT code for the coupled atmosphere-ocean system for a chlorophyll concentration of 10.0 mg m^{-3}.

The third test is designed to explore the advantage of the ISFT scheme to

compute intensities at arbitrary polar angles. Similar to the second test, first, the DISORT code for the coupled-atmosphere system is used to compute the intensities using the quadrature scheme with N = 48 streams. These angles are assumed to be user's angles, and the intensity values computed at these angles are considered as "benchmark" values of the intensities. Then the intensities at these angles are computed with the ISFT and spline interpolation scheme with the number of streams equal to 20. Then the relative error of the intensity ((I'-I)*100.0/I %) at each angle is assessed for each scheme. Here I is the "benchmark" intensity and I' is that obtained from the 20-stream case with the ISFT or spline interpolation. Figure 2.3 clearly shows the superiority of the ISFT methodology. The maximum intensity error of the spline interpolation is 8.5 % while the error of the ISFT seldom exceeds 1.5 %.

2.5 Conclusions

Analytic expressions for the upward and downward intensities at arbitrary polar angles and at arbitrary levels in the atmosphere-ocean system are derived and numerically implemented into the existing DISORT code for the coupled atmosphere-ocean system. To verify the performance of these expressions, we demonstrated that when evaluated at the quadrature points the analytic (ISFT) expressions yield results identical to the expressions obtained using the quadrature scheme. Furthermore, we assess the performance and advantage of the ISFT for interpolating the radiance field at arbitrary polar angles by comparing it to a spline interpolation. The results show that the analytical expressions for the intensity at arbitrary polar angles in the coupled atmosphere-ocean system generally yield more accurate results than a spline interpolation. This extension will allow for fast yet accurate computation of the radiance in the atmosphere-ocean system, and it will be

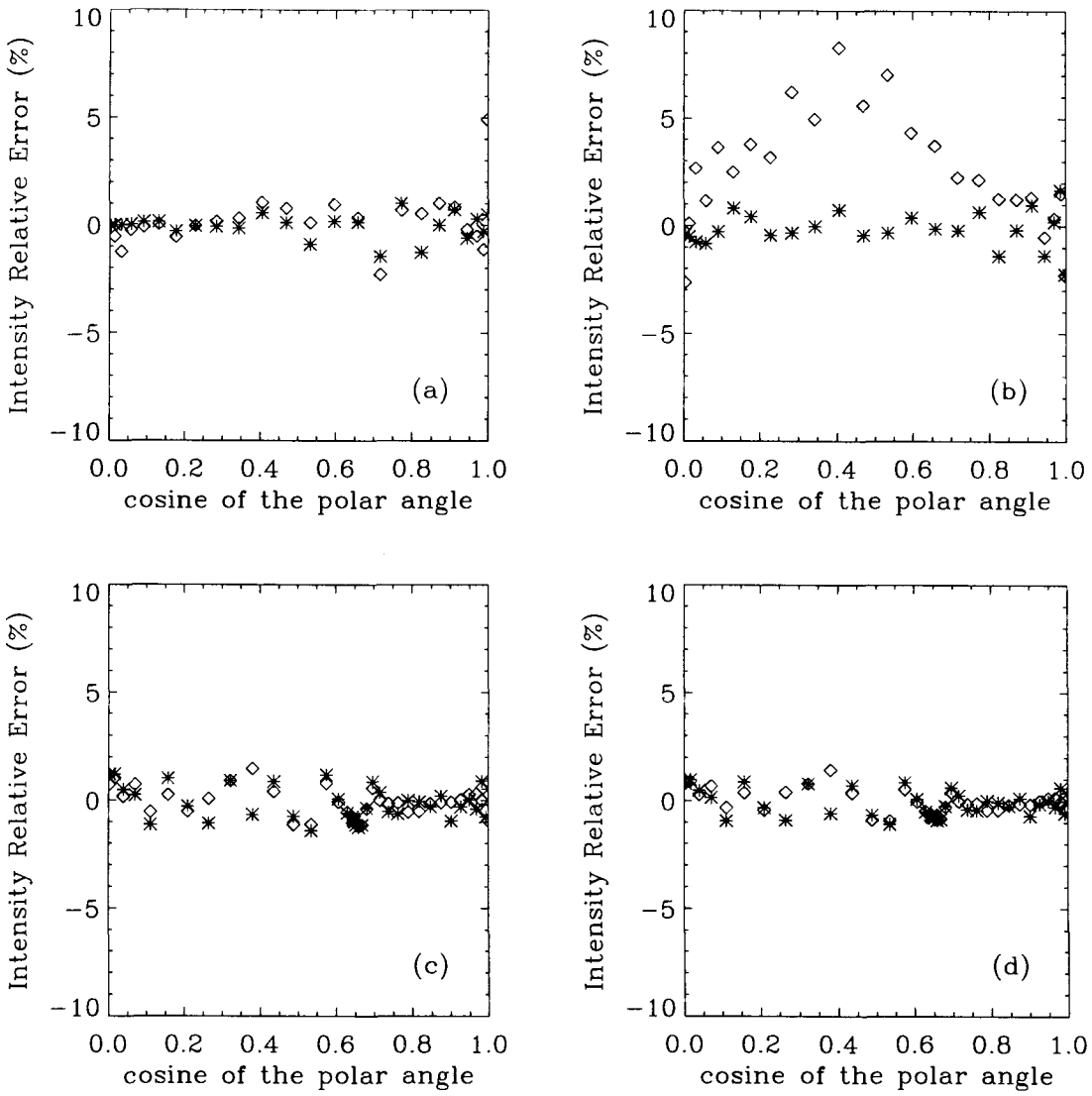

Figure 2.3 Relative error of the intensity as a function of the cosine of the polar angle in the coupled atmosphere-ocean system for a chlorophyll concentration of 10.0 mg m^{-3}. In the figures, the asterisks denote the results obtained using the ISFT and the diamonds results obtained with the spline interpolation. (a) At the top of atmosphere. (b) Just above the surface of the ocean. (c) Just below the surface of the ocean. (d) In the ocean.

useful for applications in oceanography and climate-changes studies invoking two subsystems with different indices of refraction.

Chapter 3

Comparison of irradiances between the DISORT code for the coupled atmosphere-ocean system and a Monte Carlo model

3.1 Introduction

In spite of the increasingly important role that the DISORT code for the coupled atmosphere-ocean system [63, 64] is playing in optical oceanography [10, 15], the code has not been extensively compared with measured values of the quantities it predicts. This desirable model-data comparison is not presently possible because comprehensive oceanic optical data sets are not available. Such data sets must contain simultaneous measurements of the inherent optical properties of the sea water (e.g., the absorption and scattering coefficients and the scattering phase function), environmental parameters (e.g., the sky radiance distribution and sea state), both of which are required inputs to the model, and radiometric quantities (e.g., the

complete radiance distribution or various irradiances) to be compared against output of the model. In this situation, model-model comparisons provide valuable means of identifying errors in the numerical implementation and in the mathematical representation of physical phenomena. In 1993, a comparison of seven numerical models including the DISORT code for the coupled atmosphere-ocean system for computing underwater light fields was carried out by simulating seven canonical problems [20]. It was found that the DISORT code has no statistical fluctuations and has an advantage in the computation of upward quantities and in computations of quantities at great depths. Currently, the DISORT code is being applied in the remote sensing of ocean color. Thus, further comparisons between the DISORT code and a Monte Carlo are desirable to assess its performance in this context. To this end, four test cases related to the coupled atmosphere-ocean system have been designed to compare the methods.

3.2 Description of four test cases

In a realistic atmospheric and oceanic situations, the atmosphere contains molecules and aerosols, and the ocean contains water molecules and oceanic particles (hydrosols). In case-I waters, the dominant oceanic particles are chlorophyll pigments. Thus, the four test cases for comparison are selected as follows:

1) Test case 1: an aerosol and molecular atmosphere over pure water (molecules only).

2) Test case 2: an aerosol and molecular atmosphere over ocean water containing 1.0 $mg \cdot m^{-3}$ chlorophyll pigments distributed uniformly within the top 10 m beneath the atmosphere-ocean interface.

3) Test case 3: a pure molecular scattering atmosphere over pure water.

4) Test case 4: a pure molecular scattering atmosphere over ocean water con-

taining 1.0 mg·m^{-3} of chlorophyll pigments distributed uniformly within the top 10 m meters beneath the atmosphere-ocean interface.

In each of these cases, the atmosphere is divided into 50 1-km-thick layers with a fixed molecular composition defined by Elterman (1968) [66]. For the cases with both aerosols and molecules in the atmosphere: the 5 layers contain Maritime aerosols at a relative humidity (RH) of 90 % (referred to as Maritime-90) [9]; the upper 45 layers contain the Rural aerosols with RH of 70 % (referred to as Rural-70) [9]. The Henyey-Greenstin (HG) phase function is assumed for atmospheric aerosols for the convenience of comparison with the MC, i.e. [64],

$$p_{aero}(cos\Theta) = \frac{1-g^2}{(1+g^2-2gcos\Theta)^{3/2}}, \tag{3.1}$$

where the g is the asymmetry factor and Θ is the scattering angle. The asymmetry factor for the Maritime-90 aerosol model is 0.7871 and 0.6584 for the Rural-70 aerosols at 490 nm.

The volume phase function for atmospheric molecules is determined by

$$p_{mol}(\Theta) = \frac{3}{(3+p)}(1+pcos^2\Theta) \tag{3.2}$$

with p (polarization at right angle) = 1.0.

Thus, the total volume scattering function for an atmosphere containing both molecules and aerosols is

$$p_{atm}(\Theta) = \frac{b_{mol}}{b_{atm}}p_{mol}(\Theta) + \frac{b_{aero}}{b_{atm}}p_{aero}(\Theta) \tag{3.3}$$

where b_{mol} and b_{aero} are the scattering coefficients of atmospheric molecules and aerosols, respectively, and $b_{atm} = b_{mol}+b_{aero}$. The optical properties of atmospheric molecules are adopted from Elterman [1968] [66], and those of atmospheric aerosols from Shettle and Fenn [1979] [9].

The water body is taken to be horizontally homogeneous and the real index of refraction of the water is n=1.31. The depth below the surface can be specified by the geometric depth z in meters and is divided into 13 layers. The scattering phase function for pure water molecules is determined by Eq. (3.2) but with p=0.84 [68]. The phase function for the oceanic chlorophyll pigments is assumed to be the HG phase function with an asymmetry factor of 0.99. Thus, the total volume scattering function for ocean water containing chlorophyll is

$$p_{ocean}(\theta) = \frac{b_w}{b_{ocn}} p_w(\theta) + \frac{b_{chl}}{b_{ocn}} p_{chl}(\theta) \tag{3.4}$$

where the b_w and b_{chl} are the scattering coefficients of pure water and chlorophyll pigments, respectively, and $b_{ocn} = b_w + b_{chl}$. Absorption and scattering coefficients for ocean water are determined by [67]

$$a_{ocn}(\lambda) = a_w(\lambda) + 0.06A(\lambda)[Chl]^{0.65} + a_y(440)exp(-0.014(\lambda - 440)) \tag{3.5}$$

with

$$a_y(440) = 0.2(a_w(440) + 0.06A(440)[Chl]^{0.65}) \tag{3.6}$$

and

$$b_{ocn}(\lambda) = b_w(\lambda) + (550/\lambda)0.3[Chl]^{0.62}). \tag{3.7}$$

For detailed descriptions of these formulae, the reader is referred to Morel and Gentili [1991].

This completes the description of the optical properties (scattering, absorption coefficients and scattering phase function) for the atmosphere-ocean system. Fig. 3.1 shows the vertical distribution of the optical depth and the single scattering albedo (SSALB) (the ratio of the scattering coefficient to the extinction coefficient) for aerosols and molecules in the atmosphere (the vertical distribution in the ocean is not shown because it is relatively simple).

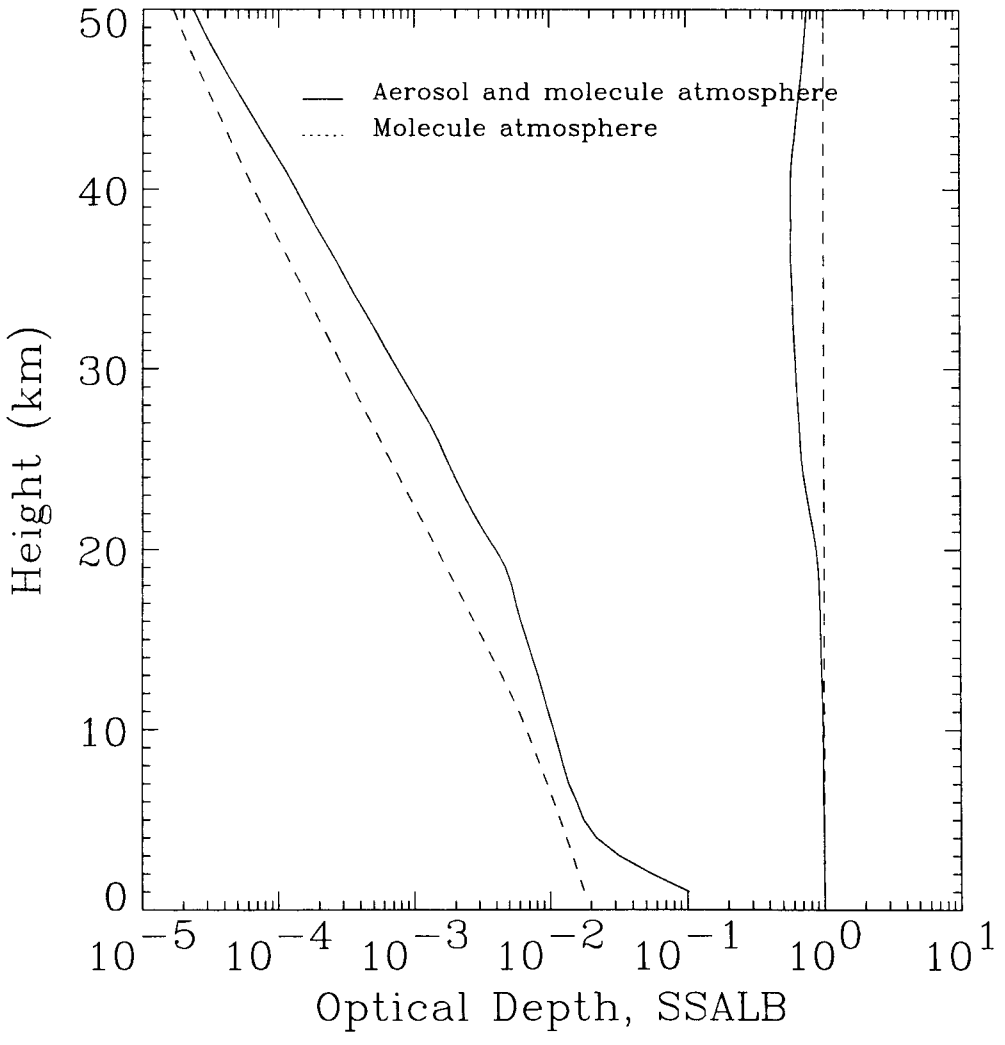

Figure 3.1 Vertical distribution of the scattering and absorption properties at 550 nm in the atmosphere. The left two lines show the optical depth and the right ones for the SSALB.

3.3 Results and discussion

Based upon the above inputs for the optical properties of the whole atmosphere-ocean system, the comparison between the DISORT and MC is carried out by simulating four irradiances as follows:

1) Downward irradiance E_d determined by

$$E_d(\tau) = \int_0^{2\pi} d\phi \int_0^1 d\mu \mu I^-(\tau, \mu, \phi) \tag{3.8}$$

where $I^-(\tau, \mu, \phi)$ is the downward intensity, $\mu = cos\theta$, and ϕ is the azimuthal angle.

2) Upward irradiance E_u determined by

$$E_u(\tau) = \int_0^{2\pi} d\phi \int_0^1 d\mu \mu I^+(\tau, \mu, \phi) \tag{3.9}$$

where $I^+(\tau, \mu, \phi)$ is the upward intensity.

3) Downward scalar irradiance E_{od} determined by

$$E_{od}(\tau) = \int_0^{2\pi} d\phi \int_0^1 d\mu I^-(\tau, \mu, \phi) \tag{3.10}$$

4) Upward scalar irradiance E_{ou} determined by

$$E_{ou}(\tau) = \int_0^{2\pi} d\phi \int_0^1 d\mu I^+(\tau, \mu, \phi) \tag{3.11}$$

Figures 3.2 $\sim$ 3.5 show the comparison of these four variables computed by the two models for the four test cases at 14 output layers, two of which are at the top and bottom of the atmosphere, the rest of which are in the ocean. In general, there is good agreement between the results simulated by two models.

3.4 Conclusions

The DISORT code for the coupled atmosphere-ocean system and a MC code are compared by simulating four irradiances in the atmosphere and ocean. In general,

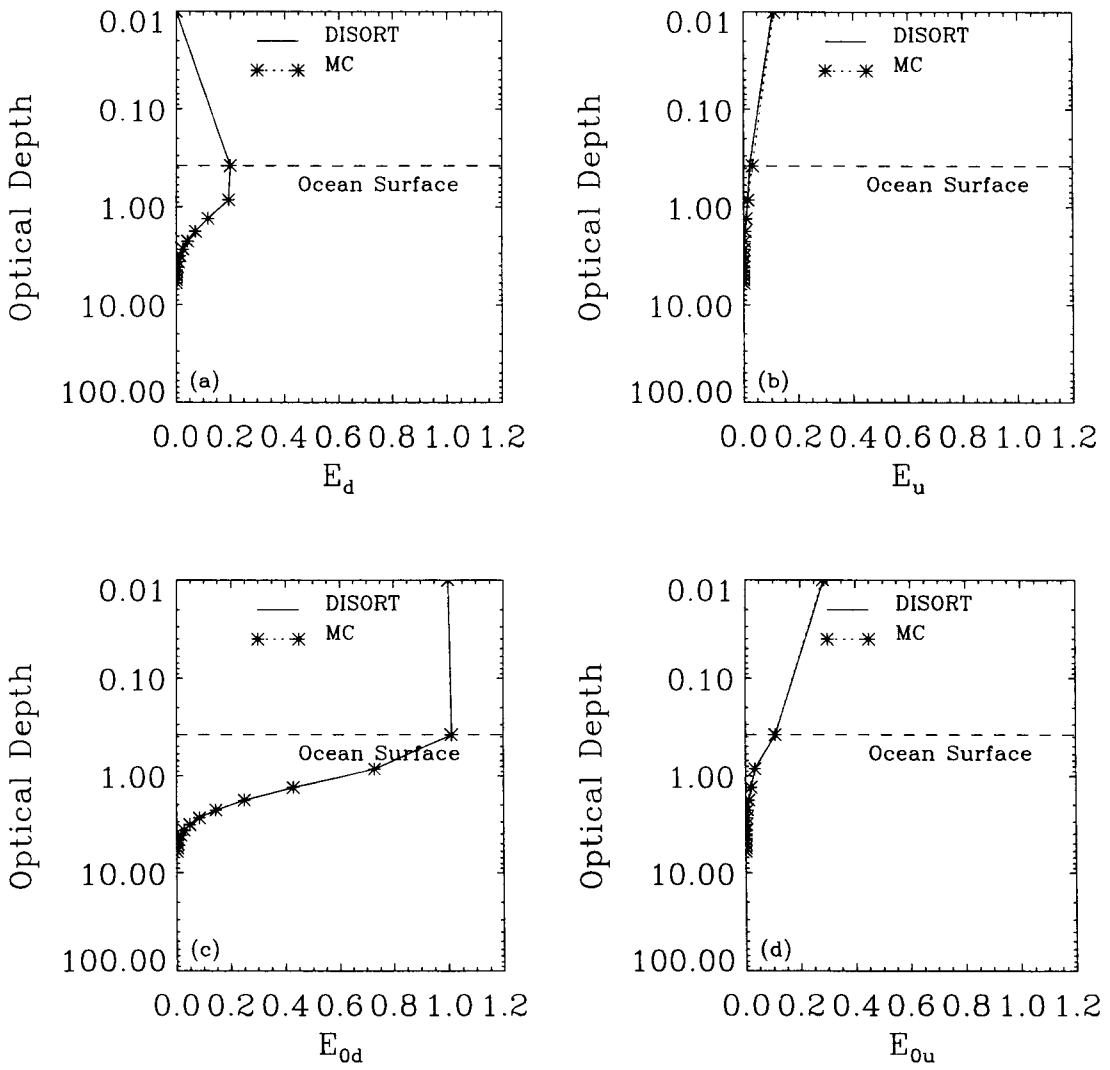

Figure 3.2 Comparison of four irradiances in the coupled atmosphere-ocean system simulated by the DISORT for test case 1. In figures, the optical depth for the top layer is assumed to be '0.01' for the convenience of the logarithm axis whose correct value is zero. (a)E_d (b)E_u (c)E_{od} (d)E_{ou}.

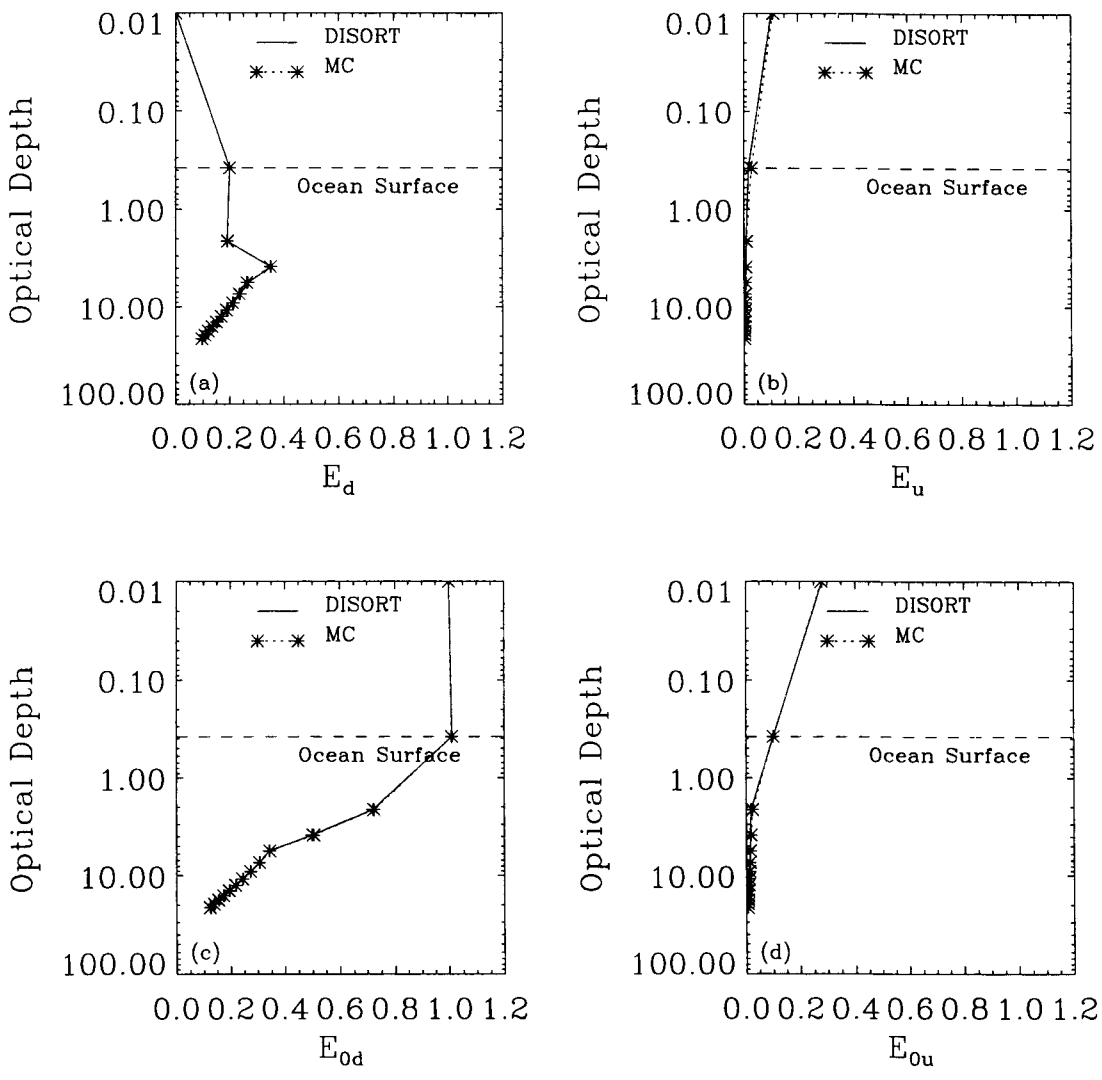

Figure 3.3 Same as Fig. 3.2 but for test case 2.

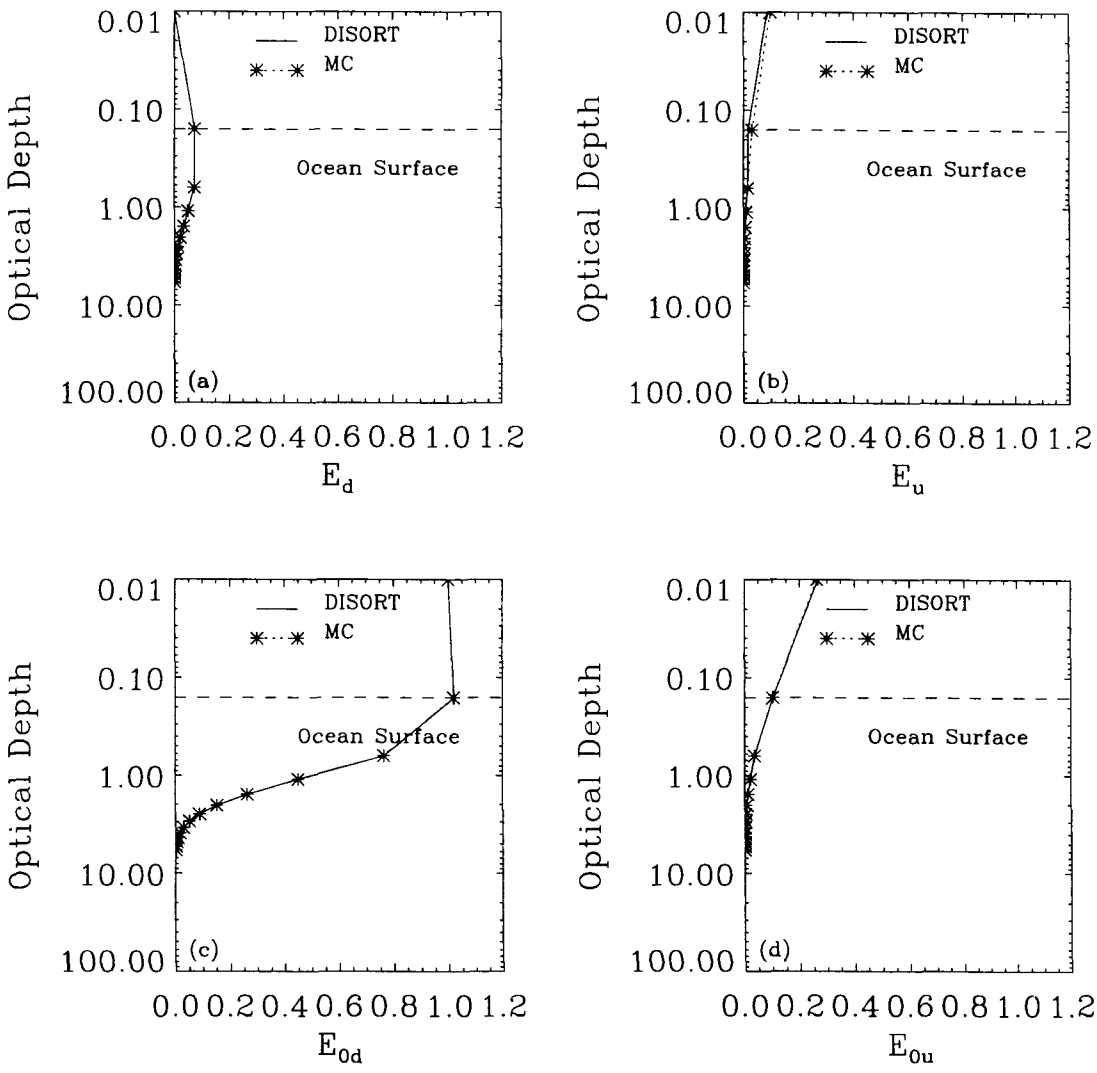

Figure 3.4 Same as Fig. 3.2 but for test case 3.

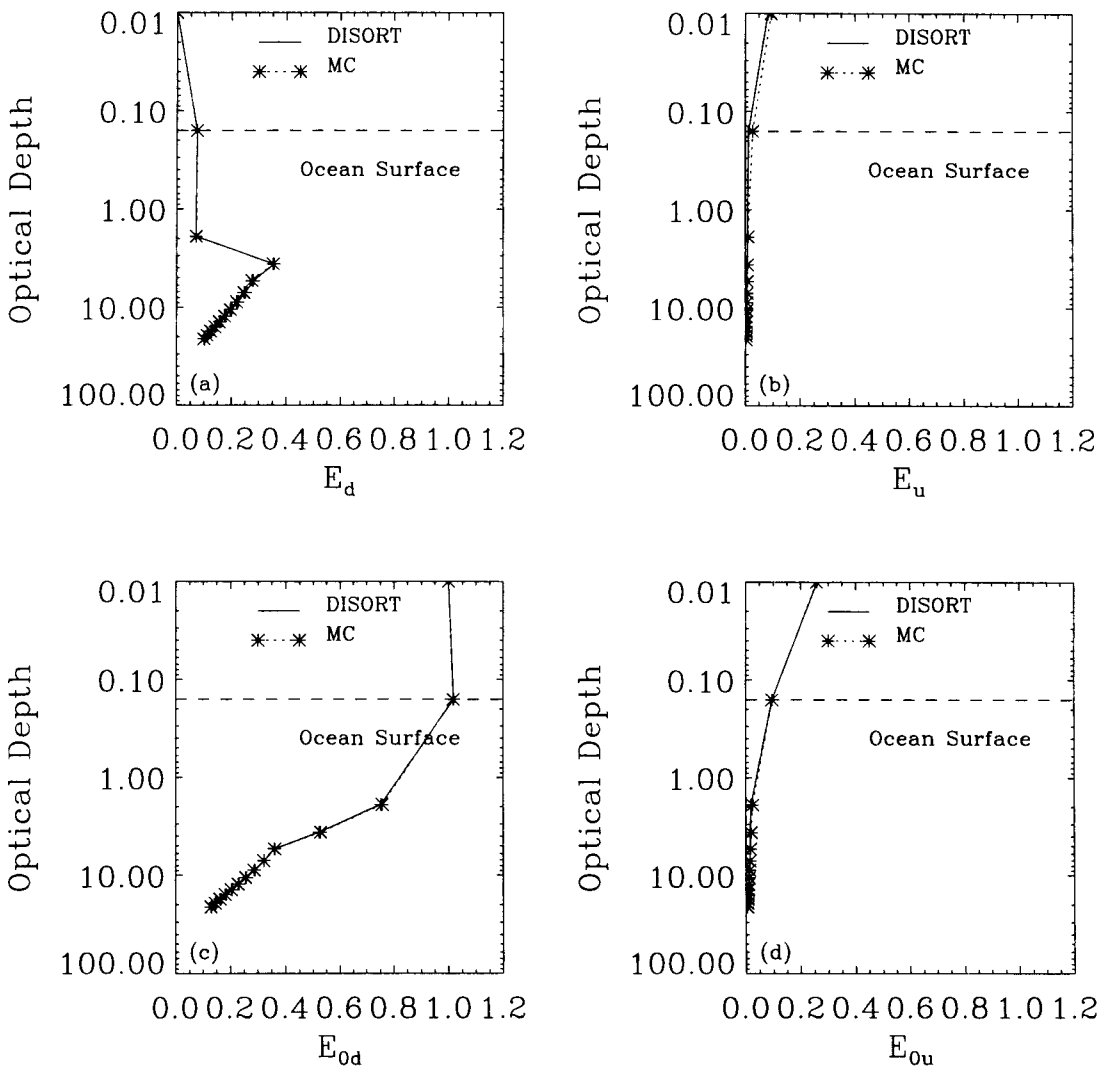

Figure 3.5 Same as Fig. 3.2 but for test case 4.

there is a good agreement between these irradiances. This implies that the two radiative transfer models perform quite well. However, comparison of simulated angular distributions of the in-water light fields remains to be carried out.

Chapter 4

Evaluation of a bio-optical model for the remote sensing reflectance at near-infrared wavelengths: implication for ocean color retrieval

4.1 Introduction

Ocean color is the water-leaving radiance in the visible just above the ocean surface resulting from chlorophyll pigments, as well as dissolved and particulate materials in the subsurface ocean waters. Its retrieval from the satellite-measured top-of-atmosphere (TOA) radiance over the oceans requires the removal of the atmospheric contribution from the measured radiance, a process called atmospheric correction. The Sea-viewing Wide Field-of-view Sensor (SeaWiFS) is providing the oceanographic community an unprecedented opportunity to retrieve ocean color

on a global scale. An operational algorithm for atmospheric correction of ocean color imagery for SeaWiFS has been developed by Gordon and co-workers [69, 70]. This algorithm relies on the black pixel assumption (according to which water-leaving radiances in the near-infrared (NIR) bands (765 and 865 nm) are zero) to retrieve the optical properties of atmospheric aerosols. For clear ocean waters this algorithm is usually accurate to within ~5 % in the blue for non- and weakly absorbing aerosols [70]. However, for highly productive waters (low water-leaving radiances in the visible bands, this algorithm underestimates dramatically the waters leaving reflectance in the violet and blue (SeaWiFS bands 1 and 2) [16, 71]. The inappropriate application of the black pixel assumption is partly responsible for the excessively high chlorophyll estimates inferred from SeaWiFS data and for some of the underestimations of the water-leaving radiance at blue wavelengths [14]. Hence, an attempt has recently been made by Siegel et al. [16] to relax this black pixel assumption for SeaWiFS imagery by using a model for the NIR water-leaving radiance which is based upon the bio-optical model for remote sensing reflectance developed by Gordon and co-workers [17, 18, 19]. It is found that this relaxation of the NIR black pixel assumption results in a significant increase in the water-leaving reflectance in the violet and blue bands when the chlorophyll concentration is greater than 2 mg m^{-3} [16].

However, uncertainties in the above bio-optical model for the remote sensing reflection lead to errors in the atmospheric correction of ocean color imagery. These uncertainties in the model are due to two sources. One is related to the specification of the input parameters to the model, the optical or physical properties. In the current model the NIR water-leaving reflectance is modeled as a function of the spectral absorption and backscattering coefficients of the upper ocean. It is well known that there is some uncertainty in the input optical parameters especially in the backscattering coefficient due to insufficient measurements and to the variation

of the optical properties of the oceanic particulates in time and space [26, 27, 28, 29, 30, 31, 32, 33]. Detailed observations and analyses are required to reduce this uncertainty in input optical parameters.

The other uncertainty is theoretical in nature and is related to the methodology used to develop this model. The current model for the NIR water-leaving reflectance is based upon a bio-optical model for the nadir remote sensing reflectance developed by Gordon et al. [17, 34, 18]. The remote sensing reflectance is derived using the two-stream approximation [34]. In its applications to compute NIR of the water-leaving radiances, the bi-directional properties of oceanic waters are ignored, i.e., the isotropic Lambertian assumption is invoked. Zaneveld derived an exact expression for the monochromatic remote sensing reflectance just beneath the surface of the ocean from the equation of radiative transfer [35, 36]. This expression shows that the remote sensing reflectance depends on the inherent optical properties and two shape factors that depend on the radiance distribution and the volume scattering function. Morel studied the bi-directional reflectance of oceanic waters between 450 and 600 nm and confirmed the importance of the bi-directional character of the ocean reflectance by a comparison of modeled and measured upward radiance fields [14]. Chen *et al.* [15] investigated the optical characteristics of the NIR (as well as visible) water-leaving radiances using the DISORT code for the coupled atmosphere-ocean system [63, 64], and concluded that the magnitude of the NIR (visible) water-leaving radiances depend on (i) the ocean particle concentration (e.g. chlorophyll-a), (ii) the scattering characteristics of particles in the near-surface ocean water, described by their shape, size, and refractive-index distribution, which in turn determine the scattering phase function; (iii) the aerosol optical depth; and (iv) the sun-satellite geometry. These results imply that theoretically the isotropic assumption invoked in current bio-optical models for the remote sensing reflectance used to infer water-leaving radiance is questionable. One

important question arises: Does the isotropic assumption impair the accuracy of the ocean color retrieval? Atmospheric correction of ocean color imagery is a non-trivial task because the water-leaving radiance resulting from oceanic chlorophyll pigments can be as low as a few percent of the TOA radiance [21] and because accurate determination of the aerosol contribution to the TOA radiance in the visible is very difficult [69, 70, 15]. Thus, it is important to quantify the error resulting from invoking this assumption in computation of the water-leaving radiance and in the determination of the TOA water-leaving radiances required for atmospheric correction.

In this study, the performance of a bio-optical model for nadir remote sensing reflectance at 670 nm is first evaluated by comparing its results with the SeaWiFS Bio-optical Algorithm Mini-Workshop (SeaBAM) data base [81] as well as with simulations using the DISORT code for the coupled atmosphere-ocean system with the newly derived solutions at arbitrary polar angles (Chapter 2). In addition to the bio-optical model developed by Gordon et al., as specified by Siegel et al., the model developed by Tanaka et al. is included in the this evaluation. Secondly, the bi-directional characteristic of the NIR remote sensing reflectance is simulated by the DISORT code for the coupled atmosphere-ocean system. Finally, the TOA reflectance deviation caused by the isotropic assumption used in the bio-optical model for computing water-leaving radiance at NIR wavelengths is assessed. In the case of the atmospheric correction scheme SeaWiFS band 6 and 8 (670 and 865 nm) are used in addition to the current band 7 and 8 [72]. Thus, all of the 670, 765 and 865 nm bands are taken into account in our studies.

4.2 Description of the bio-optical models for the remote sensing reflectance in the NIR

The remote sensing reflectance in the ocean at wavelength λ is defined as

$$R_{rs}(z,\theta,\phi,\lambda) = \frac{L_w(z,\theta,\phi,\lambda)}{E_d(z,\lambda)}, \tag{4.1}$$

where $L_w(z,\theta,\phi,\lambda)$ is the upward radiance at polar angle θ, azimuth angle ϕ and depth z, and $E_d(z,\lambda)$ is the downward irradiance.

In the ocean color community, the remote sensing reflectance just above the sea surface (0^+) is defined as follows:

$$R_{rs}(0^+,\theta,\phi,\lambda) = \frac{L_w(0^+,\theta,\phi,\lambda)}{E_(0^+,\lambda)}, \tag{4.2}$$

which is estimated from that just beneath the surface $R_{rs}(0^-,\theta,\phi,\lambda)$ using the following relationship [21, 73, 74]:

$$R_{rs}(0^+,\theta,\phi,\lambda) = t_r(\lambda)R_{rs}(0^-,\theta,\phi,\lambda) \tag{4.3}$$

with

$$t_r(\lambda) = \frac{1-\rho(\lambda,\theta)}{{n_w}^2(\lambda)}t_d. \tag{4.4}$$

Here $\rho(\lambda,\theta)$ is the Fresnel reflectance from water to air [64], n_w is the wavelength-specific index of refraction for water [21, 75], t_d is the transmittance of $E_d(0^-,\lambda)$ across the sea surface [73, 76].

Currently, there are two bio-optical models available for the nadir remote sensing reflectance at NIR wavelengths (see below for details). One is the model for case-I ocean developed by Gordon et al. [17, 18, 19] and used by Siegel et al. referred to here as Siegel's model for convenience; the other one is the model applicable for both case-I and case-II waters developed by Tanaka et al. referred to

as Tanaka's model. Since both models use the radiance in the nadir direction, the nadir remote sensing reflectance just above the sea surface is written simply as $R_{rs}(0^+, \lambda)$, i.e.,

$$R_{rs}(0^+, \lambda) = \frac{L_w(0^+, \lambda)}{E_d(0^+, \lambda)}, \tag{4.5}$$

which is estimated from the $R_{rs}(0^-, \lambda)$ as

$$R_{rs}(0^+, \lambda) = t_r(\lambda) R_{rs}(0^-, \lambda) \tag{4.6}$$

where $t_r(\lambda)$ varies from 0.515 to 0.524 depending on wavelength, absorption, scattering as well as wind and sky conditions [76].

4.2.1 Review of Siegel's model for $R_{rs}(0^-, \lambda)$

Siegel's model for the remote sensing reflectance just below the ocean surface in case-I waters is determined by

$$R_{rs}(0^-, \lambda) = g_1 \frac{b_b}{a + b_b} + g_2 \{\frac{b_b}{(a + b_b)}\}^2 \tag{4.7}$$

where $g_1 = 0.0949$, $g_2 = 0.0794$ and a and b_b are the absorption and backscattering coefficients, respectively [16]. The absorption coefficient a is given by

$$a = a_w + a_{cs}[chl]^{0.8177396} \tag{4.8}$$

where a_w is the absorption coefficient of pure water. $a_w = 0.4346, 2.550, 4.286\ [m^{-1}]$ at $\lambda = 670$, 765 and 865 nm, respectively; $[chl]$ is the chlorophyll concentration $\mathrm{mg \cdot m^{-3}}$, a_{cs} is Chl-a specific absorption; $a_{cs} = 0.01989, 0.000, 0.000\ m^{-1}$ at $\lambda =$ 670, 765 and 865 nm, respectively.

The scattering coefficient b is determined by

$$b = 0.00288(\frac{\lambda}{500})^{-4.32} + 0.416[chl]^{0.766}(\frac{550.}{\lambda}) \tag{4.9}$$

and the backscattering coefficient b_b is determined as follows

$$b_b = \frac{1}{2} b_w + 0.416[chl]^{0.766}(0.002 + 0.02(0.5 - 0.25 log_{10}([chl]))(\frac{550}{\lambda})). \tag{4.10}$$

4.2.2 Review of Tanaka's model for $R_{rs}(0^+, \lambda)$

Tanaka's model pertains to the remote sensing reflectance at just above the ocean surface in case-I and case-II waters. In case-I waters which is our concern, $R_{rs}(0^+, \lambda)$ is modeled as

$$R_{rs}(0^+, \lambda) = \frac{0.533R(0^-, \lambda)}{Q} \tag{4.11}$$

with

$$R(0^-, \lambda) = \frac{(k-a)}{(k+a)} \tag{4.12}$$

where Q=4.5 and k is the attenuation coefficient determined by

$$k = \sqrt{a(a+2b_b)}. \tag{4.13}$$

Here a and b_b are the absorption and backscattering coefficients, respectively.

The absorption coefficient a is given by

$$a = a_w + a_{cs}[chl] + a_{y440}exp(-0.014(\lambda - 440)) \tag{4.14}$$

where a_w is the absorption coefficient of pure water with a_w = 0.4112, 2.7722, 5.1014 $[m^{-1}]$ at λ = 670, 765 and 865 nm, respectively; a_{cs} is the Chl-a specific absorption where a_{cs} = 0.018982, 0.000, 0.000 $[m^{-1}]$ at λ = 670, 765 and 865 nm, respectively; a_{y440} is a_y at 440 nm, i.e., the absorption by yellow substance.

The scattering coefficient b is given by

$$b = 0.00288(\frac{\lambda}{500})^{-4.32} + (0.3[chl]^{0.62} - b_{w550})\frac{550}{\lambda}. \tag{4.15}$$

and the backscattering coefficient b_b is

$$b_b = \frac{1}{2}b_w + (0.3[chl]^{0.62} - b_{w550})(0.002 + 0.02(0.5 - 0.25log_{10}([chl]))(\frac{550}{\lambda})). \tag{4.16}$$

Figure 4.1 provides a comparison of the optical properties (absorption, scattering and backscattering coefficients, single scattering albedo) of case-I waters computed by employing the Siegel and Tanaka bio-optical models, when the chlorophyll

concentration (Chl) is 0.0, 0.01, 0.1, 1.0, 10.0, and 20.0 mg·m^{-3}, respectively, as a demonstration. This shows that there is some difference between the two models in all of the scattering, absorption and backscattering coefficients, which implies a corresponding difference in the remote sensing reflectance. For the convenience of the comparison below, the remote sensing reflectance at 0^+ is discussed in the reminder of this chapter. So, the remote sensing reflectance at 0^- specified by Siegel will be transformed into the one at 0^+ by Eq. (4.6).

Siegel's model is utilized to relax the NIR black pixel assumption to take into account the water-leaving radiance due to scattering by chlorophyll pigments in the operational algorithm for atmospheric correction of SeaWiFS imagery. Due to its use in an operational algorithm, the following analyses are mainly focused on the evaluation of the Siegel model except for the discussion about the performance of the model at nadir.

4.3 Performance of the bio-optical models for remote sensing reflectance in the NIR

Two bio-optical models for the remote sensing reflectance at nadir either just below or just above the sea surface are derived using the two stream approximation. In modeling of the NIR water-leaving radiance the isotropic assumption is often used to estimate the contribution from oceanic chlorophyll pigments and hereby avoid invoking the black pixel assumption. The two models are evaluated in two respects: 1) the performance of the bio-optical models for the remote sensing reflectance at nadir; 2) the bi-directional characteristics of the water-leaving radiance or the remote sensing reflectance just above (similarly just below) the ocean surface.

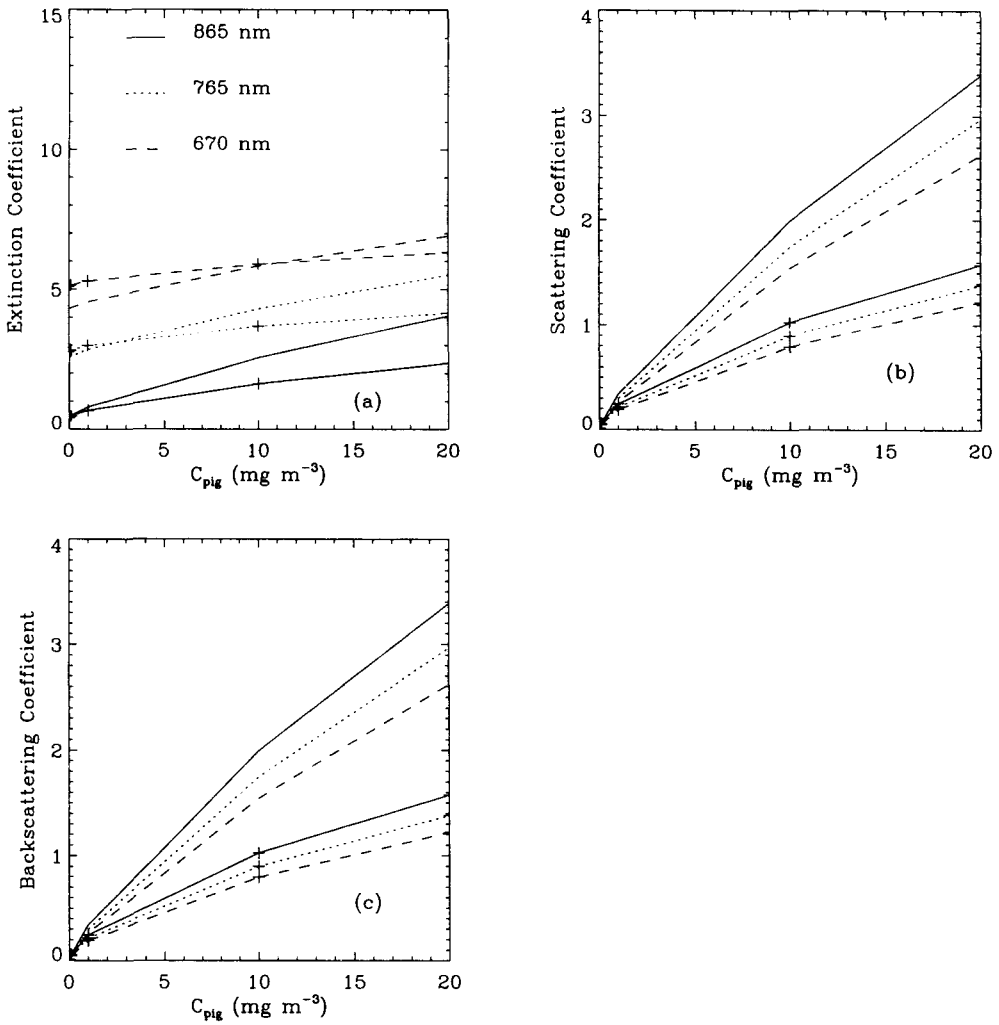

Figure 4.1 Comparison of the optical properties (extinction, scattering and backscattering coefficients) of case-I waters computed by employing the Siegel and Tanaka model in the range between 0.0 and 20.0 mg·m^{-3} of the *Chl*. In figure, the lines without/with marks are for the Siegel and Tanaka models, respectively. (a) Extinction coefficient. (b) Scattering coefficient. (c) Backscattering coefficient.

4.3.1 The performance of the bio-optical models at nadir

The NIR remote sensing reflectances just above (below) the ocean surface at nadir are determined by the optical properties of oceanic waters (scattering and absorption coefficients and the volume phase function) and the solar zenith angle. This implies that it becomes a challenging task to evaluate the performance of the bio-optical models.

4.3.1.1 Comparison with the SeaBAM data at 670 nm

The radiance-chlorophyll data assembled from various sources and included in the SeaBAM data base, consist of data from 919 stations encompassing chlorophyll concentrations between 0.019 and 32.79 mg·m^{-3} and radiances at several wavelengths between 412 and 670 nm [81]. Most of the observations are from Case-I nonpolar waters, whereas a very few (20) observations are from more turbid coastal waters. The remote sensing reflectance just above the sea surface is computed according to Eqs. (4.2) and (4.3). Thus, $R_{rs}(0^+, \lambda)$ at 670 nm is used to assess the performance of the bio-optical models at $\theta = 0°$. Figure 4.2 is a comparison of the $R_{rs}(0^+, \lambda)$ at $\lambda = 670$ nm between the results computed by two bio-optical models and the SeaBAM data. There is a good agreement when the chlorophyll concentration is smaller than 1.0 mg·m^{-3}, but when it is close to or larger than 1.0 mg·m^{-3}, the $R_{rs}(0^+, 670)$ computed by the Siegel model is too large by a few percent for the majority of the measured points, whereas the Tanaka model agrees better with the measured $R_{rs}(0^+, 670)$ for the majority of the measured points.

These two bio-optical models are derived using the two stream approximation. However, since the measured $R_{rs}(0^+, 670)$ values assembled in the SeaBAM data base are scattered within a large range when the chlorophyll concentration is large, it is difficult from this comparison to quantify the error in these bio-optical

models because the variation of the optical properties of the oceanic chlorophyll pigments from region to region is partly responsible for the variation of the measured $R_{rs}(0^+, 670)$, and thus for the difference between the measured and computed $R_{rs}(0^+, 670)$. However, this comparison indicates that it is of practical importance to improve the flexibility of the bio-optical models for the NIR remote sensing reflectance to provide more realistic predictions from region to region.

4.3.1.2 Comparison with the simulations carried out by the DISORT code for the coupled atmosphere-ocean system

Comparisons with the simulated $R_{rs}(0^+, \lambda)$ predicted by the DISORT code for the coupled atmosphere-ocean system are carried out at λ = 670, 765 and 865 nm below. Due to the uncertainty of the phase function for oceanic chlorophyll pigments in these two bio-optical models for the remote sensing reflectance, several assumptions about the phase function of oceanic chlorophyll particles are utilized in the following comparisons.

In the simulation of the $R_{rs}(0^+, \lambda)$, the volume phase function of oceanic chlorophyll pigments is first assumed to be the phase function measured by Petzold [77], referred to as the Petzold phase function below. In addition to the phase function, the scattering and absorption coefficients of oceanic waters follow those specified by the two bio-optical models, respectively. Comparison at 670 nm is shown in Figure 4.2. One sees that when the scattering and absorption coefficients in the Siegel model are used the simulated $R_{rs}(0^+, 670)$ values are larger than the measured ones at the majority of observed points when the chlorophyll concentration is larger than 10.0 mg·m^{-3}. When the scattering and absorption coefficients in the Tanaka model are used in the simulation, the measured $R_{rs}(0^+, 670)$ are more accurately estimated by the simulations at the majority of the observed points. This indicates that the optical properties of chlorophyll pigments used in the Tanaka

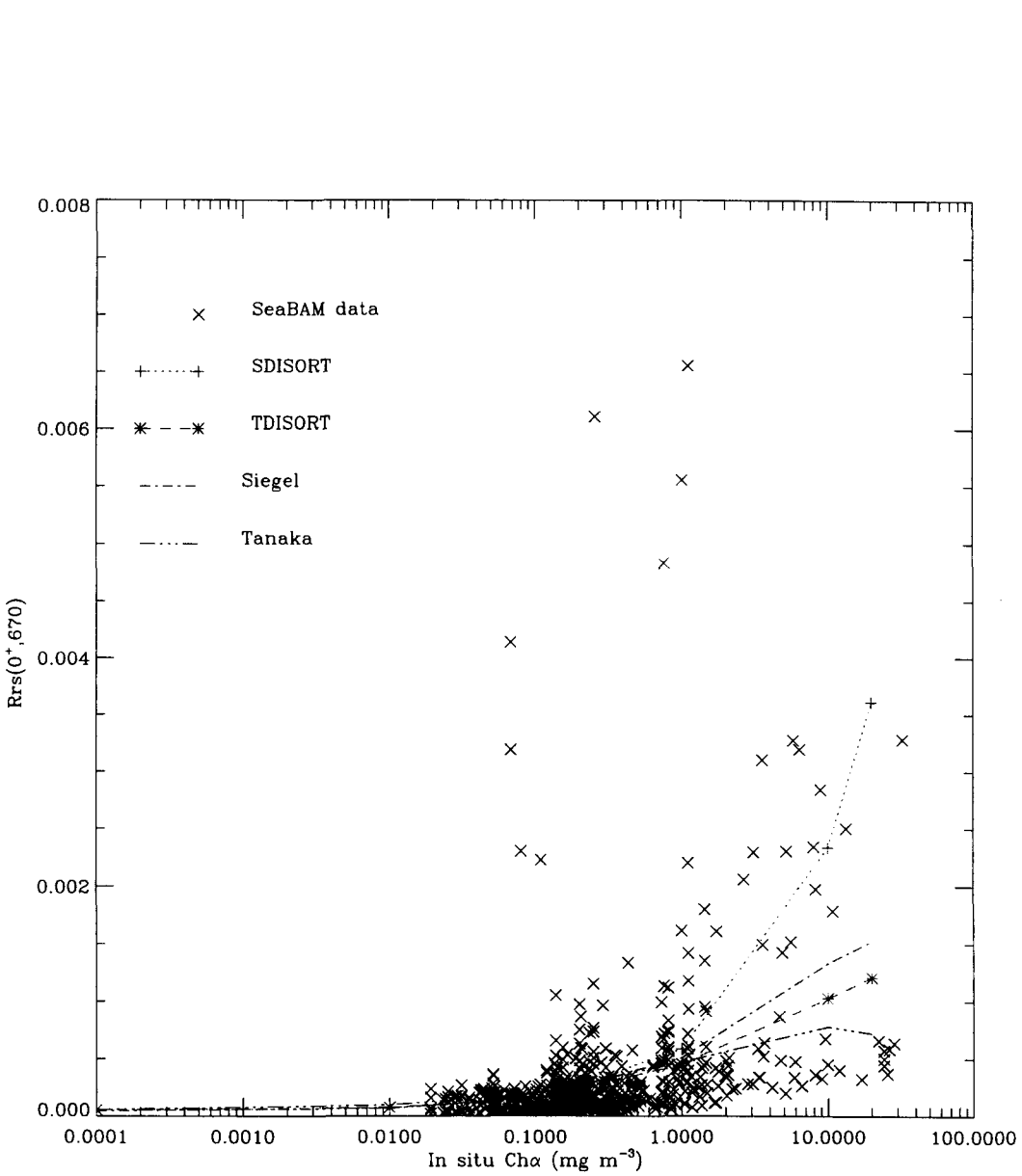

Figure 4.2 Comparison of the nadir $R_{rs}(0^+, 670nm)$ between the results computed by two bio-optical models and adopted from SeaBAM data. Results simulated by the DISORT code for the coupled atmosphere-ocean system for the volume phase function measured by Petzold [82] are also shown. 'SeaBAM' denotes the results inferred from the SeaBAM measurements; 'SDISORT' denotes the results simulated by the DISORT code with optical properties defined by the Siegel model and 'TDISORT' is similar to 'SDISORT' except for the Tanaka model; 'Siegel' results computed by the Siegel model and 'Tanaka' by the Tanaka model.

model are more reasonable than those used in Siegel model and that different scattering and absorption coefficients lead to large differences in the remote sensing reflectance simulated by the radiative transfer model for the same volume phase function. Figure 4.3 shows a comparison of the $R_{rs}(0^+, \lambda)$ computed using the bio-optical models and simulated by the DISORT code at λ = 765 and 865 nm, respectively, when the Petzold phase function is used in the simulations. The conclusions are similar to those arrived at for 670 nm. At all of these wavelengths, one sees that the values of $R_{rs}(0^+, \lambda)$ computed by Siegel model are larger than those computed by Tanaka model.

A phase function compatible with the backscattering coefficients of the oceanic chlorophyll pigments specified by two bio-optical models is then employed in the simulations. For a given volume phase function, the backscattering coefficient can be computed by [64]

$$b_b = 1/2 \sum_{l=0}^{2N-1} (-1)^l (2l+1) x_l \left[\int_0^1 d\mu P_l(\mu) \right]^2 \tag{4.17}$$

where $P_l(\mu)$ is the lth Legendre polynomial and x_l (the moment of the phase function) is given by

$$x_l = 1/2 \int_{-1}^{+1} d(cos\Theta) P_l(cos\Theta) p(cos\Theta). \tag{4.18}$$

Here $p(cos\Theta)$ is the phase function and Θ is the scattering angle. For example, for the Henyey-Greenstein (HG) phase function given by [64]

$$p(cos\Theta) = \frac{1 - g^2}{(1 + g^2 - 2g cos\Theta)^{3/2}}, \tag{4.19}$$

x_l is given by g^l, where g is the asymmetry factor.

By requiring the Henyey-Greenstein phase function to yield the same backscattering coefficient as that used in the two bio-optical models, we may determine the asymmetry factor, g. When the *Chl* is in the range between 0.01 and 20.0

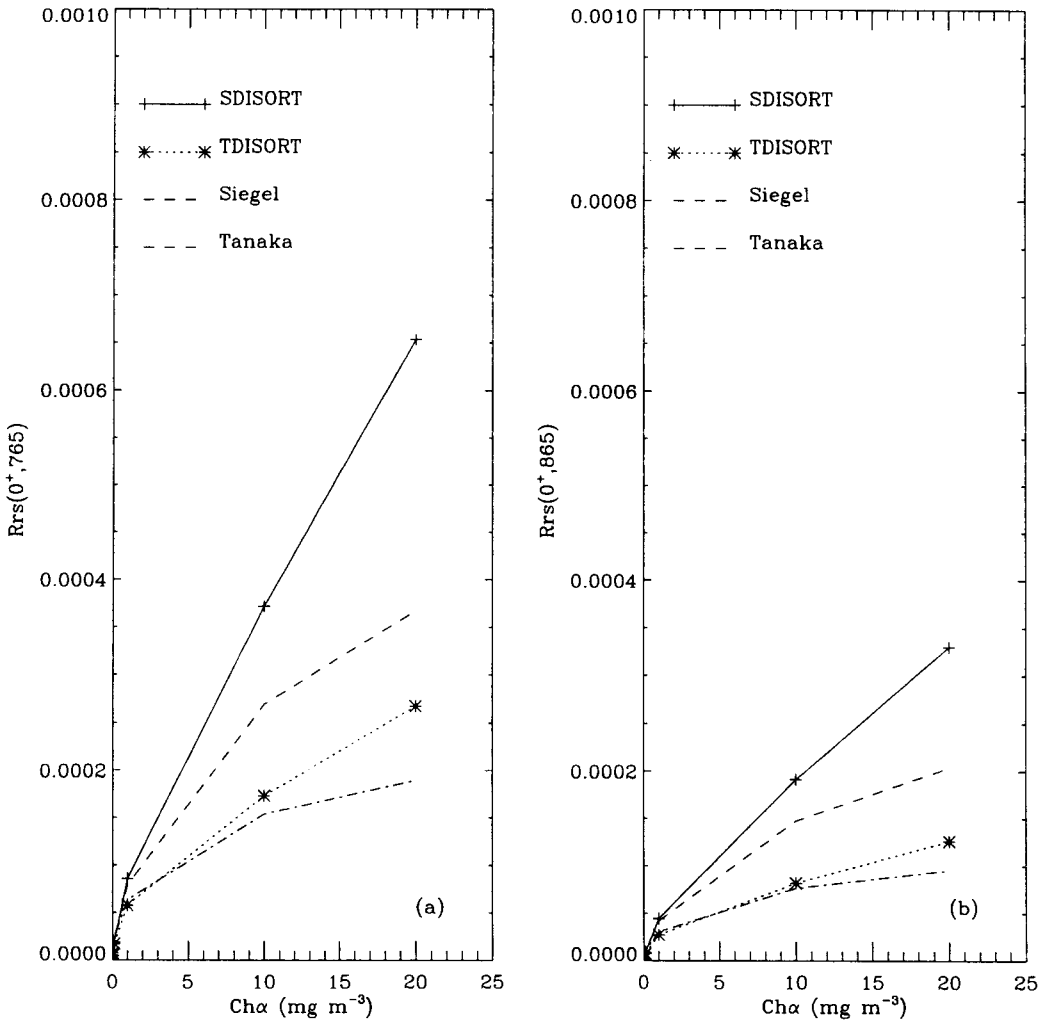

Figure 4.3 Comparison of the $R_{rs}(0^+, \lambda)$ computed by the bio-optical models and simulated by the DISORT code at $\lambda = 765$ and 865 nm, respectively. The Petzold phase function is used in the simulations. The descriptions of the legends used in the figures are the same as those in Fig. 4.2. (a) 765 nm. (b) 865 nm.

$mg{\cdot}m^{-3}$, the simulated asymmetry factor for three NIR wavelengths (670, 765 and 865 nm) lies between 0.98 and 0.997, depending on the chlorophyll concentration and the wavelength. Based upon these fitted HG phase functions, the simulated $R_{rs}(0^+, 670)$ (which are not shown here) are generally small compared to the measured values for the majority of the observed points as well as to the values computed by the two bio-optical models when the *Chl* is larger than 10.0 mgm^{-3}. For small *Chl*, the simulated $R_{rs}(0^+, 670)$ are comparable to the measured and computed ones. This shows the relative insensitivity of the $R_{rs}(0^+, 670)$ to the phase function of chlorophyll pigments at small *Chl*. At 765 and 865 nm, similar conclusions are obtained. The large asymmetry factor for the fitted HG phase functions used in the above simulations is responsible for this underestimation of the measured $R_{rs}(0^+, \lambda)$. We note that the asymmetry factor for the Petzold phase function is about 0.924 [21]. This underscores the significance of the phase function in addition to the scattering and absorption coefficients. On the other hand, one should be aware of limitations inherent in using a synthetic one-parameter phase function, and the uncertainty involved in fitting the HG phase function to a very small backscattering coefficient. This implies that it is of importance to measure accurately the phase function of oceanic chlorophyll pigments.

4.3.1.3 Sensitivity of the nadir NIR remote sensing reflectance to the phase function of oceanic particles

Due to the significance of the phase function of oceanic waters in determining the remote sensing reflectance, its effect on the remote sensing reflectance just above (below) the ocean surface is further simulated and discussed. A few measurements of the phase functions for chlorophyll species in the ocean including Case-I and Case-II water exist [77, 78]. Volten *et al.* (1998) measured a set of volume phase functions for 16 phytoplanktonic species [78]. These measurements were carried

out at 633 *nm* and are available only for scattering angles between 20° and 160°. An approximate estimate of the asymmetry factor for these phase functions shows that it frequently lies between 0.92 and 0.98, if the pattern of the volume phase function beyond the available scattering angles is assumed to be same as that of the Petzold phase function. Figure 4.4 shows the $R_{rs}(0^+, \lambda)$ simulated by the DISORT code at wavelengths of 670, 765 and 865 nm as a function of the asymmetry factor at 10.0 mg·m^{-3}. $R_{rs}(0^+, \lambda)$ values computed by the two bio-optical models, which are constant when the *Chl* and wavelength are specified, are shown for the comparison. It is found that the volume phase function of chlorophyll particles significantly affects the remote sensing reflectance when the other optical properties of ocean water are the same. From these simulations, we may determine a set of asymmetry factors for which the simulated $R_{rs}(0^+, \lambda)$ values are equivalent to the ones computed by the two bio-optical models at the same *Chl* value and wavelength. For example, for the Siegel model, at 10.0 mg·m^{-3} the asymmetry factors at 670, 765 and 865 nm determined in this manner are 0.955, 0.945, 0.942, respectively, as may be easily inferred from Fig. 4.4. At 1.0 mg·m^{-3} the asymmetry factors at 670, 765 and 865 nm become 0.92, 0.918, 0.917, respectively; at 20.0 mg·m^{-3} the asymmetry factors become 0.965, 0.957, 0.955, respectively (not shown here).

4.3.1.4 Sensitivity of the nadir NIR remote sensing reflectance to solar zenith angle

The above simulations of the nadir remote sensing reflectance above the ocean surface were carried out for a solar zenith angle of 45°. When we change the solar zenith angle, the $R_{rs}(0^+, \lambda)$ will change. For example, when the *Chl* varies between 1.0 and 20.0 mg·m^{-3} and the solar zenith angle varies between the range 0 and 85 °, the $R_{rs}(0^+, \lambda)$ at the solar zenith angle of 85 ° increases by up to 48 % compared to

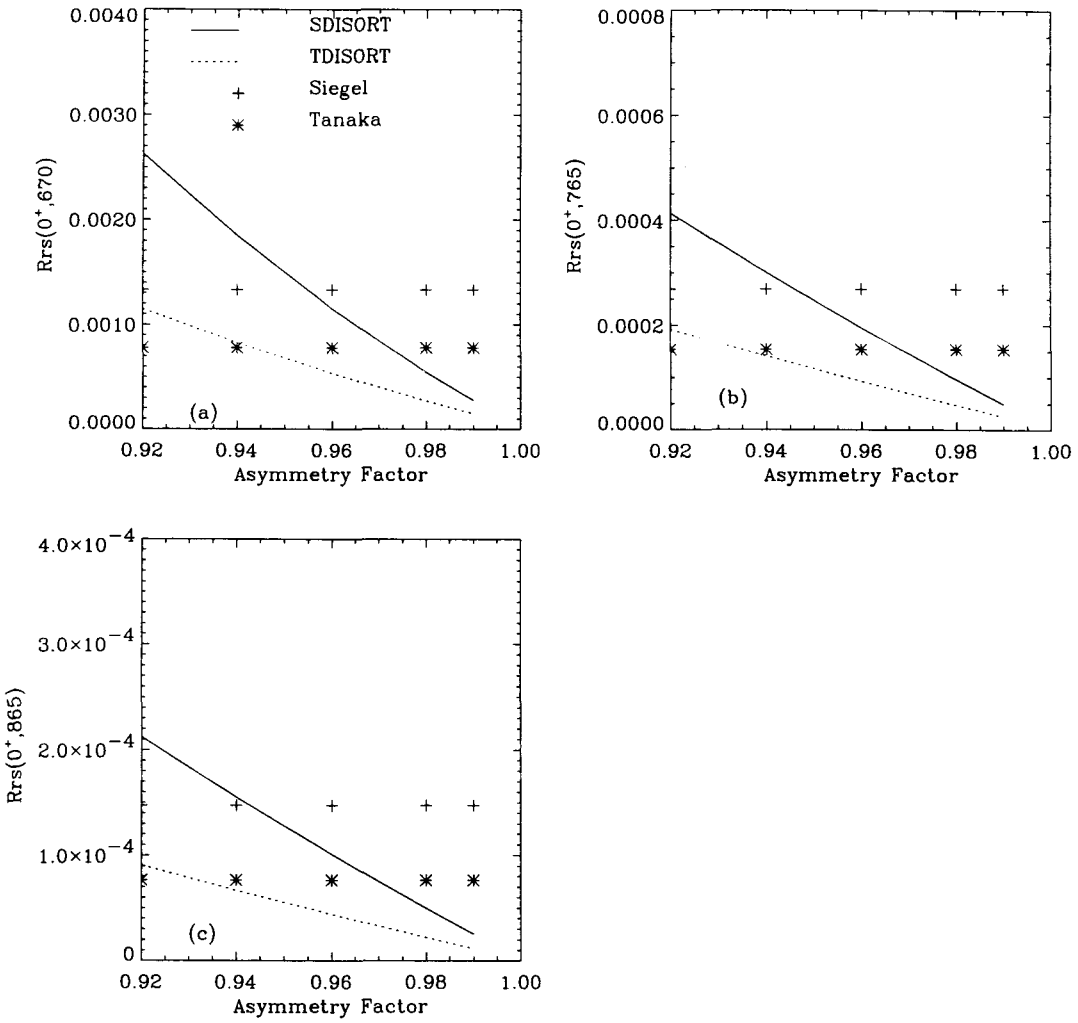

Figure 4.4 Comparison of the $R_{rs}(0^+, \lambda)$ computed using the bio-optical models with that simulated by the DISORT code at λ = 670, 765 and 865 nm, respectively, where the Chl = 10.0 mg·m^{-3}. In the simulations by the DISORT code the HG phase function is assumed. The description of the legends are the same as those in Fig. 4.2. (a) λ = 670 nm. (b) λ = 765 nm. (c) λ = 865 nm.

that at the solar zenith angle of 0 ° and the Q factor (see below) at nadir increases by up to 27 %, depending on wavelength and chlorophyll concentration. Fig. 4.5 shows the $R_{rs}(0^+, \lambda)$ at 670, 765 and 865 nm as a function of solar zenith angle at $Chl = 10.0$ mg·m^{-3} for the Petzold phase function. This figure shows that the dependence of $R_{rs}(0^+, \lambda)$ on the solar zenith angle is not negligible.

4.3.2 Numerical simulations of the bi-directional properties of the remote sensing reflectance in the NIR

In addition to the above uncertainty in computing the nadir $R_{rs}(0^+, \lambda)$, the bi-directional characteristics of the remote sensing reflectance are important because the upward radiance just below the ocean surface derived from the two bio-optical models will be used in the computation of the top-of-atmosphere (TOA) reflectance through the multiple scattering process in the atmosphere. Morel et al. studied the bi-directional reflectance of oceanic waters for wavelengths between 450 and 600 nm by assessing the value of the Q factor (in steradians) relating the upward radiance $L_u(\theta, \phi)$ to the upwelling irradiance E_u at the same depth [14],

$$L_u(z, \theta, \phi, \lambda) = E_u(z, \lambda)/Q(z, \theta, \phi, \lambda). \tag{4.20}$$

At z = 0^- (just below the ocean surface), Eq. (4.20) is rewritten as (z = 0^- is omitted in the Q factor)

$$Q(\theta, \phi, \lambda) = E_u(0^-, \lambda)/L_u(0^-, \theta, \phi, \lambda). \tag{4.21}$$

Thus, the Q factor indicates the bi-directional dependence of the water-leaving radiance. We simulated the Q factor just below sea surface at three NIR bands by employing the radiative transfer model. In the simulations the scattering and extinction coefficients (single scattering albedo as well) specified by the bio-optical models and Petzold phase function are used.

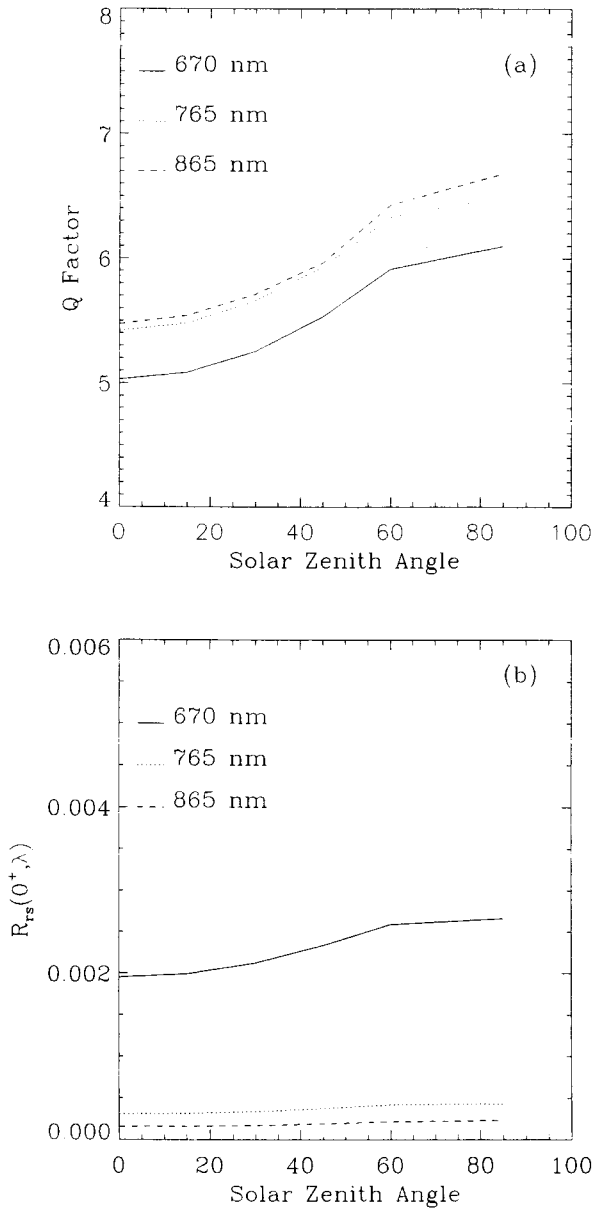

Figure 4.5 The Q factor and the $R_{rs}(0^+, \lambda)$ as a function of the solar zenith angle at $\lambda = 670$, 765 and 865 nm when the $Chl = 10.0$ mg·m^{-3}. The scattering and absorption coefficients used in the bio-optical models and the measured Petzold phase function are employed in the computation of $R_{rs}(0^+, \lambda)$ using the DISORT code for the coupled atmosphere-ocean system. (a) Q factor at nadir. (b) $R_{rs}(0^+, \lambda)$.

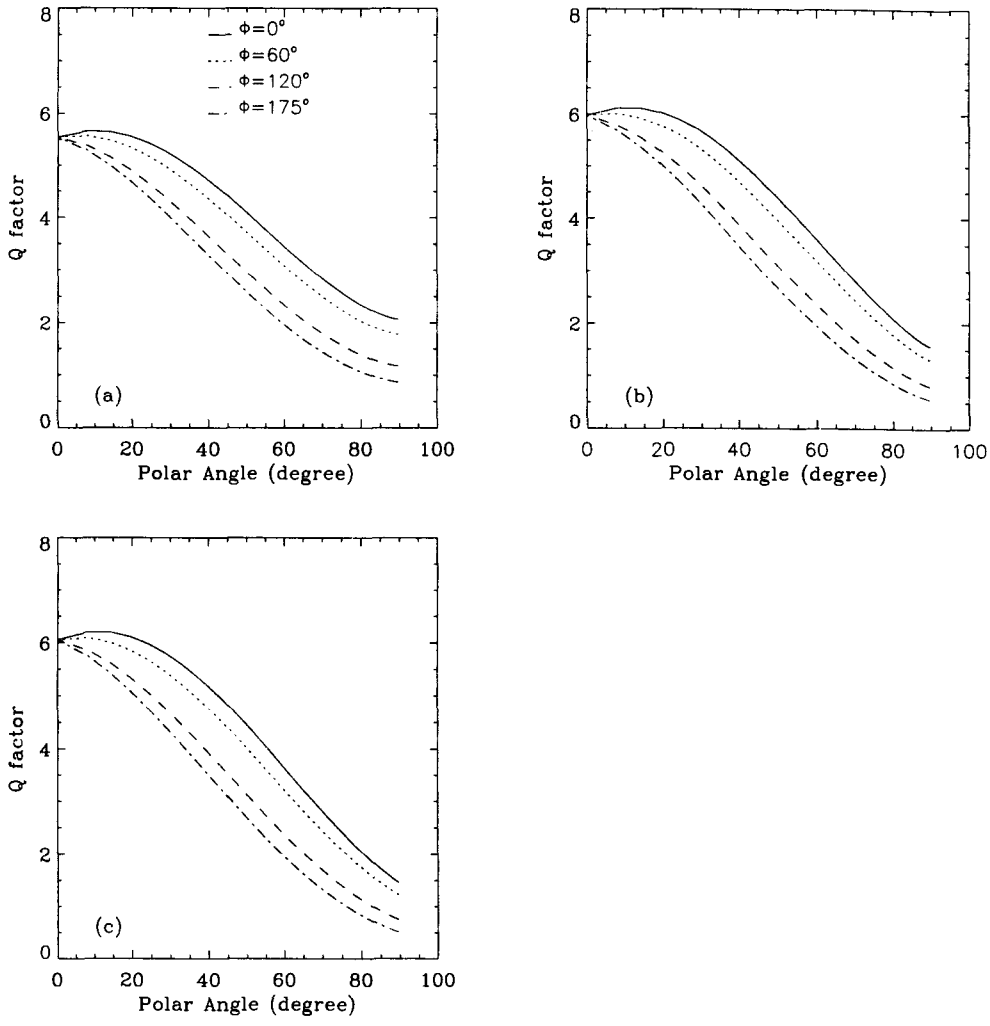

Figure 4.6 The dependence of the Q-factor on the polar angle at different azimuthal angles (0, 60, 120 and 175°). (a) 670 nm. (b) 765 nm. (c) 865 nm.

Figure 4.6 shows the dependency of the Q factor on the polar angle for several azimuthal angles. As mentioned by Morel et al. [14], the largest Q values are found in the vicinity of nadir, while the smallest ones occur in the horizontal direction ($\theta = \pi/2$). This implies that the upward remote sensing reflectance just below the ocean surface is the smallest at nadir. The difference between the maximum and the minimum in the upward radiance just below the surface is as large as a factor of six. Thus, the isotropic assumption invoked in determining the values of the remote sensing reflectance is significantly violated. When the HG phase functions with asymmetry factors of 0.92 and 0.99 are employed, similar conclusions are obtained except for slightly different numerical values. In view of this large bi-directional dependence of the $R_{rs}(0^-, \lambda)$ it becomes important to assess the effect of the isotropic assumption on the TOA NIR water-leaving radiance.

4.4 Implication for ocean color retrieval

An important use of the above bio-optical models for the NIR remote sensing reflectance just below the ocean surface is in the computation of the TOA NIR water-leaving radiance as required for the ocean color retrieval. In the presence of chlorophyll particles in the ocean, the satellite-measured reflectance, after the removal of contributions from glitter patterns and whitecaps, is given by [70]

$$\rho_{tot}(\lambda) = \rho_{path}(\lambda) + t\rho_w(\lambda), \tag{4.22}$$

where $\rho_{path}(\lambda)$ is the atmospheric contribution, $\rho_w(\lambda)$ the water-leaving reflectance, and t the atmospheric diffuse transmittance. We define the reflectance as the radiance normalized by the extraterrestrial solar irradiance, i.e. $\rho = \pi \mathrm{I}/\mathrm{F_0}\cos\theta_0$, where I is the measured radiance, $\mathrm{F_0}$ is the extraterrestrial solar irradiance, and θ_0 is the solar zenith angle.

Then the TOA water-leaving reflectance is determined by

$$t\rho_w(\lambda) = \rho_{tot}(\lambda) - \rho_{path}(\lambda). \tag{4.23}$$

Usually, when the *Chl* is smaller than 1.0 mg·m^{-3}, the water-leaving reflectance just below the ocean surface ($\rho_w(\lambda)$) or the TOA water-leaving reflectance ($t\rho_w(\lambda)$) at NIR is negligible [15, 16]. However, $\rho_w(\lambda)$ is not negligible when the *Chl* is larger than this value. Siegel et al. [16], considered this non-negligible $t\rho_w(\lambda)$ in the atmospheric correction algorithm for SeaWiFS imagery. Based on a bio-optical model for the NIR remote sensing reflectance and the assumption that $\rho_w(\lambda)$ is isotropic, Siegel et al. demonstrated that it is important not to assume that $\rho_w(\lambda) = 0$ in the NIR if the chlorophyll concentration is sufficiently large. Unfortunately, the above analyses in this study show: 1) the NIR remote sensing reflectance ($R_{rs}(0^+, \lambda)$) varies by up to 48 % with the solar zenith angle for a given wavelength and chlorophyll concentration when other inputs are the same; 2) the NIR remote sensing reflectance just above (below) the ocean surface are strongly bi-directional (the variation in the remote sensing reflectance with the polar angle is almost 600 %) , i.e., the isotropic assumption in determining the values of the remote sensing reflectance is dramatically violated. Since the second error is much larger than the first one, here we assess the TOA water-leaving reflectance deviation at NIR caused by the isotropic assumption. As a demonstration, the deviation is quantified based upon the Siegel model because it is in operational use for SeaWiFS imagery. Finally, we quantify the deviation in the ratios $\epsilon(765, 865)$ employed to retrieve the aerosol model and aerosol optical depth for non-absorbing or weakly absorbing aerosols [70], and $\gamma(765)$ employed to retrieve the aerosol model and aerosol optical depth for absorbing aerosols [13], as mentioned above.

4.4.1 TOA water-leaving reflectance deviation in the NIR

For convenience, we rewrite the TCA water-leaving reflectance $t\rho_w(\lambda)$ as ${\rho_w}^{TOA}(\lambda)$, i.e.,

$$ {\rho_w}^{TOA}(\lambda) = t\rho_w(\lambda). \tag{4.24} $$

To introduce the TOA water-leaving reflectance deviation caused by invoking the isotropic assumption in computing the water-leaving radiance, we first define the TOA water-leaving reflectances ${\rho_w}^{Iso,TOA}(\lambda)$ and ${\rho_w}^{True,TOA}(\lambda)$ as follows.

1) The TOA water-leaving reflectance resulting from the isotropic assumption, i.e., ${\rho_w}^{Iso,TOA}(\lambda)$, is defined as the TOA water-leaving reflectance computed by the DISORT code when the water-leaving radiance just below the ocean surface (0^-) is assumed to be isotropic and replaced by the $L_w(0^-, \lambda)$ at nadir computed by the Siegel model, i.e.,

$$ L_w(0^-, \theta, \lambda) = L_w(0^-, \lambda) = E_u(0^-, \lambda) R_{rs}(0^-, \lambda). \tag{4.25} $$

Here $R_{rs}(0^-, \lambda)$ is determined by Eq. (4.7), and $E_u(0^-, \lambda)$ is the downward irradiance at 0^- computed by the DISORT code for the same optical properties (scattering and absorption coefficients) as in the Siegel model and for the HG phase function with an asymmetry such that the $R_{rs}(0^-, \lambda)$ at nadir computed by the DISORT code is the same as to that computed by the Siegel model (see section 4.3).

2) The TOA water-leaving reflectance in the absence of the isotropic assumption, i.e., ${\rho_w}^{True,TOA}(\lambda)$, is defined as TOA water-leaving reflectance computed by the DISORT code when the angular distribution of the water-leaving radiances at 0^- are taken into accounted in the computation, and the optical properties used in the computation are the same as those are used in 1).

Thus, the deviation between the ${\rho_w}^{Iso,TOA}(\lambda)$ and ${\rho_w}^{True,TOA}(\lambda)$ shows the effect of invoking the isotropic assumption in computation of the water-leaving

radiances at 0^- on the TOA water-leaving radiance (reflectance). The relative deviation is defined as

$$\Delta {\rho_w}^{TOA}(\lambda) = ({\rho_w}^{Iso,TOA}(\lambda) - {\rho_w}^{True,TOA}(\lambda)) * 100.0/{\rho_{tot}}^{True,TOA}(\lambda) \quad (4.26)$$

where

$${\rho_w}^{True,TOA}(\lambda) = {\rho_{tot}}^{True}(\lambda) - \rho_{path}(\lambda) \quad (4.27)$$

and

$${\rho_w}^{Iso,TOA}(\lambda) = {\rho_{tot}}^{Iso}(\lambda) - \rho_{path}(\lambda). \quad (4.28)$$

Note that the TOA water-leaving reflectance is computed as the difference between the TOA reflectance over the ocean containing chlorophyll particles and over pure water. Thus, by running the DISORT code defined by the items 1) and 2) above we compute, the TOA reflectance with and without the isotropic assumption, i.e., ${\rho_{tot}}^{True}(\lambda)$ and ${\rho_{tot}}^{Iso}(\lambda)$, respectively. The computation of the $\rho_{path}(\lambda)$ is obtained by running the DISORT code over pure water, which implies that the ocean is approximately black in the NIR.

The analyses in section 4.3 show that the remote sensing reflectance at nadir is a minimum compared to its value at other polar angles (see Fig. 4.6 where one notes that a large Q factor implies a small remote sensing reflectance). This implies the use of the isotropic assumption in computing the water-leaving radiance just below the ocean surface based upon the value at nadir would cause an underestimation of the TOA water-leaving radiance, i.e., it would imply a negative deviation in the TOA water-leaving radiance (reflectance). Our simulations show that this deviation depends on chlorophyll concentration, wavelength, and aerosol optical depth. When the *Chl* is smaller than 10 mg·m^{-3}, the deviation at 765 and 865 nm is negligible regardless of the aerosol optical depth. When the *Chl* varies between the 10 and 20.0 mg·m^{-3}, the deviation at these two NIR wavelengths is between

-1 and -3 %, which will cause a non-negligible effect on the atmospheric correction and ocean color retrieval in the visible bands. At 670 nm, when the *Chl* varies between 1.0 and 20.0 mg·m^{-3}, the deviation lies between -1.0 and -9.0 % depending upon the aerosol optical depth. Figure 4.7 shows the TOA water-leaving reflectance deviation at 670 and 765 nm when Coastal aerosols at the relative humidity of 90 % [9] and the aerosol optical depth at 865 nm of 0.1 are included in the atmosphere, and the *Chl* is 20 mg·m^{-3}. For Urban aerosols, the conclusion will be slightly different. Thus, these results show that when the *Chl* is 10.0 mg·m^{-3} or larger, use of the isotropic assumption in determining the values of the remote sensing reflectance or water-leaving reflectance will cause a non-negligible deviation in the TOA water-leaving reflectance at NIR. This deviation will cause a deviation in the ratio to be used to retrieve the aerosol model and the aerosol optical depth.

4.4.2 Deviation in the $\epsilon(765, 865)$ and $\gamma(765)$

The atmospheric contribution to the TOA radiance stems from three components: molecules, aerosols and the interaction between the molecules and aerosols [70]. The contribution from atmospheric molecules can be accurately computed [70], so the inaccuracy in the atmospheric contribution is due to aerosols. In practice, the atmospheric correction in the visible is based upon an aerosol model and a corresponding optical depth retrieved in the NIR and then extrapolated into the visible. Algorithms for atmospheric correction over Case-I waters usually employ ratios aimed at isolating the aerosol contribution to the TOA radiance from the molecular contribution. Such ratios are used to select an aerosol model and a corresponding optical depth in the NIR. Subsequently they are used to extrapolate the atmospheric contribution to the TOA radiance from the NIR into the visible. The current operational SeaWiFS algorithm employs the ratio [70]

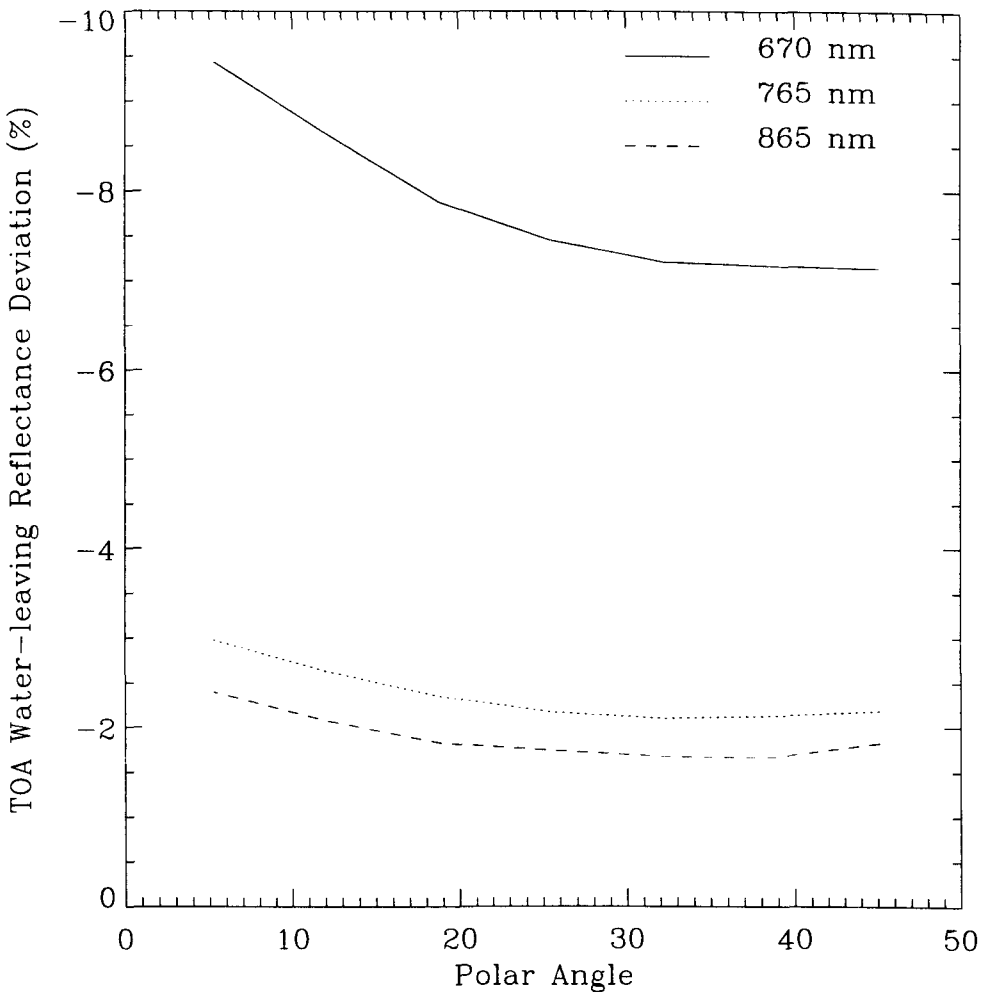

Figure 4.7 TOA water-leaving reflectance deviation as a function of the polar angle when Coastal-90 aerosols with an aerosol optical depth at 865 nm of 0.1 are included in the atmosphere, *Chl* is 20 $mg \cdot m^{-3}$, and the asymmetry factor at 670m 765 and 865 are 0.955, 0.945, 0.942, respectively. The HG phase function is assumed.

$\epsilon(\lambda, 865) = \rho_{ms}(\lambda)/\ \rho_{ms}(865)$, where $\rho_{ms}(\lambda) = \rho_{path}(\lambda) - \rho_r(\lambda)$ and $\rho_{path}(\lambda)$ is the total atmospheric contribution and $\rho_r(\lambda)$ the atmospheric molecular contribution to the TOA (satellite-measured) reflectance. The ratio $\gamma(\lambda) = \rho_{path}(\lambda)/\rho_r(\lambda)$ has been used for atmospheric correction purposes in the presence of strongly absorbing aerosols [13].

As a demonstration, we introduce the deviation in $\epsilon(765, 865)$ and $\gamma(765)$ (%) as

$$\Delta\epsilon(765, 865) = \frac{\left[\epsilon^{Iso}(765, 865) - \epsilon^{True}(765, 865)\right] * 100.0}{\epsilon^{True}(765, 865)} \tag{4.29}$$

where

$$\epsilon^{Iso}(765, 865) = \frac{\rho_{ms}(765) + \Delta\rho_{tot}(765)}{\rho_{ms}(865) + \Delta\rho_{tot}(865)} \tag{4.30}$$

and

$$\epsilon^{True}(765, 865) = \frac{\rho_{ms}(765)}{\rho_{ms}(865)} \tag{4.31}$$

with

$$\Delta\rho_{tot}(\lambda_{NIR}) = \rho_{tot}{}^{True}(\lambda_{NIR}) - \rho_{tot}{}^{Iso}(\lambda_{NIR}) \tag{4.32}$$

where the $\Delta\rho_{tot}(\lambda_{NIR})$ denotes the difference in the NIR TOA water-leaving reflectance due to the use of the isotropic assumption when computing the water-leaving radiances just below the ocean surface. Unless it is properly corrected this difference may lead to the retrieval of incorrect aerosol optical properties.

Similarly, we introduce

$$\Delta\gamma(765) = \frac{(\gamma^{Iso}(765) - \gamma^{True}(765)) * 100.0}{\gamma^{True}(765)} \tag{4.33}$$

where

$$\gamma^{Iso}(765) = \frac{\rho_{path}(765) + \Delta\rho_{tot}(765)}{\rho_r(765)} \tag{4.34}$$

and

$$\gamma^{True}(765) = \frac{\rho_{path}(765)}{\rho_r(765)}. \tag{4.35}$$

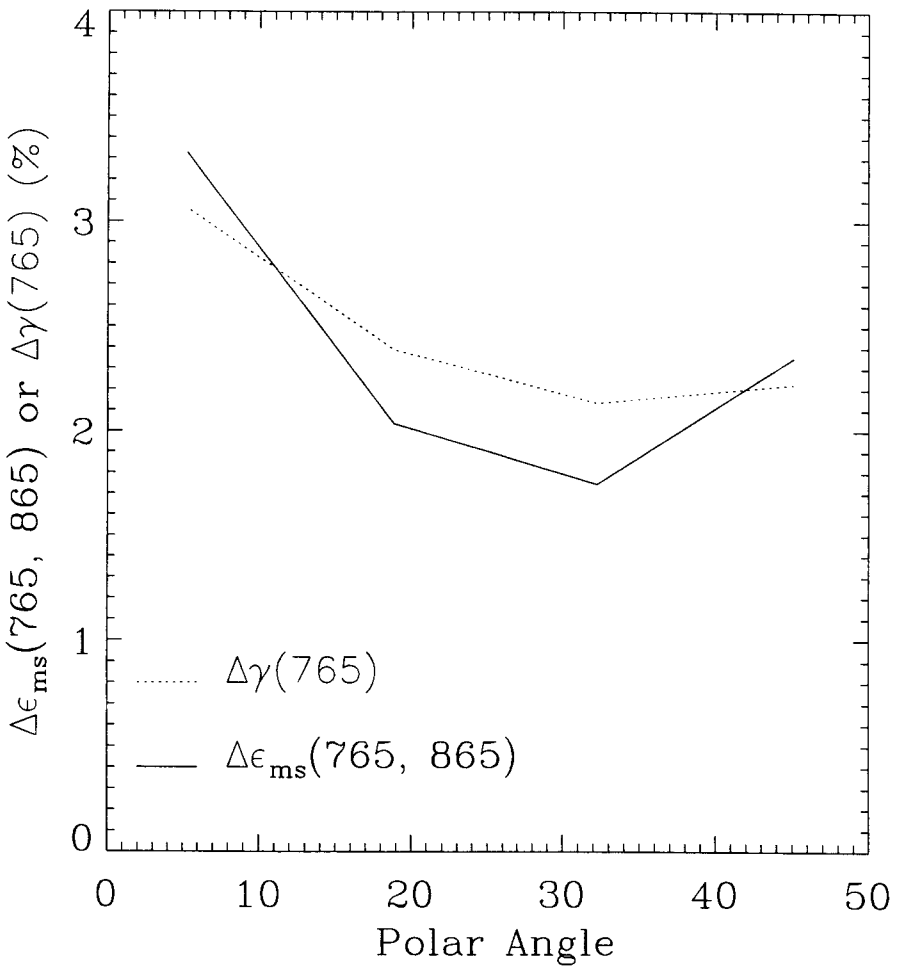

Figure 4.8 Same as Fig. 4.7 but for the deviation of $\epsilon(765, 865)$ and $\gamma(765)$.

Figure 4.8 displays the deviations $\Delta\epsilon(765, 865)$ and $\Delta\gamma(765)$ for the same inputs as those used in Fig. 4.7. We note that when *Chl* is 20.0 mg·m^{-3}, the deviation in the $\epsilon(765, 865)$ and $\gamma(765)$ is up to + 3 %. These ratios are employed to retrieve an aerosol model and a corresponding NIR optical depth that is extrapolated into the visible region and used to estimate the small TOA water-leaving radiance in the visible region.

Even in Case-I waters, the concentration of oceanic chlorophyll particles may vary between 0.01 (very clear water) and 100.0 mg·m^{-3} (very turbid water) [21]. This implies that the NIR bi-directional properties of the water-leaving radiance just below the ocean surface must be taken into account in the atmospheric correction of the ocean color imagery when the oceanic chlorophyll concentration is larger than 10.0 mg·m^{-3}.

4.5 Conclusions

Appreciable efforts have been expended on the application of the bio-optical models for the remote sensing reflectance in the visible to convert the optical properties into other parameters of interest such as chlorophyll concentration, colored dissolved organic matter, and inorganic particle concentrations [19, 80, 79]. However, less attention has been paid to the performance of the bio-optical models for the NIR remote sensing reflectance (water-leaving reflectance) and the resulting effects of uncertainties in the model on the ocean color retrieval. In this chapter the DISORT code for the coupled atmosphere-ocean system is employed to assess numerically the performance of the bio-optical model for the remote sensing reflectance at NIR bands developed by Gordon et al. and used by Siegel et al. The performance of the model developed by Tanaka et al. is also evaluated. The measured nadir remote sensing reflectance at 670 nm just below the ocean surface assembled in

the SeaBAM data base is employed to evaluate the performance of two bio-optical models. Some important conclusions are obtained as follows:

1) Compared to the measured $R_{rs}(0^-, 670)$ (at nadir) available in the SeaBAM data base, the bio-optical model adopted by Siegel and co-workers slightly over-estimates the measured values for the majority of the observed points, while the model adopted by Tanaka and his co-workers yield values in closer agreement with the measured ones for the majority observed points.

2) By employing the same absorption and scattering coefficients defined by two bio-optical models and the Petzold phase function, we found that $R_{rs}(0^-, 670)$ values simulated by the DISORT code for the coupled atmosphere-ocean system using optical properties based upon the Siegel model are much larger than those computed by the Siegel model. However, $R_{rs}(0^-, 670)$ values simulated by the DISORT code using optical properties based upon the Tanaka model are approximately equivalent to those computed by the Tanaka model. This implies that the absorption and scattering coefficients used in the Tanaka model may more properly describe the optical properties of chlorophyll particles in Case I water.

3) Strong bio-directional characteristics of the NIR remote sensing reflectance just below the ocean surface are found in the simulations. Thus the bi-directional dependence of the NIR water-leaving radiance just below the ocean surface needs to be taken into account in the retrieval of ocean color imagery. When the chlorophyll concentration is larger than 10.0 $mg \cdot m^{-3}$, the TOA NIR water-leaving reflectance deviation caused by the isotropic assumption is non-negligible and should be considered in atmospheric correction of ocean color imagery.

Chapter 5

The role of oceanic air bubbles in atmospheric correction of ocean color imagery

5.1 Introduction

Retrieval of marine constituents from ocean color imagery is an important and challenging task in the field of remote sensing. The spectral distribution of light emanating from the ocean determines its color. This light is due to solar radiation that has been subject to absorption and scattering by molecules and particles in the water column. The light that originates in the ocean in this manner and leaves the water column through the air-water interface is called the water-leaving radiance. Since water molecules and particles not only scatter but also absorb light, the water-leaving radiance carries information about both absorption and scattering processes that can be used to infer the optical properties of the water. A suitable bio-optical model can then be used to convert the optical properties into other parameters of interest such as chlorophyll concentration, colored dissolved

organic matter, and inorganic particle concentration. Retrieval of the water-leaving radiance from satellite-measured radiances relies heavily on accurate removal of the atmospheric contribution to the radiance received by the sensor deployed in space. This removal is called atmospheric correction. Operational algorithms for atmospheric correction are usually based on the so-called black pixel assumption, in which the near-infrared (NIR) water-leaving radiance is taken to be zero. This is true also for the Sea-viewing Wide Field-of-view Sensor (SeaWiFS) [69, 70] although an attempt has recently been made to relax this assumption [16]. Chen *et al.* [15] investigated the validity of the black pixel assumption in atmospheric correction, and concluded that the impact of non-negligible water-leaving radiances at NIR wavelengths on atmospheric correction depends on (i) the ocean particle concentration (e.g. chlorophyll-a), (ii) the scattering characteristics of particles in the near-surface ocean water, described by their shape, size, and refractive-index distribution, which in turn determine the scattering phase function; (iii) the aerosol optical depth; and (iv) the sun-satellite geometry. A question then arises: Can oceanic air bubbles play a role similar to that of oceanic particles in violating the NIR black pixel assumption? In addition to answering this question, it becomes important to assess the contribution of the oceanic air bubbles to the reflectance in the visible at the top-of-the-atmosphere (TOA), which we shall refer to as the TOA water-leaving reflectance for brevity. This contribution must then be distinguished from the chlorophyll contribution to the TOA signal and properly removed.

Oceanic air bubbles can efficiently scatter light and thus contribute to the radiance emanating from the ocean, because they may exist in oceanic waters with a number density in the range of $10^4 - 10^7$ m^{-3} [37, 38, 39, 40, 41]. The potential impact of oceanic air bubbles on ocean color has been recognized. Mobley *et al.* and Bukata discussed qualitatively the optical properties of bubble clouds [21, 42].

Stramski [43] investigated light scattering by submerged bubbles in quiescent seas and compared results of scattering and backscattering coefficients at 550 nm with scattering and backscattering coefficients of bubble-free sea water as estimated from the chlorophyll-based bio-optical models for case 1 waters. Zhang and co-workers [44, 45] found that air bubbles in the ocean are strong scatterers that contribute significantly to the upward radiance, and showed that through enhanced backscattering over the whole visible domain oceanic air bubbles will influence the remote sensing of ocean color by affecting atmospheric correction as well as optical and biological properties derived from color ratios. They concluded that for high bubble concentrations the assumption that there is negligible water-leaving radiance in the NIR would be invalid [45]. Flatau *et al.* derived apparent optical properties of oceanic air bubbles (i.e. the remote sensing reflectance) for the whole solar spectrum and showed that the optical effects of submerged microbubbles on the remote sensing reflectance of the ocean are significant [46]. The above studies constitute the basis for our investigation: to carry out a quantitative assessment of the impact of oceanic air bubbles on atmospheric correction of ocean color imagery.

Atmospheric correction of ocean color imagery is a non-trivial task, and aerosols play a critical role in this context [70, 15]. Therefore, when we assess the effect of oceanic air bubbles on atmospheric correction of ocean color imagery, we must investigate how this effect is influenced by aerosol optical properties such as the wavelength-dependent scattering and absorption coefficients as well as the aerosol optical depth [15].

We employ a discrete-ordinate radiative transfer code for the coupled atmosphere-ocean system [63, 64] to expand the previous studies by assessing the effect of oceanic air bubbles on the water-leaving radiance as well on atmospheric correction of ocean color imagery. Thus, we investigate how oceanic air bubbles affect the black pixel assumption in the NIR region. We also assess the contribution of

oceanic air bubbles to the TOA water-leaving reflectance at visible wavelengths, where it may be mistakenly attributed to chlorophyll unless it is properly identified and removed.

5.2 Optical properties of oceanic air bubbles

Air bubbles in the ocean are mainly generated by injection of air by breaking waves and may form two different structures: clean and coated bubbles. Many studies have already described the optical properties of oceanic air bubbles in terms of number density, size distribution, refractive index, and thickness of the coating film [85, 86, 87, 88, 89, 90, 91, 92, 93, 94, 95, 96]. Useful reviews of the optical properties of oceanic air bubbles may be found in the papers by Zhang *et al.* [45] and by Flatau *et al.* [46].

The majority of the bubbles injected into the surface layers of natural waters are unstable. They either dissolve due to enhanced surface tension and hydrostatic pressure or rise to the air-water interface where they break [92]. However, for oceanic air bubbles with long residence times (i.e. stable microbubbles), a bubble concentration of nearly 2.5×10^{6} m^{-3} with radii in the range 18−355 μm has been reported [87], and bubble concentrations as large as 2.13×10^{7} m^{-3} have been observed [40]. Isao *et al.* [95] observed very large populations of neutrally buoyant bubbles with radii between 0.1 and 1.0 μm. The bubbles are distributed within the top layer of the ocean and observations indicate that the thickness D_b of this layer may vary over a large range between 0.25 and 36 m [39, 41, 92, 93]. There is evidence [46] that individual bubble clouds may reach mean depths of about $4H_s$, where H_s is the significant wave height. But some clouds may extend to about $6H_s$, and bubbles are frequently observed at depths between 1 and 6 m [46]. Based on these results, in our simulations we set the range of the bubble size (radius)

between $r_{min} = 1.0$ and $r_{max} = 300.0$ μm and we assume that the number density of the bubble population lies in the range between 10^5 and 10^8 m^{-3} within the top ocean layer of thickness $D_b = 5$ m.

Observations and modeling results show that the bubbles, even after rising only short distances, are often coated with monolayers and multilayers of particulate materials, which could well explain their anomalous acoustic properties [92]. Thorpe indicated that in nature bubbles acquire organic films quickly after their formation in the sea [90]. Although the composition and the thickness of the coating films are not firmly established, both proteins and lipids are generally considered to be components of the coating film. The mean relative refractive index is 1.10 for lipid and 1.20 for protein [45, 85, 86]. The thickness of such coatings of bubbles in sea water has been estimated to range from 0.01 μm for lipids to 1 μm for proteins [89]. However, existing results show that the optical properties of bubbles, the backscattering in particular, do not change much with increased thickness of the film after it exceeds 0.1 μm [45]. Thus, we set the coating thickness to lie between 0.01 and 0.2 μm in our study.

Based on field observations, the size distribution of oceanic air bubbles is estimated to follow a power law distribution $n(r) = r^{-\alpha}$, where r is the radius of the bubble, and the mean value of α is approximately 4 [39, 88, 94]. Thus, in our study, we assume that the size distribution $n(r)$ of oceanic air bubbles is given by

$$n(r) = \frac{dN(r)}{dr} = c\frac{r_{min}^4}{r^4}, \tag{5.1}$$

where r_{min} is the minimum radius of the bubbles. If N_0 is the total concentration (number density) of bubbles with radii between $r_{min} = 1.0$ and $r_{max} = 300.0$ μm, we find that the coefficient c is approximately $c \approx 3N_0/r_{min}$.

In Fig. 5.1 we show Mie computations of phase functions at 670 nm of lipid- and protein-coated oceanic air bubbles for several coating thicknesses to illustrate

how the scattering phase function of air bubbles depend on composition and coating thickness. For comparison we also show phase functions for a few strongly backscattering phytoplankton species (case 1 and case 2 waters) measured by Volten *et al.* [78]. Measured phase functions of phytoplankton species are only available for scattering angles between 20° and 160°. The asymmetry factor of the phytoplankton species typically lies in the range between 0.9 and 0.99, and thus phytoplankton species show strong forward scattering. The asymmetry factor of oceanic air bubbles lies in the range between 0.76 and 0.86 depending on the wavelength and size distribution. Thus, in comparison to phytoplankton species oceanic air bubbles exhibit much stronger backscattering. Since the optical properties of clean bubbles are very similar to those of coated bubbles with very thin coating thickness (e.g. 0.01 μm in Fig. 5.1), it is sufficient to limit our study to coating thicknesses lying in the range between 0.01 and 0.2 μm.

5.3 Error analysis of atmospheric correction in the presence of oceanic air bubbles

In this study we use the reflectance defined as the radiance normalized by the extraterrestrial solar irradiance, i.e. $\rho = \pi \mathrm{I}/\mathrm{F_0}\cos\theta_0$, where I is the radiance, $\mathrm{F_0}$ is the extraterrestrial solar irradiance, and θ_0 is the solar zenith angle. The contribution of oceanic air bubbles to the water-leaving radiance and in turn to the TOA reflectance measured by the satellite sensor will, unless it is properly accounted for, lead to an error in the inferred water-leaving radiance. The error due to oceanic air bubbles consists of two parts: The first part is due to the direct contribution of the oceanic air bubbles to the TOA water-leaving reflectance at visible wavelengths. If this error is not corrected, the TOA water-leaving reflectance attributed

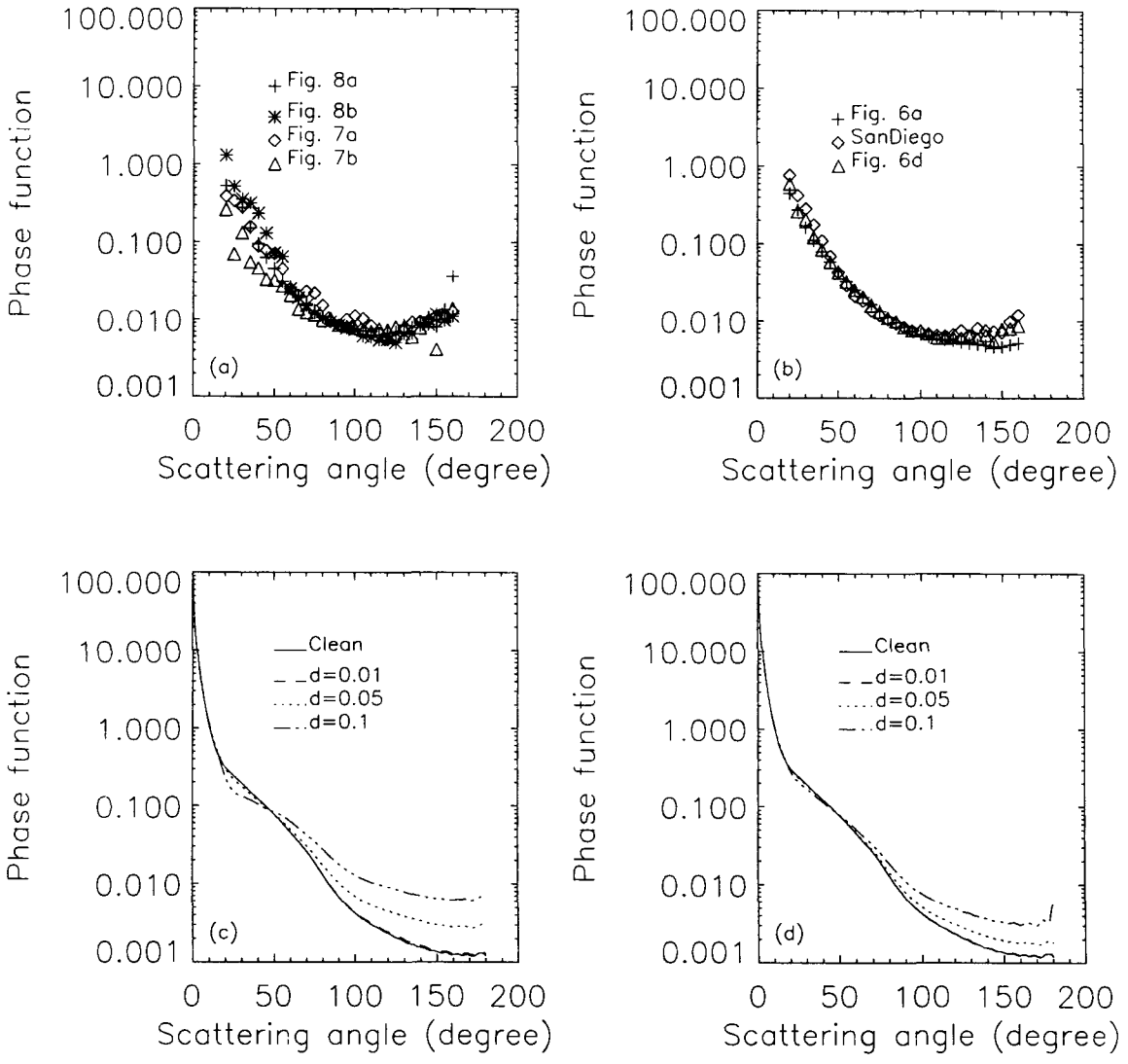

Figure 5.1 Comparison of phase functions of oceanic air bubbles and phytoplankton species. d (μm) denotes the coating thickness used in the computations. (a) Measured phase functions for phytoplankton particles adopted from Fig. 7a, 7b, 8a, and 8b in the paper by Volten *et al.* pigment particles adopted from Fig. 6a, and 6d in the paper by Volten *et al.* (d) Computed phase functions for lipid-coated bubbles.

to chlorophyll will be overestimated. The second part stems from the atmospheric correction procedure because the black pixel assumption in the NIR region will be violated due to the contribution of the oceanic air bubbles to the TOA reflectance.

In the absence of oceanic air bubbles, the satellite-measured reflectance at a visible wavelength λ_{vis} after the removal of contributions from glitter patterns and whitecaps, is given by [70]

$$\rho_{tot}(\lambda_{vis}) = \rho_{path}(\lambda_{vis}) + t\rho_w(\lambda_{vis}), \tag{5.2}$$

where $\rho_{path}(\lambda_{vis})$ is the atmospheric contribution, $\rho_w(\lambda_{vis})$ the water-leaving reflectance in the absence of air bubbles, and t the atmospheric diffuse transmittance. Then the TOA water-leaving reflectance is determined by

$$t\rho_w(\lambda_{vis}) = \rho_{tot}(\lambda_{vis}) - \rho_{path}(\lambda_{vis}). \tag{5.3}$$

When oceanic air bubbles are present, we may define the error E_b in the retrieval of the TOA water-leaving reflectance due to oceanic air bubbles as follows

$$E_b \equiv \Delta[t\rho_w(\lambda_{vis})] = \Delta\rho_{tot}(\lambda_{vis}) - \Delta\rho_{path}(\lambda_{vis}). \tag{5.4}$$

In Eq. (5.4) the first term on the right side, denoted by $\Delta\rho_{tot}(\lambda_{vis})$, is the error due to the extra contribution of the oceanic bubbles to the TOA water-leaving reflectance at visible wavelengths, i.e. the difference between the TOA reflectance in the presence and in the absence of oceanic air bubbles. The second term on the right side of Eq. (5.4), i.e. $\Delta\rho_{path}(\lambda_{vis})$, is the error due to inaccurate assessment of atmospheric contribution in the visible. It is a consequence of inaccurate atmospheric correction caused by inaccurate retrieval of aerosol model and corresponding optical depth resulting from the violation of the black pixel assumption in the NIR due to the oceanic bubbles. If the water-leaving reflectance resulting from oceanic chlorophyll pigments in the NIR is non-negligible, the contribution from

these pigments to the TOA reflectance in the NIR should also be taken into account in this analysis. We circumvent this complication here by setting the chlorophyll concentration low enough that its contribution to the NIR water-leaving radiance can be ignored.

To arrive at an expression for $\Delta\rho_{path}(\lambda_{vis})$, we may start by writing [70]

$$\rho_{path}(\lambda_{vis}) = \rho_{ms}(\lambda_{vis}) + \rho_r(\lambda_{vis}), \tag{5.5}$$

where $\rho_r(\lambda_{vis})$ is the pure Rayleigh component that can be accurately computed (i.e. we can assume $\Delta\rho_r(\lambda_{vis}) = 0$), and $\rho_{ms}(\lambda_{vis})$ is due to the aerosols and the interactions between aerosols and molecules. Thus, the error $\Delta\rho_{path}(\lambda_{vis})$ is from the computation of $\rho_{ms}(\lambda_{vis})$ in Eq. (5.5). The current operational SeaWiFS algorithm employs the ratio $\epsilon_{ms}(\lambda, 865) = \rho_{ms}(\lambda)/\rho_{ms}(865)$ for atmospheric correction of ocean color imagery [70]. By introducing $\epsilon_{ms}(\lambda, 865)$, we may rewrite Eq. (5.5) as follows

$$\rho_{path}(\lambda_{vis}) = \rho_{ms}(865)\epsilon_{ms}(\lambda_{vis}, 865) + \rho_r(\lambda_{vis}). \tag{5.6}$$

Oceanic air bubbles will contribute to the TOA reflectance in the NIR, and thus cause an error $\Delta\rho_{ms}(\lambda_{NIR})$ compared to the reflectance obtained in the absence of oceanic bubbles. This error $\Delta\rho_{ms}(\lambda_{NIR})$ results in an erroneous estimate of $\epsilon_{ms}(765, 865)$ which is used to select an aerosol model and corresponding optical depth for the purpose of atmospheric correction [70]. Since $\epsilon_{ms}(\lambda_{vis}, 865)$ is extrapolated from the NIR to the visible on the basis of this retrieved aerosol model, the erroneous $\epsilon_{ms}(765, 865)$ will lead to an erroneous estimate of $\epsilon_{ms}(\lambda_{vis}, 865)$. Therefore, the error $\Delta\rho_{path}(\lambda_{vis})$ is determined by both $\Delta\rho_{ms}(865)$ and $\Delta\epsilon_{ms}(\lambda_{vis}, 865)$. In the presence of oceanic air bubbles, Eq. (5.6) becomes

$$\rho^B_{path}(\lambda_{vis}) = [\rho_{ms}(865) + \Delta\rho_{ms}(865)]\,[\epsilon_{ms}(\lambda_{vis}, 865) + \Delta\epsilon_{ms}(\lambda_{vis}, 865)] + \rho_r(\lambda_{vis}). \tag{5.7}$$

The difference between Eqs. (5.7) and (5.6), $\Delta\rho_{path}(\lambda_{vis}) = \rho^{B}_{path}(\lambda_{vis}) - \rho_{path}(\lambda_{vis})$, obtained by ignoring the smallest term $\Delta\rho_{ms}\Delta\epsilon_{ms}$ is

$$\Delta\rho_{path}(\lambda_{vis}) \approx \rho_{ms}(865)\Delta\epsilon_{ms}(\lambda_{vis}, 865) + \epsilon_{ms}(\lambda_{vis}, 865)\Delta\rho_{ms}(865). \qquad (5.8)$$

5.4 Assessment of the effect of oceanic air bubbles on atmospheric correction

In this section, we will first assess the TOA reflectance deviation due to the oceanic air bubbles in the spectral range between 412 and 865 nm. From this analysis we will determine the magnitude of the contribution of the oceanic air bubbles to the TOA reflectance. Based on these results, we will then assess the two parts of the error shown in Eq. (5.4). In case 1 waters, the chlorophyll concentration typically lies in the range between 0.01 and 10.0 mg m^{-3} [19, 21, 70]. For simplicity, we use a chlorophyll concentration of 0.5 mg m^{-3} in the ocean in addition to the pure water and oceanic air bubbles in the following simulations, since we focus our attention on assessing the effect of oceanic air bubbles on atmospheric correction of ocean color imagery. This chlorophyll concentration (0.5 mg m^{-3}) is sufficiently low that the black pixel assumption is approximately valid [15].

5.4.1 Selection of input parameters for aerosols and oceanic air bubbles

We adopt the following input for our simulations: (i) For oceanic air bubbles, we adopt 4 number densities 10^5, 10^6, 10^7, and 10^8 m^{-3}, and 5 coating thicknesses between 0.01 and 0.2 μm. The air bubbles are assumed to be distributed uniformly within a surface layer of 5 m thickness just beneath the atmosphere-ocean interface.

The optical properties of the oceanic air bubbles are computed from Mie theory [24]. (ii) For oceanic chlorophyll particles, we adopt a Henyey-Greenstein phase function with an asymmetry factor of 0.99. The oceanic chlorophyll pigments are also assumed to be distributed uniformly within the water column. The other optical properties of chlorophyll pigments (the scattering and extinction coefficients) are adopted from bio-optical models for case 1 waters [67, 97, 98]. (iii) For atmospheric aerosols, we adopt 4 candidate models, and 4 aerosol optical depths for each model. These are the Coastal-90, Maritime-90, Tropospheric-90 and Urban-90 aerosol models, where 90 stands for the relative humidity RH = 90% [9]. The Tropospheric aerosol model consists of weakly absorbing aerosols as follows: 70% water-soluble substance and 30% dust-like aerosols. The Coastal aerosol model contains 99.5% Tropospheric aerosols and 0.5% sea salt aerosols, whereas the Maritime model contains 99.0% Tropospheric aerosol and 1.0% sea salt aerosol. The Urban aerosol model consists of a mixture of weakly absorbing as well as strongly absorbing aerosols as follows: 56% water soluble substance, 24% dust-like aerosols and 20% soot-like aerosols [9]. Thus, Urban-90 represents an aerosol model with relatively strong absorption, while the others contain non-absorbing or weakly absorbing aerosols. The aerosol optical depth at 865 nm (τ_{865}) is utilized to represent the column density of aerosols in the atmosphere. Previous results show that, far from sources of pollution and/or sources of desert aerosols, the aerosol optical depth at 865 nm over the Pacific Ocean lies in the range between 0.08 and 0.11 [99]. Thus, we will adopt $\tau_{865} = 0.05, 0.1, 0.3$ and 0.8 in this study. The aerosols are assumed to be distributed uniformly from the ocean surface to 4 km in the atmosphere. The optical properties are computed from Mie theory for a multi-component mixture of aerosols [24]. (iv) We take the SeaWiFS channels as a reference for studying the wavelength-dependence of the effect of oceanic air bubbles on atmospheric correction. Thus, in this study we use 8 wavelengths at

$\lambda = 412, 443, 490, 510, 555, 670, 765,$ and 865 nm, respectively.

5.4.2 TOA reflectance deviation due to the presence of oceanic air bubbles

We define the TOA reflectance deviation $\Delta\rho^B_{TOA}(\lambda)$ (%) as

$$\Delta\rho^B_{TOA}(\lambda) = \left[\frac{\rho^B_{tot}(\lambda) - \rho_{tot}(\lambda)}{\rho_{tot}(\lambda)}\right] \times 100. \tag{5.9}$$

Here $\rho_{tot}(\lambda)$ is the simulated TOA reflectance in the absence of oceanic air bubbles (i.e. only scattering and absorption by pure water molecules and chlorophyll pigments are included in the ocean), and $\rho^B_{tot}(\lambda)$ denotes the same quantity in the presence of bubbles, while all other conditions are the same.

5.4.2.1 Dependence of the TOA reflectance deviation on the optical properties of the bubbles

The optical properties of the oceanic air bubbles depend on the number density (N_0), the size distribution, and the coating thickness (d) and the refractive index of the coating film. All these parameters will affect the scattering and absorption properties of the air bubbles. Here, we investigate the effect of oceanic air bubbles on the TOA reflectance as a function of N_0 and d for specific values of the refractive index of the coating film and the size distribution of the air bubbles.

Figure 5.2 shows the TOA reflectance deviation $[\Delta\rho^B_{TOA}(\lambda)]$ at 865 nm for the Coastal-90 and Urban-90 aerosol models with $\tau_{865} = 0.1$, and Fig. 5.3 shows the same quantity for the Coastal-90 model at 443 nm. From these plots in Figs. 5.2 and 5.3 we see that the TOA reflectance deviation increases with N_0 in both the NIR and the visible for weakly as well as strongly absorbing aerosols. The TOA reflectance deviation is about 1−3% at 865 nm, and 2−4% at 765 nm (the

plots for 765 nm are not shown here) for $N_0 = 10^7$ m^{-3}, and coating thickness $d = 0.05 - 0.2$ μm. This deviation will increase to 7–26% at 865 nm for $N_0 = 10^8$ m^{-3} when other conditions are unchanged. We also find that a strongly absorbing aerosol [Urban-90, see panel (b) in Fig. 5.2] will yield a larger TOA reflectance deviation than weakly absorbing aerosols. By comparing Figs. 5.2 and 5.3, we see that the deviation is larger in the visible than in the NIR. Figure 5.3 indicates that the deviation lies between 0.5% and 26% when N_0 is in the range $10^6 - 10^7$ m^{-3}, and roughly between 120% and 200% when $N_0 = 10^8$ m^{-3}. Similar conclusions are obtained for all aerosol models when other conditions are the same. We will therefore make extensive use of the Coastal-90 aerosol model for illustration purposes in the reminder of this paper.

The dependence of the TOA reflectance deviation on the coating thickness (d) is also illustrated in Figs. 5.2 and 5.3. For $\tau_{865} = 0.1$ the TOA reflectance deviation increases with increasing coating thickness, and similar results are obtained for other aerosol optical depths (not shown). For $\tau_{865} \leq 0.3$ there is a non-negligible error when the coating thickness is larger than 0.05 μm and N_0 is of the order of 10^7 m^{-3}. From these results we conclude that the TOA reflectance deviation caused by oceanic air bubbles is negligible when N_0 is much smaller than 10^7 m^{-3} regardless of the coating thickness. Thus, next we set $N_0 = 10^7$ m^{-3} and investigate how the TOA reflectance deviation depends on wavelength and the optical properties of aerosols.

5.4.2.2 Dependence of the TOA reflectance deviation on wavelength and aerosol optical properties

The retrieval of ocean color depends on an accurate atmospheric correction in the visible (i.e. removal of the contributions from the unknown aerosol and the known molecular components). Therefore, it is important to investigate how the

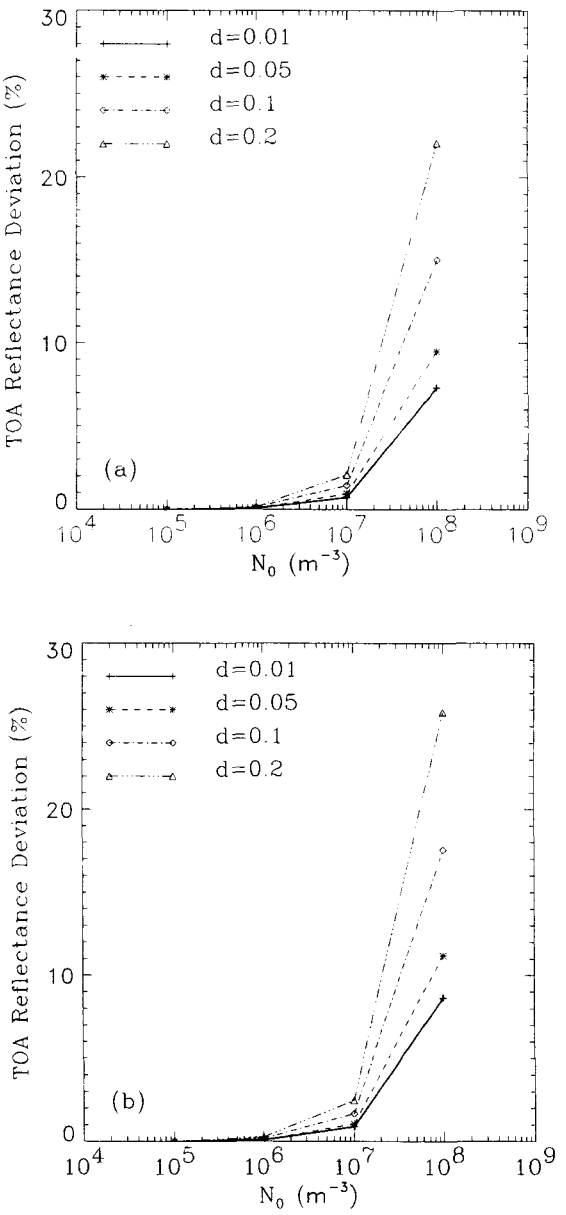

Figure 5.2 The TOA reflectance deviation at $\lambda = 865$ nm as a function of N_0 and d. The oceanic air bubbles are protein-coated with coating thickness $d = 0.01, 0.05, 0.1, 0.2$ μm. Aerosol optical depth $\tau_{865} = 0.1$. The solar zenith is 45°, the relative azimuth angle is 60°, and viewing zenith angle is 18°. (a) Coastal-90. (b) Urban-90.

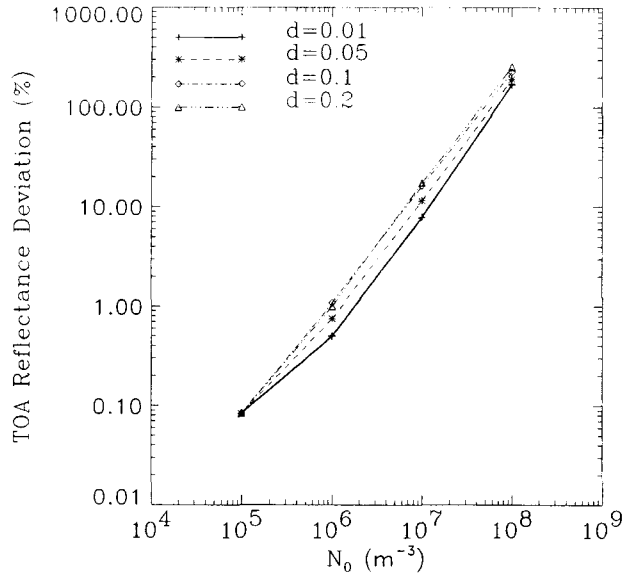

Figure 5.3 Same as Fig. 5.2(a) but for $\lambda = 443$ nm.

TOA reflectance deviation caused by oceanic air bubbles depends on wavelength as well as the optical properties of aerosols. Figure 5.4 shows the TOA reflectance deviation as a function of wavelength for the Coastal-90 model when $N_0 = 10^7$ m^{-3} and $\tau_{865} = 0.05$. Figure 5.5 shows the same plots as in Fig. 5.4 but for $\tau_{865} = 0.3$. By comparing Figs. 5.4 and 5.5, we see that the position of the maximum of the deviation in TOA reflectance changes with aerosol optical depth. The maximum deviation is 26% and occurs at 555 nm when $\tau_{865} = 0.05$. It is 18% at 510 nm when $\tau_{865} = 0.3$, and 14% at 490 nm when $\tau_{865} = 0.8$ (the plots for $\tau_{865} = 0.8$ are not shown). This explains why the error in the water-leaving reflectance due to oceanic air bubbles is larger at 555 nm than at 443 nm (see Fig. 5.6).

Figure 5.6 shows the dependence of the TOA reflectance deviation on aerosol optical depth at several wavelengths. When N_0 is of the order of 10^7 m^{-3} and the coating thickness $d > 0.05$ μm, the TOA reflectance deviation due to oceanic air

bubbles lies between 2% and 26% at blue and green wavelengths for the Coastal-90 aerosol model. Since the TOA water-leaving reflectance due to pigments in the ocean can be as low as only a few percent of the total satellite-measured reflectance, accurate assessment of the contribution from oceanic air bubbles to the TOA reflectance becomes important. Our simulations indicate that other aerosol models yield only slightly different results. In the NIR the deviations are smaller, but non-negligible, lying between about 1% and 4% at 765 and 865 nm when $\tau_{865} \leq 0.3$. In summary, these NIR and visible TOA reflectance deviations are sufficiently large that (i) the validity of the black pixel assumption needs to be carefully investigated; (ii) the error caused by oceanic air bubbles needs to be removed via an accurate atmospheric correction algorithm.

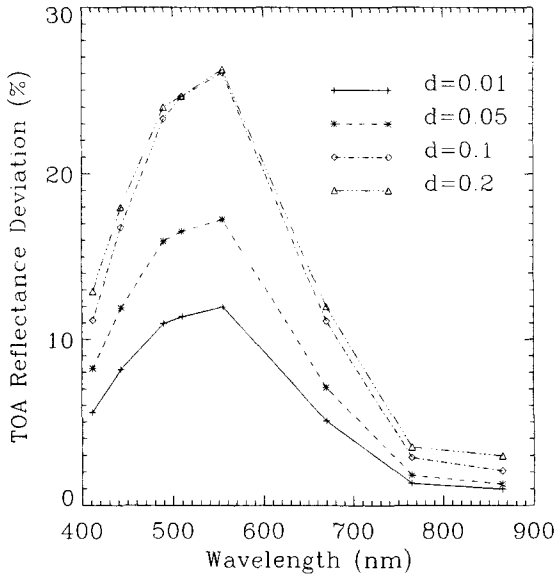

Figure 5.4 The TOA reflectance deviation as a function of wavelength for $\tau_{865} = 0.05$, and $N_0 = 10^7$ m^{-3}. The aerosol model Coastal-90 is used.

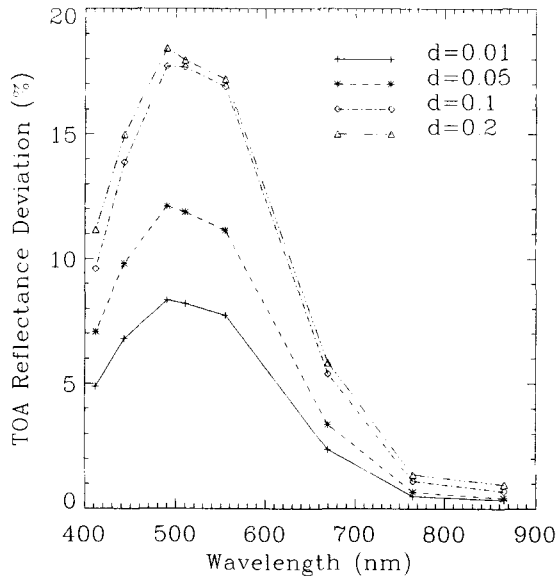

Figure 5.5 Same as Fig. 5.4 but for $\tau_{865} = 0.3$.

5.4.3 Error in the water-leaving reflectance retrieval due to the presence of oceanic air bubbles

The contribution of oceanic air bubbles to the TOA reflectance will, unless it is properly accounted for, lead to an error in the TOA reflectance as discussed in Section 5.3. This error leads to an error in the retrieved TOA water-leaving reflectance in the visible bands which consists of two parts as discussed in Section 5.3 [see Eq. (5.4)]. The first part is the direct contribution of the bubbles to the TOA reflectance in the visible. The second part stems from the inaccurately retrieved optical properties of the aerosols as part of the atmospheric correction process caused by the contribution of the oceanic air bubbles to the TOA reflectance in the NIR.

We now investigate the two parts of the error shown in Eq. (5.4) assuming

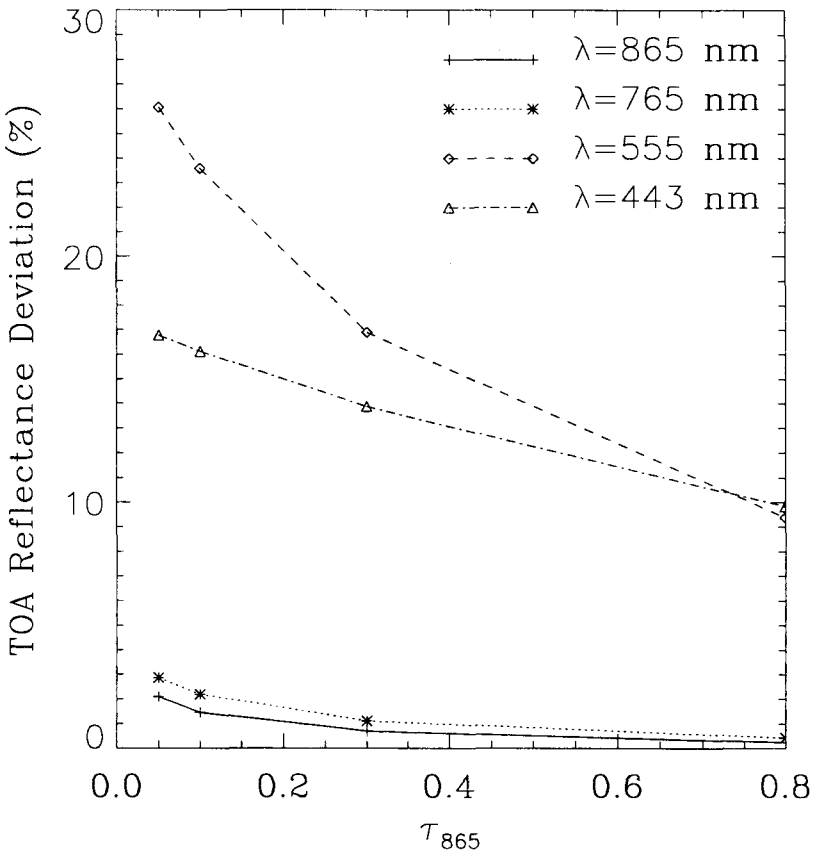

Figure 5.6 The TOA reflectance deviation at 865, 765, 555 and 443 nm as a function of the aerosol optical depth at 865 nm for protein-coated bubbles when $N_0 = 10^7$ m^{-3} and the coating thickness $d = 0.1\mu m$. The aerosol model Coastal-90 is used.

$N_0 = 10^7$ m^{-3}. For atmospheric correction purposes, we use 16 aerosol models. These are the same Coastal, Maritime, Tropospheric, and Urban aerosols that we introduced in Section 5.4, but with four different relative humidities RH = 50, 70, 90 and 99%, for each of these four models yielding a total of 16 models [9]. The TOA reflectances and $\epsilon_{ms}(\lambda, 865) = \rho_{ms}(\lambda)/\rho_{ms}(865)$ are precomputed and stored in lookup tables for these 16 candidate aerosol models with the aerosol optical depth at 865 nm lying in the range between 0.05 and 0.8. To simulate "measured" TOA reflectances, we use the Coastal-90 and Urban-90 as the "true" aerosol models, and we compute the corresponding "true" TOA reflectances in the presence of the oceanic air bubbles from the radiative transfer model for the coupled atmosphere-ocean system. By introducing the $\epsilon_{ms}(\lambda, 865)$, we compute the two errors shown in Eq. (5.4) via the following steps:

- We compute $\epsilon_{ms}(765, 865) = \rho_{ms}(765)/\rho_{ms}(865)$ from the simulated "true" TOA reflectances in the presence of oceanic air bubbles.

- We use these "true" values of $\epsilon_{ms}(765, 865)$ to retrieve an aerosol model and its corresponding optical depth among the suite of 16 candidate aerosol models for which $\epsilon_{ms}(765, 865)$ are stored in the lookup tables.

- We use the retrieved aerosol model and its corresponding optical depth determined in the previous step to compute $\rho^B_{tot}(\lambda_{vis})$, i.e. the TOA reflectance in the *presence* of oceanic air bubbles. Then, the first error on the right side of Eq. (5.4), i.e. $\Delta\rho_{tot}(\lambda_{vis})$, is simply the difference between $\rho^B_{tot}(\lambda_{vis})$ and $\rho_{tot}(\lambda_{vis})$, where $\rho_{tot}(\lambda_{vis})$ is the TOA reflectance obtained in the *absence* of bubbles for the *true* aerosol model and aerosol optical depth. Our simulations show that the chlorophyll concentration in the ocean does not significantly affect the magnitude of the error $\Delta\rho_{tot}(\lambda_{vis})$.

- The second error $\Delta\rho_{path}(\lambda_{vis})$ shown in Eq. (5.4) is computed as follows: (i) Using the *retrieved* aerosol model and optical depth, we determine $\epsilon_{ms}^{retr}(\lambda_{vis}, 865)$. (ii) $\Delta\epsilon_{ms}(\lambda_{vis}, 865)$ is the difference between $\epsilon_{ms}^{retr}(\lambda_{vis}, 865)$ and $\epsilon_{ms}^{true}(\lambda_{vis}, 865)$ determined for the true aerosol model. (iii) Similarly, $\Delta\rho_{ms}(865)$ is the difference between $\rho_{ms}^{retr}(865)$ and $\rho_{ms}^{true}(865)$. (iv) The error $\Delta\rho_{path}(\lambda_{vis})$ is obtained using Eq. (5.8). Note that the superscript "*retr*" stands for retrieved, and "*true*" for true. Also note that the error $\Delta\rho_{ms}(865)$ will in general consist of contributions due to oceanic air bubbles as well as chlorophyll pigments to the TOA reflectance in the NIR. However, as mentioned previously, for the low chlorophyll concentration used here (0.5 mg m^{-3}) the contribution due to chlorophyll pigments is negligible.

5.4.3.1 The error due to the direct contribution of the oceanic air bubbles

Figure 5.7 shows plots of $\Delta\rho_{TOA}^{B}(\lambda = 443\ nm)$ as defined in Eq. (5.9). These plots indicate that the error lies between 3% and 18% when the coating thickness is less than 0.2 μm. As we discussed above, this error is indirectly influenced by the inaccurately-retrieved aerosol model and optical depth as a result of the violation of the black pixel assumption in the NIR due to the oceanic air bubbles.

5.4.3.2 The error $\Delta\rho_{path}(\lambda_{vis})$ described in Eq. (5.8)

Figure 5.8 shows plots of $[\Delta\rho_{path}(\lambda_{vis})/\rho_{tot}(\lambda_{vis})] \times 100$ at $\lambda_{vis} = 443$ nm. We see that as a consequence of the violation of the black pixel assumption in the NIR due to oceanic air bubbles, the error in the retrieval of water-leaving reflectance lies between -9% and $+1\%$ for non- or weakly-absorbing aerosols [see Fig. 5.8 (a)]. This error lies between -12% and $+4\%$ for strongly absorbing aerosols [see Fig. 5.8 (b)]. Note that this error does not always increase with increasing coating

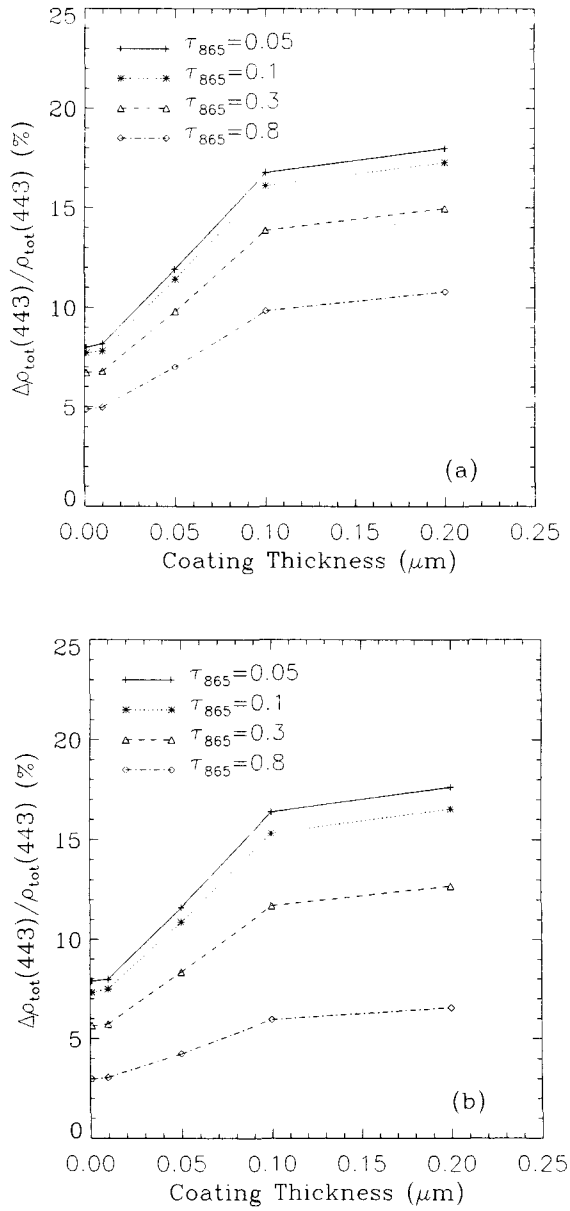

Figure 5.7 Plots of $\Delta\rho_{tot}(\lambda_{443})/\rho_{tot}(\lambda_{443})$ as a function of the coating thickness of protein-coated bubbles. τ_{865} is in the range between 0.05 and 0.8. $N_0 = 10^7$ m^{-3}. (a) Coastal-90. (b) Urban-90.

thickness and decreasing aerosol optical depth. To understand the results shown in Fig. 5.8, we may rewrite Eq. (5.8) in the following form

$$\Delta\rho_{path}(\lambda_{vis}) \approx \rho_{ms}(865)\epsilon_{ms}(\lambda_{vis},865)\left[\frac{\Delta\epsilon_{ms}(\lambda_{vis},865)}{\epsilon_{ms}(\lambda_{vis},865)} + \frac{\Delta\rho_{ms}(865)}{\rho_{ms}(865)}\right].$$

We know that $\frac{\Delta\rho_{ms}(865)}{\rho_{ms}(865)}$, caused by chlorophyll pigments and oceanic air bubbles, is less than a few percent for case 1 waters and is always positive[?]. What about $\frac{\Delta\epsilon_{ms}(\lambda_{vis},865)}{\epsilon_{ms}(\lambda_{vis},865)}$? To answer this question, we introduce Fig. 5.9. In the operational SeaWiFS atmospheric correction algorithm [69, 70], the retrieval of the aerosol model as well as the aerosol optical depth in the NIR is based on $\epsilon_{ms}(765,865)$. From Fig. 5.9 we see that if No. 10 is the true aerosol model, but No. 9 is mistakenly selected in the atmospheric correction process, then $\Delta\epsilon_{ms}(443,865)$ will be positive. On the other hand, if No. 10 is the true aerosol model, but No. 11 is mistakenly selected in the atmospheric correction process, then $\Delta\epsilon_{ms}(443,865)$ will be negative. Therefore, we can conclude that $\frac{\Delta\epsilon_{ms}(\lambda_{vis},865)}{\epsilon_{ms}(\lambda_{vis},865)}$ may be positive or negative. From Fig. 5.9 we can also see that the absolute values of $\frac{\Delta\epsilon_{ms}(\lambda_{vis},865)}{\epsilon_{ms}(\lambda_{vis},865)}$ lie between a few percent and a few-ten percent (or even larger), i.e. $\left|\frac{\Delta\epsilon_{ms}(\lambda_{vis},865)}{\epsilon_{ms}(\lambda_{vis},865)}\right|$ is usually larger or much larger than $\frac{\Delta\rho_{ms}(865)}{\rho_{ms}(865)}$. Thus, we may conclude that the "random" error shown in Figs. 5.8 (a) and (b) is dominated by the error $\frac{\Delta\epsilon_{ms}(\lambda_{vis},865)}{\epsilon_{ms}(\lambda_{vis},865)}$, and it might be positive or negative, depending on which incorrect aerosol model is retrieved as a consequence of the violation of the black pixel assumption due to the presence of oceanic air bubbles, as we discussed in Section 5.3. Obviously, the "random" nature of the error shown in Figs. 5.8 (a) and (b) will make atmospheric correction complicated and difficult when this error due to the presence of oceanic air bubbles cannot be ignored.

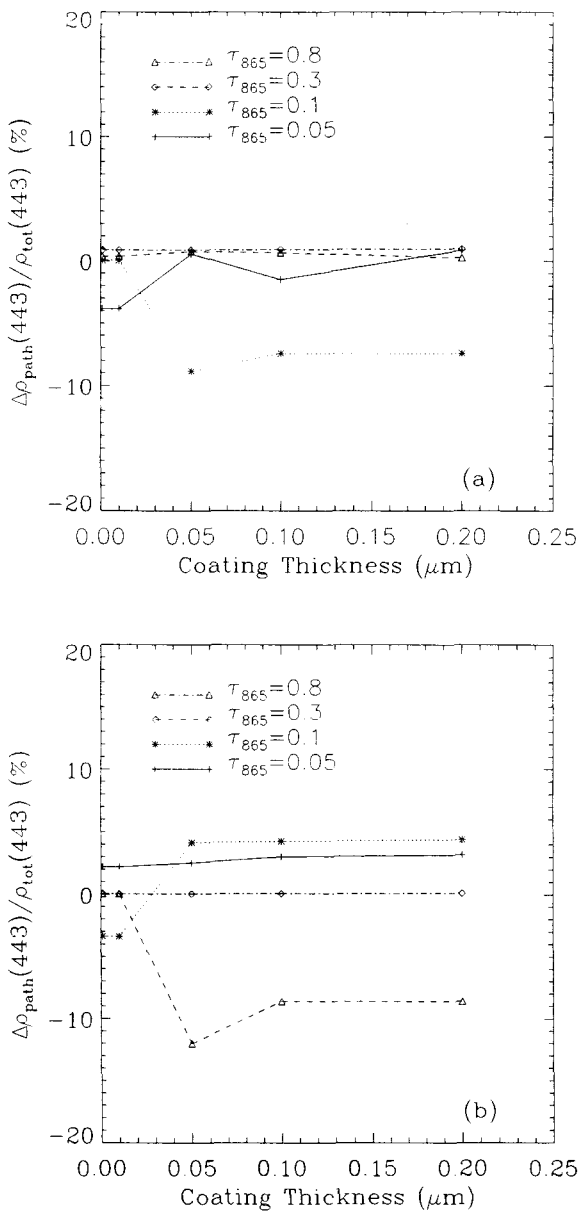

Figure 5.8 Same as the plots in Fig. 5.7 but for $\Delta\rho_{path}(\lambda_{443})/\rho_{tot}(\lambda_{443})$.

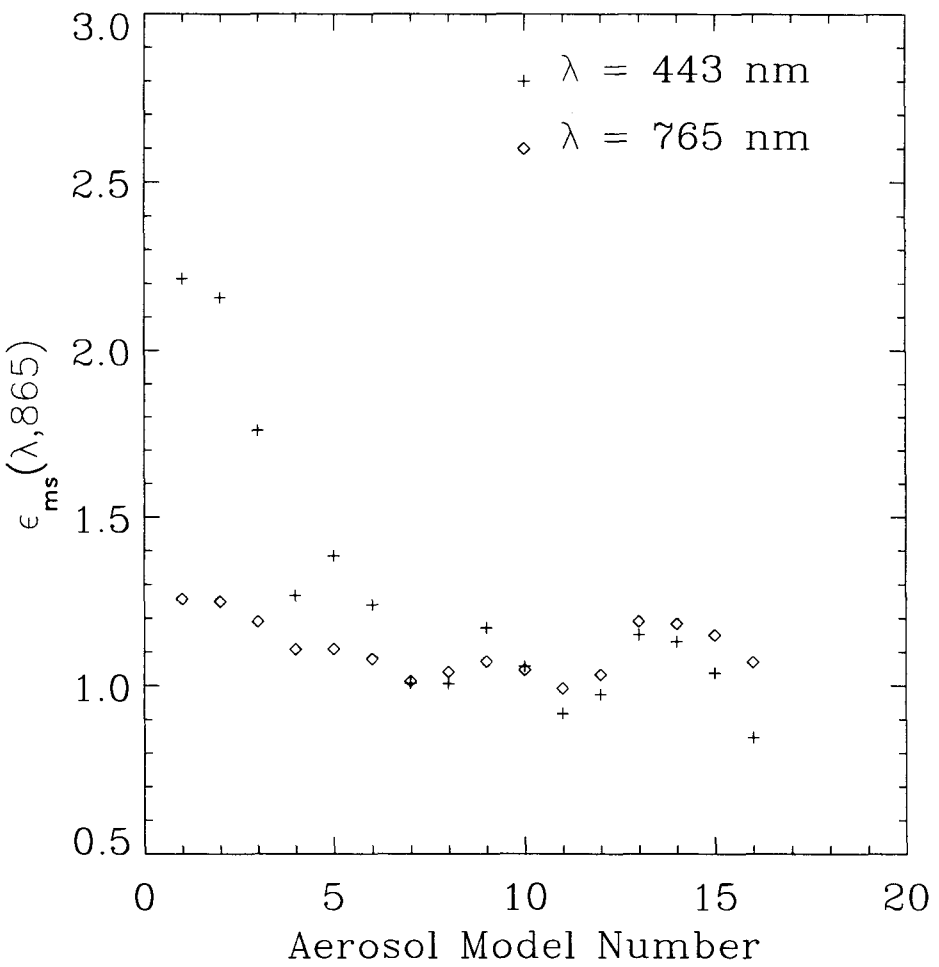

Figure 5.9 $\epsilon_{ms}(\lambda, 865)$ values at 443 and 765 nm for 16 aerosol models: (i) No. 1-4: Coastal-50, 70, 90, 99; (ii) No. 5-8: Maritime-50, 70, 90, 99; (iii) No. 9-13: Tropospheric-50, 70, 90, 99; and (iv) No. 13-16: Urban-50, 70, 90, 99. $\tau_{865} = 0.10$.

5.4.3.3 Error sensitivity to parameter D_b

As we discussed in Section 5.2, oceanic air bubbles are usually assumed to be distributed uniformly within the top layer of the ocean. So far, we have used $D_b = 5$ m for the thickness of this bubble layer. To investigate the sensitivity of the error to the choice of the parameter D_b, we show in Fig. 5.10 the TOA reflectance deviation due to the presence of oceanic air bubbles for different values of D_b. These plots indicate that when D_b increases, the error in the water-leaving reflectance due to the presence of bubbles increases. At 443 nm, the error for $D_b = 10$ m is twice as large as for $D_b = 5$ m. These results indicate that more field measurements are needed to establish the depth-dependence of the oceanic air bubble concentration.

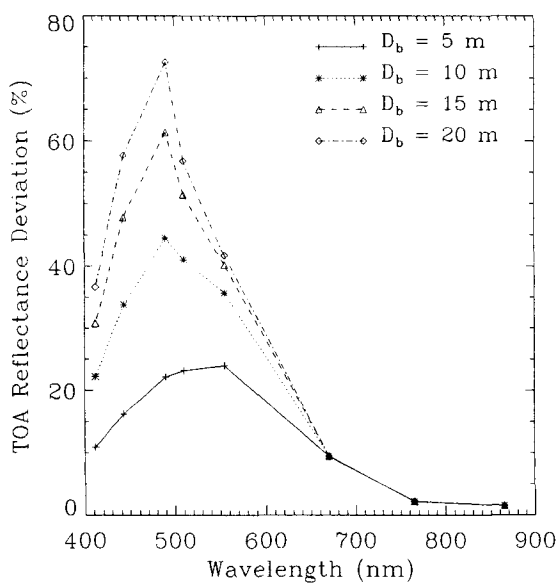

Figure 5.10 The TOA reflectance deviation for different thicknesses D_b of the top layer of the ocean water in which the bubbles are assumed to be distributed uniformly. The Maritime-90 aerosol model is used with $\tau_{865} = 0.1$. The coating thickness is $d = 0.1$ μm.

5.5 Conclusions

A comprehensive radiative transfer model for the coupled atmosphere-ocean system is used to investigate the effect of oceanic air bubbles on the retrieval of the water-leaving reflectance at visible wavelengths. This effect is evaluated through (i) the TOA reflectance deviation at both NIR and visible wavelengths, and (ii) the error in the retrieval of the TOA water-leaving reflectance in the visible. The magnitude of the error incurred by ignoring oceanic air bubbles in the atmospheric correction of ocean color imagery depends on (i) the oceanic air bubble concentration, (ii) the coating thickness and refractive index of the organic film surrounding the bubbles, (iii) the aerosol optical properties including scattering and absorption, aerosol optical depth, and phase function, and (iv) wavelength.

The TOA reflectance deviation due to the contribution of oceanic air bubbles increases with increasing bubble concentration and coating thickness, and with decreasing aerosol optical depth. When the aerosol optical depth at 865 nm is less than 0.3, the bubble concentration is 10^7 m^{-3}, and the coating thickness is greater than 0.05 μm, this deviation is 1$-$4% in the NIR, and 7$-$26% in the visible. Thus, the NIR deviation is sufficiently large that the black pixel assumption becomes questionable, and the deviation in the visible region will also lead to an error in ocean color retrieval.

The error in the retrieval of the water-leaving reflectance in the visible due to the presence of oceanic air bubbles includes two parts: (i) extra upward radiance in the visible resulting from oceanic air bubbles, mistakenly attributed to chlorophyll pigments; and (ii) erroneous atmospheric correction in the visible due to incorrect identification of aerosol model and incorrect assignment of optical depth as a result of the violation of the black pixel assumption in the NIR. Simulations indicate that at 443 nm the first part of the error lies between 3% and 18% whereas the second

part lies between -12% and $+4\%$.

Thus, the effect of oceanic air bubbles on the retrieval of the water-leaving radiance should be considered in algorithms aimed at atmospheric correction of ocean color imagery. Otherwise, wrong atmospheric correction and erroneous inference of water-leaving radiance and marine pigment concentration would occur. Our knowledge of oceanic air bubbles is still incomplete, and uncertainties remain concerning the size distribution and its change with depth in the ocean as well as the composition and thickness of the film coating. Nevertheless, the results presented in this study have provided a quantitative assessment of the potential impact on atmospheric correction of ocean color imagery. A remaining challenge in the remote sensing area is to establish adequate procedures for proper identification of oceanic air bubbles from the measured radiances at the TOA, and subsequent quantification and removal of their contribution to the water-leaving radiance.

Chapter 6

Pitfalls in atmospheric correction of ocean color imagery: How should aerosol optical properties be computed?

6.1 Introduction

The wavelength-dependence of the water-leaving radiance just above the ocean surface is usually referred to as the ocean color. It is the result of scattering and absorption by chlorophyll pigments as well as dissolved and particulate matter in the subsurface ocean waters. Thus, the ocean color provides information about the concentrations of phytoplankton, dissolved organic matter, and particles in the water column. This implies that, at least in principle, these concentrations can be retrieved from measurements of the ocean color from space, on regional as well as global scales. However, the water-leaving radiance due to scattering and absorption in the ocean can be as low as a few percent of the TOA radiance [21].

Consequently, it becomes very important to quantify and accurately remove the contribution from atmospheric molecules and aerosols to the TOA radiances. This removal is commonly referred to as "atmospheric correction".

SeaWiFS was designed to measure the TOA radiances in 8 bands between 412 and 865 nm. An algorithm for atmospheric correction of the SeaWiFS imagery obtained over case 1 waters was developed by Gordon and Wang [69, 70]. This algorithm utilizes 12 candidate aerosol models for non-absorbing or weakly absorbing aerosols in the atmospheric correction process. To study the atmospheric correction for strongly absorbing aerosols, four additional aerosols models have been considered [70, 11, 13]. The optical properties of aerosols vary in time and space. For atmospheric correction purposes it is important to select candidate aerosol models that span the range of conditions one expects to encounter over the region under consideration. Schwindling *et al.* measured direct atmospheric transmittance and sky radiance in La Jolla, California, in an attempt to verify if the aerosol models selected by Gordon and Wang for SeaWiFS are adequate for ocean color remote sensing from space [100]. They found that these aerosol models allow one to fit, within measurement inaccuracies, the derived values of the Angstrom coefficient and the 'pseudo' phase function (the product of the single scattering albedo and the phase function). However, additional measurements taken under different atmospheric conditions would be required to make a more general assessment of the suitability of these candidate aerosol models for atmospheric correction purposes.

These 16 candidate aerosol models consist of several types of particles, each having its own characteristic chemical composition, size distribution and hygroscopicity [9]. The following questions then arise: How do we compute the optical properties of such a multi-component mixture of dry aerosol particles? And can we predict how these optical properties change with an increase in the humidity of

the air in which the particles are suspended? The changes in the optical properties depend on how the particles grow and mix when they are exposed to humidity. Mixing is usually treated superficially in radiative transfer models due to lack of observational data, but the mixing mechanism adopted affects the absorption by the aerosols [101, 102]. As the relative humidity (RH) increases, water vapor condenses out of the atmosphere onto the suspended aerosol particles. This condensed water increases the size of an aerosol particle and changes its composition (and hence its refractive index). As a result its optical properties are correspondingly modified [9, 103, 104].

The aerosol models used for atmospheric correction in the SeaWiFS operational algorithm are based on those constructed by Shettle and Fenn [9]. These models were based on the aerosol data available at that time, and they were designed to cover a wide range of atmospheric conditions. In order to save computational resources (computers were much less powerful in the 1970's than today!), Shettle and Fenn decided to combine the different aerosol species into an effective single-component model by averaging the refractive indices of the multi-component aerosol mixture. This approach, which we shall refer to as the single-component (SC) approach below, seemed to be a reasonable choice at the time. In view of the sparsity of observational data this SC approach has been used by the atmospheric community for a variety of purposes. To account for the change in optical properties with changing relative humidity Shettle and Fenn used the SC approach to compute and tabulate the change in particle size and refractive index as a function of relative humidity. These tables provided a convenient set of optical properties which have been used extensively for a variety of purposes. In particular, these tables have been used in conjunction with Mie computations to obtain aerosol optical properties which are then used as a basis for atmospheric correction of ocean color imagery [69, 70, 11, 13, 22, 23].

A more realistic approach would be to treat each aerosol component separately, and compute its change in size and refractive index with relative humidity. The optical properties of a multi-component mixture would then be obtained by first computing the optical properties of each component, and then obtain the optical properties of the mixture as the concentration-weighted-average of the optical properties of each aerosol component [24]. For convenience we refer to this procedure as the multi-component (MC) approach below. d'Almeida *et al.* [25] also discussed the MC approach: each component is characterized by a specific log-normal distribution and a wavelength-dependent refractive index, and then these two quantities enable the computation of the optical properties of the components, and finally the addition of the component properties, weighted by their respective mixing ratios, yields the optical properties of the aerosol type in question [25].

Remote sensing of ocean color from space is a very difficult undertaking due to the small contribution of the water-leaving radiance (transmitted through the atmosphere) to the total TOA radiance. A few percent error in the TOA reflectance in the near-infrared (NIR) bands caused by the violation of the NIR black pixel assumption will lead to a non-negligible error in the retrieval of ocean color [15, 16]. Therefore, accurate computation of the optical properties of the candidate aerosol models adopted for atmospheric correction purposes becomes a matter of considerable importance. In this paper, we use an accurate numerical scheme to compute the change in size and refractive index of individual aerosol components with increasing relative humidity, as well as an accurate Mie computational code to compute the optical properties of a multi-component aerosol mixture [24]. A comprehensive radiative transfer code [61] properly modified to apply to the coupled atmosphere-ocean system [63, 64] is employed to compute the TOA radiance in the 8 SeaWiFS bands, and to assess the error incurred by using optical properties generated by the SC approach as compared to the more

realistic MC approach.

6.2 Comparisons between aerosol optical properties computed using the SC and the MC approachs

The 16 aerosol models employed as candidate models in the SeaWiFS algorithm for atmospheric correction of ocean color imagery, include the Coastal, Maritime, Tropospheric, and Urban models introduced by Shettle and Fenn [9]. Each of these are used with relative humidities (RH) of 50, 70, 90 and 99%, respectively, which yield a total of 16 different models. Except for the Tropospheric aerosol models, these models consist of two log-normal size distributions (LND) as follows [9]:

$$n(r) = \frac{dN(r)}{dr} = \sum_{i=1}^{2} \left[\frac{N_i}{\ln(10) r \sigma_i \sqrt{2\pi}} \right] exp \left[- \frac{(\log r - \log r_i)^2}{2\sigma^2} \right], \qquad (6.1)$$

where N(r) is the cumulative number density of particles with radius r, σ is the standard deviation, and N_i is the number density of particles with the mode radius r_i. r_i and σ depend upon the aerosol model and RH [9]. This form of distribution function represents the multi-modal nature of the atmospheric aerosols that has been discussed in various studies [105, 106, 107, 108, 109]. Harris and McCormick have suggested using the sum of as many as four log-normal distributions [110] and Davies used the sum of as many as seven log-normal distributions to fit a measured aerosol size distribution [111]. However, Whitby and Cantrell have shown that two modes are generally adequate to characterize the gross features of most aerosol distributions [112].

6.2.1 Physical difference between the SC and the MC approachs

It is well known that the aerosol size and refractive index will change in a moist environment because water in the air condenses onto the aerosol. The growth in particle size due to the condensation of water vapor is [103]

$$r(a_w) = r_0\left[1 + \rho\frac{m_w(a_w)}{m_0}\right]^{1/3}, \tag{6.2}$$

where the water activity of a soluble aerosol at radius r [μm] can be expressed as

$$a_w = RH\ exp\left[\frac{-2\sigma V_w}{R_w\,T}\cdot\frac{1}{r(a_w)}\right]. \tag{6.3}$$

Here r_0 is the dry particle radius, ρ the particle density relative to that of water, $m_w(a_w)$ the mass of condensed water, m_0 the dry particle mass, RH the relative humidity, σ the surface tension on the wet surface, V_w the specific volume of water, R_w the gas constant for water vapor, and T the absolute temperature [K].

The refractive index for the wet aerosol particle modified by the increased size is simply the volume-weighted average of the refractive indices of the dry aerosol substance (n_0) and the water (n_w) as follows

$$n = n_w + (n_0 - n_w)\left[\frac{r_0}{r(a_w)}\right]^3. \tag{6.4}$$

From these formulae, we note that: (i) The magnitude of the particle growth and the change of refractive index with increasing relative humidity depends on the size r_0 of the dry aerosol. The aerosol size in each of the 16 aerosol models spans a large range depending on the aerosol component. For example, the typical size range of dry soot particles lies between 0.005 and 20.0 μm [25]. This implies that the rate of change of size and refractive index due to increased RH will depend on aerosol size, i.e., it is not a constant across the aerosol size range.

(ii) The magnitude of the particle growth and the change of refractive index with increasing relative humidity depends on the aerosol type because the water uptake (the ratio $m_w(a_w)/m_0$ in Eq. (6.2)) depends on aerosol type [103, 113, 114]. The aerosol models introduced by Shettle and Fenn [9] consist of five groups: water soluble (e.g., ammonium, organic compounds, etc.), dust-like (e.g., clay, quartz, etc.), soot (e.g., graphite, elemental carbon, etc.), sea salt (e.g., sodium, potassium chloride, etc.), and liquid water. Since the physical size of the aerosol may grow either because it is soluble or it consists of an insoluble core with a soluble material coating, the rate of growth for a specific particle size differ from one aerosol component to another.

Both the SC and MC approaches consider the particle growth and the change in refractive index of the aerosol due to increased relative humidity to be as described by the Eqs. (6.2)-(6.4). However, as mentioned above the SC approach is based upon an effective refractive index obtained as an average over the multi-component aerosol population. This homogeneous mixing results in a single-component aerosol population that is assumed to adequately represent the actual multi-component mixture. This single-component aerosol population with an effective refractive index is then modified by the relative humidity according to Eqs. (6.2)-(6.4). The resulting particle growth and change in refractive index are provided in Tables 4 and 5 of Shettle and Fenn [9]. The SC approach ignores the fact that different aerosol components grow and thereby change their refractive indices at different rates as the humidity increases. In contrast to the SC approach, the MC approach allows each aerosol component to grow and change refractive index independently with relative humidity according to Eqs. (6.2)-(6.4). This heterogeneous mixing allows the size and refractive index of each component to be modified by the changing RH at all different aerosol sizes within the size distribution, and the optical properties of each aerosol component is computed separately for each modified

particle size consistent with its modified refractive index [24]. Thus, the MC approach describes the particle growth and its change in refractive index caused by the increased relative humidity for each particular size of the aerosol distribution, and each component in a physically reasonable manner.

The size and refractive index of the aerosol affect the asymmetry factor (g) of the aerosol population and the imaginary part of the refractive index affects the single scattering albedo (SSALB) of aerosol population. From this discussion it is easy to understand that for a specific aerosol size the SC approach will lead to a distribution of refractive indices that is different from that produced by the MC approach. Conversely, for a specific refractive index the SC approach will lead to a size distribution different from that produced by the MC approach. As shown in section 6.2, these differences in aerosol size and refractive index distributions between the SC and the MC approaches will cause significant discrepancies between the optical properties produced by the SC and the MC approach as we see below (see section 6.2.2).

6.2.2 Comparisons between aerosol optical properties computed by the SC and MC approaches

The difference between the SC and MC approaches in the way the particles are allowed to grow and change their refractive indices with increasing humidity, leads to significant differences in the resulting optical properties for a collection of aerosols consisting of more than one type of particles. As explained above, "type" here refers to the refractive index of the particle (i. e. its chemical composition) and its solubility or water uptake capacity (i.e. its hygroscopicity). Thus, it is no surprise that these two approaches lead to different bulk optical properties for the mixture of particles as a whole, such as the angular scattering pattern or phase function,

and the wavelength-dependence of the optical depth. This is a necessity because the bulk optical properties are obtained by averaging over optical properties of individual particles as determined by their sizes and refractive indices. Furthermore if any of the particle types in the mixture is absorbing, so that the imaginary part of its refractive index is non-zero, then the SC and MC approaches will result in significant differences in the single scattering albedo (SSALB = the ratio of scattering to extinction coefficient) even for a dry mixture of particles, and a different evolution of the SSALB as the particles grow with increasing humidity. To quantify these effects we show results for the single scattering albedo SSALB, the asymmetry factor g (the first moment of the phase function), and the wavelength-dependence of the optical depth. For illustration purposes, we show results only for the Tropospheric and Urban aerosols models at wavelengths of 443 and 865 nm generated with the SC and MC approaches. Similar results (not shown here) are obtained for the other candidate aerosol models. The Tropospheric aerosol model consists of weakly absorbing particles with 70% water soluble substance and 30% dust-like substance. The Urban aerosol model consists of a mixture of weakly absorbing as well as absorbing particles with 56% water soluble substance, 24% dust-like substance, and 20% soot-like substance.

Figure 6.1 shows comparisons of the single scattering albedo (SSALB), the asymmetry factor (g), and the spectral dependence of the optical depth for the Tropospheric aerosol model computed with the two different approaches. As shown in Figs. 6.1 (a) and (b), the SSALB depends weakly upon whether the SC or MC approach is adopted. This is understandable in view of the weak absorption. However, the MC approach leads to a larger asymmetry factor with increasing humidity than the SC approach as illustrated in Figs. 6.1 (c) and (d). This is primarily a consequence of larger particles being produced by the MC approach than by the SC approach as the particles grow with increasing humidity, but the

different rates of water uptake also affect the refractive index of the particles as shown in Eq. (6.4). Thus, this difference in G may be partly due to a smaller rate of growth with increasing humidity produced by the SC approach as a result of its use of an effective refractive index for the entire population. We also note that the difference in G as a result of increased humidity between the SC and MC approaches is more pronounced in the NIR spectral region (865 nm) than in the blue region (443 nm).

The SC and MC approaches lead to a spectral dependence of the aerosol optical depth τ that is markedly different when the humidity is high ($RH \geq 90\%$) as shown in Figs. 6.1 (e) and (f). Since the dependency of the asymmetry factor upon wavelength is stronger in the SC approach than in the MC approach, the spectral dependence of τ obtained with the SC approach is much stronger than that obtained with the MC approach because the spectral dependence of the SSALB is similar in the two approaches.

Figure 6.2 shows results similar to those presented in Fig. 6.1, but for the Urban aerosol model containing a mixture of weakly-absorbing as well as absorbing aerosols as described above. The results are similar to those obtained in Fig. 6.1 pertaining to weakly-absorbing aerosols, except for the following two points: (i) as shown in Figs. 6.2 (a) and (b) the MC approach yields a much higher SSALB than the SC approach except for very high relative humidities ($RH \geq 90\%$), (ii) as shown in Figs. 6.2 (c) and (d) the MC approach yields a smaller g than the SC approach when RH is small (e.g. when $RH \leq 90\%$ at 443 nm and when $RH \leq 80\%$ at 865 nm).

The Urban aerosol models contain strongly absorbing particles. If the absorbing particles are water soluble or contain a water soluble coating, then, as the humidity increases, the absolute value of the imaginary part of the refractive index of the aerosol is reduced compared to its original value [see Eq. (6.4)]. When we use the

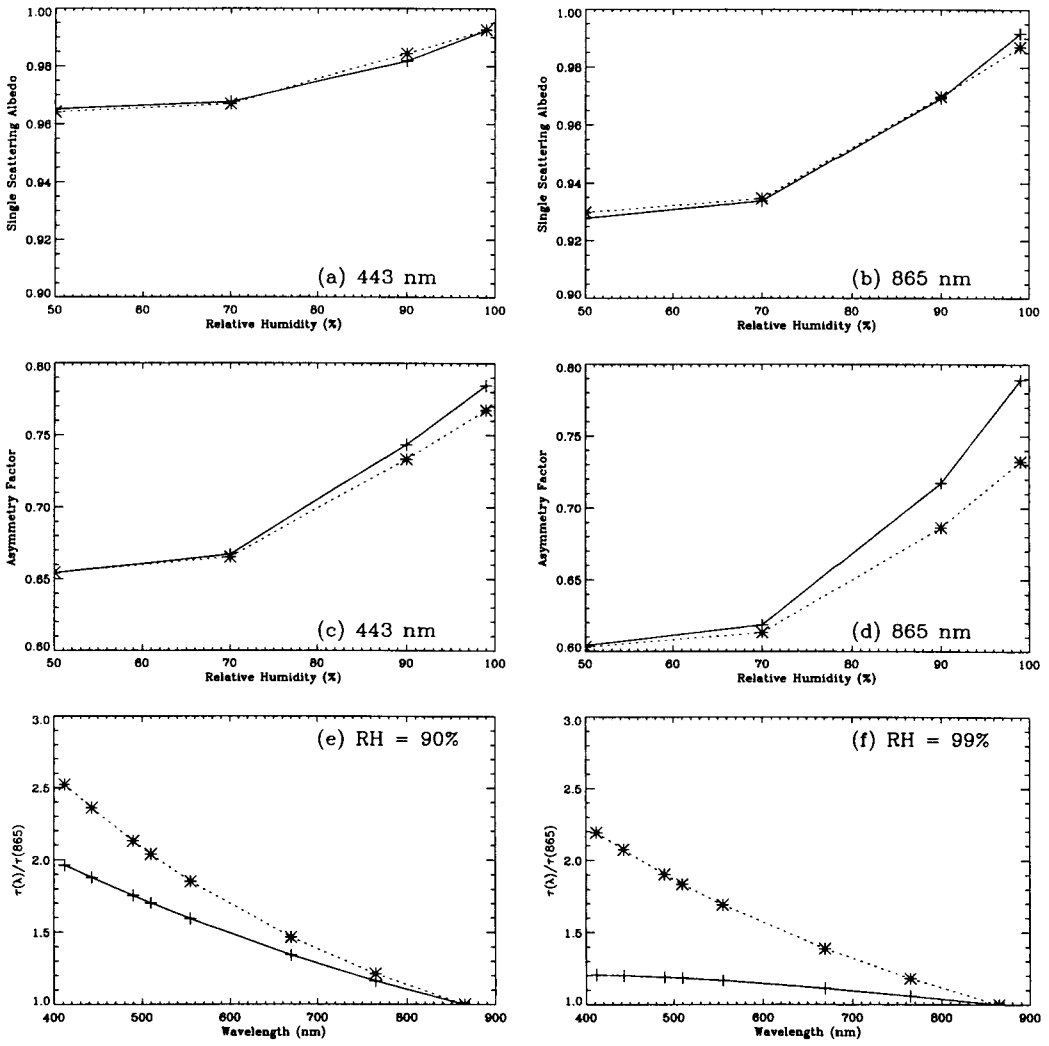

Figure 6.1 Comparison of single scattering albedo SSALB, asymmetry factor g, and optical depth $\tau(\lambda)$ for the Tropospheric aerosol model computed using the MC approach (solid curves) and SC approach (dotted curves) at 443 nm and 865 nm. (a) SSALB at 443 nm, (b) SSALB at 865 nm, (c) g at 443 nm, (d) g at 865 nm, (e) $\tau(\lambda)/\tau(865)$ for $RH = 90\%$, and (f) $\tau(\lambda)/\tau(865)$ for $RH = 99\%$.

MC approach, this effect is stronger than when we use the SC approach. Thus, a larger SSALB is obtained with the MC approach when the RH is smaller than about 95%. The asymmetry factor is primarily determined by the particle size, but also to some extent by the real part of the refractive index. Thus, the larger G-values obtained by the SC approach for the relatively dry Urban aerosol ($RH \sim$ 50%) may be due to the effective refractive index used in this approach. However, as the particles grow with increased humidity, the particle size becomes a more important factor in determining the asymmetry factor. A more comprehensive investigation, beyond the scope of the present study, would be required to explain the detailed behavior of the g-values displayed in Figs. 6.2 (c) and (d).

6.3 Implications for atmospheric correction of ocean color imagery

The accuracy of ocean color retrievals depends critically on our ability to perform accurate removal of the aerosol contribution to the measured TOA radiance, i.e., on accurate atmospheric correction. Errors in the optical properties of the aerosols will directly affect the accuracy of our atmospheric correction. To explore this issue we compare TOA radiances resulting from the SC approach with those obtained from the more realistic MC approach. The following results were derived from a radiative transfer code applicable to the coupled atmosphere-ocean system. However, for simplicity we ignored the scattering by particles in the ocean, in order to focus on the aerosol contribution. However, scattering by molecules in the air and in the ocean is included. Thus, in the NIR spectral region the ocean will be "black". For convenience, we define the reflectance as the TOA hemispherical irrradiance divided by the extraterrestrial solar irradiance, i.e. $\rho = \pi \mathrm{I}/\mathrm{F_0}\cos\theta_0$, where I is

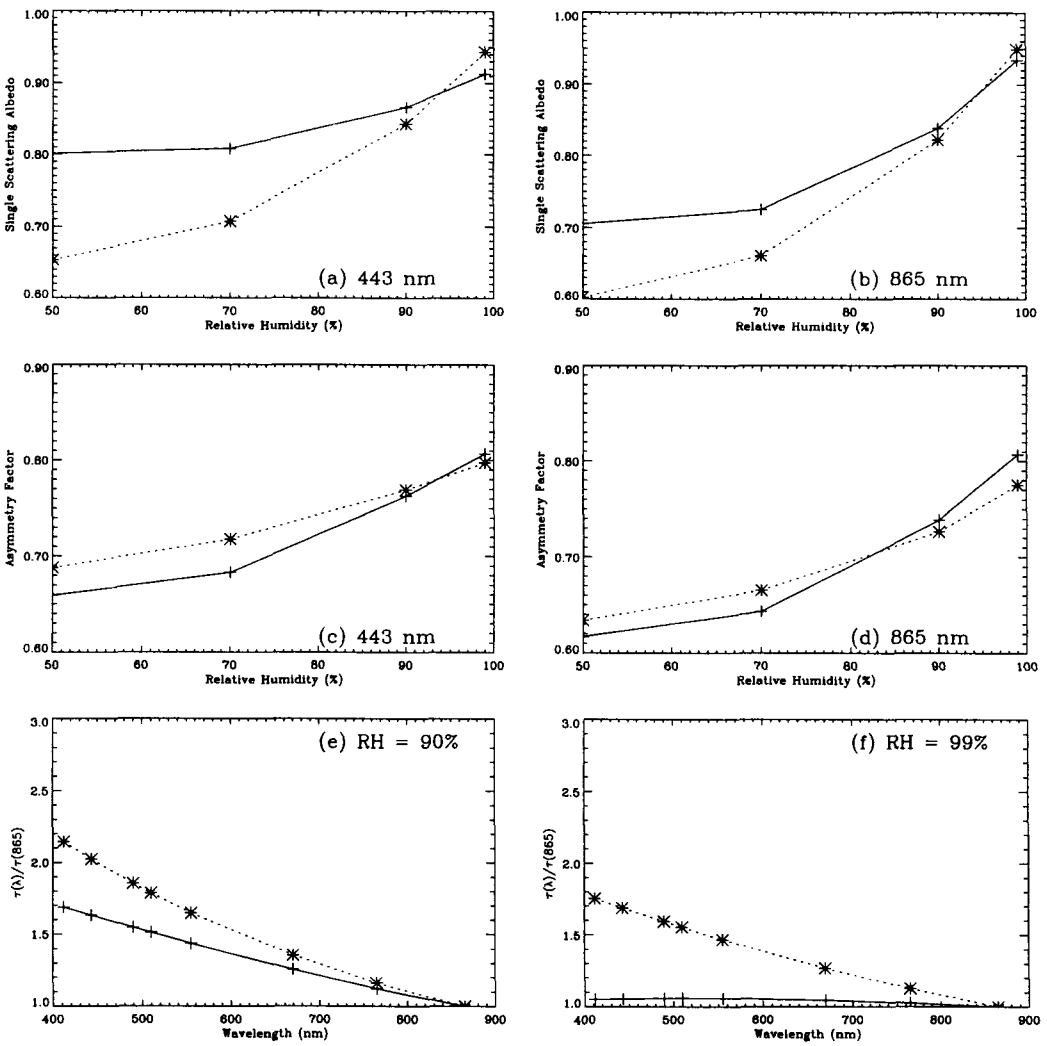

Figure 6.2 Similar to Fig. 6.1 but for Urban aerosols.

the TOA radiance, F_0 is the extraterrestrial solar irradiance (normal to the solar beam), and θ_0 is the solar zenith angle. In the following figures we display results for polar angle $\theta_0 = 35°$ and azimuthal angle $\phi = 60°$ relative to the solar azimuth.

6.3.1 TOA reflectance deviation

To compare TOA reflectances resulting from the SC approach with those obtained from the more realistic MC approach, we introduce the TOA reflectance deviation defined as

$$\rho_{dev} = \left[\frac{\rho'_{path}(\lambda) - \rho_{path}(\lambda)}{\rho_{path}(\lambda)}\right] \times 100, \tag{6.5}$$

where $\rho'_{path}(\lambda)$ denotes the TOA reflectance obtained with the SC approach, and $\rho_{path}(\lambda)$ denotes the TOA reflectance obtained with the MC method.

The vertical distribution of aerosols varies in time and space. In the SeaWiFS algorithm a two-layer model is assumed in the atmosphere: the aerosols occupy the lower layer, and all molecular scattering is confined to the upper layer [70]. This distribution of aerosols is similar to that typically found over the oceans when the aerosols are locally generated, i.e., most of the aerosols are confined to the marine boundary layer [115]. For demonstration purposes, in the following computations, we let the aerosols be distributed homogeneously between the surface and 4 km.

Figures 6.3 and 6.4 show the TOA reflectance deviation at four wavelengths for the Tropospheric and Urban aerosol models, respectively. For the Tropospheric aerosol model, Fig. 6.3 shows that the smaller asymmetry factor and the larger optical depth obtained with the SC approach lead to an overestimation of the TOA reflectance by as much as +32%. This implies that the aerosol contribution to the TOA radiance will be overestimated by the same amount, and hence lead to a significant error in the atmospheric correction. Similar conclusions are obtained for other aerosol models containing weakly absorbing particles, such as the Coastal

and Maritime aerosol models used for atmospheric correction purposes.

For the Urban aerosol model, Fig. 6.4 shows that the TOA reflectance deviation changes from being negative (-32% at $RH = 50\%$) to becoming positive ($+20\%$ at $RH = 99\%$) when the humidity increases. This finding is consistent with the difference in the optical properties of the aerosols resulting from the SC approach as compared to the MC approach. This implies that the SC approach underestimates the TOA reflectance for low relative humidities ($RH < 90\%$) and overestimates it when $RH > 90\%$.

Clearly, both for weakly absorbing and strongly absorbing aerosols the SC approach leads to considerable errors in the TOA reflectance. In fact, these errors can be as large as or even larger than the contribution by the ocean to the TOA radiance, which is typically a few percent of the total TOA reflectance. Thus, these errors are significant and must be corrected.

6.3.2 $\epsilon_{ms}(\lambda, 865)$ and $\gamma(\lambda)$

The SeaWiFS algorithm for atmospheric correction over case 1 waters employs various ratios, involving the aerosol and the molecular contribution to the TOA radiance. These ratios are used to select an aerosol model and a corresponding NIR optical depth. Based on the model selected the optical depth is then extrapolated from the NIR into the visible, where it is used to quantify the atmospheric contribution to the TOA radiance, so that it can be subtracted from the total. The current operational SeaWiFS algorithm indirectly employs the ratio [70]

$$\epsilon_{ms}(\lambda, 865) = \rho_{ms}(\lambda)/\ \rho_{ms}(865),$$

where $\rho_{ms}(\lambda) = \rho_{path}(\lambda) - \rho_r(\lambda)$ and $\rho_{path}(\lambda)$ is the total atmospheric contribution and $\rho_r(\lambda)$ the atmospheric molecular contribution to the TOA (satellite-measured)

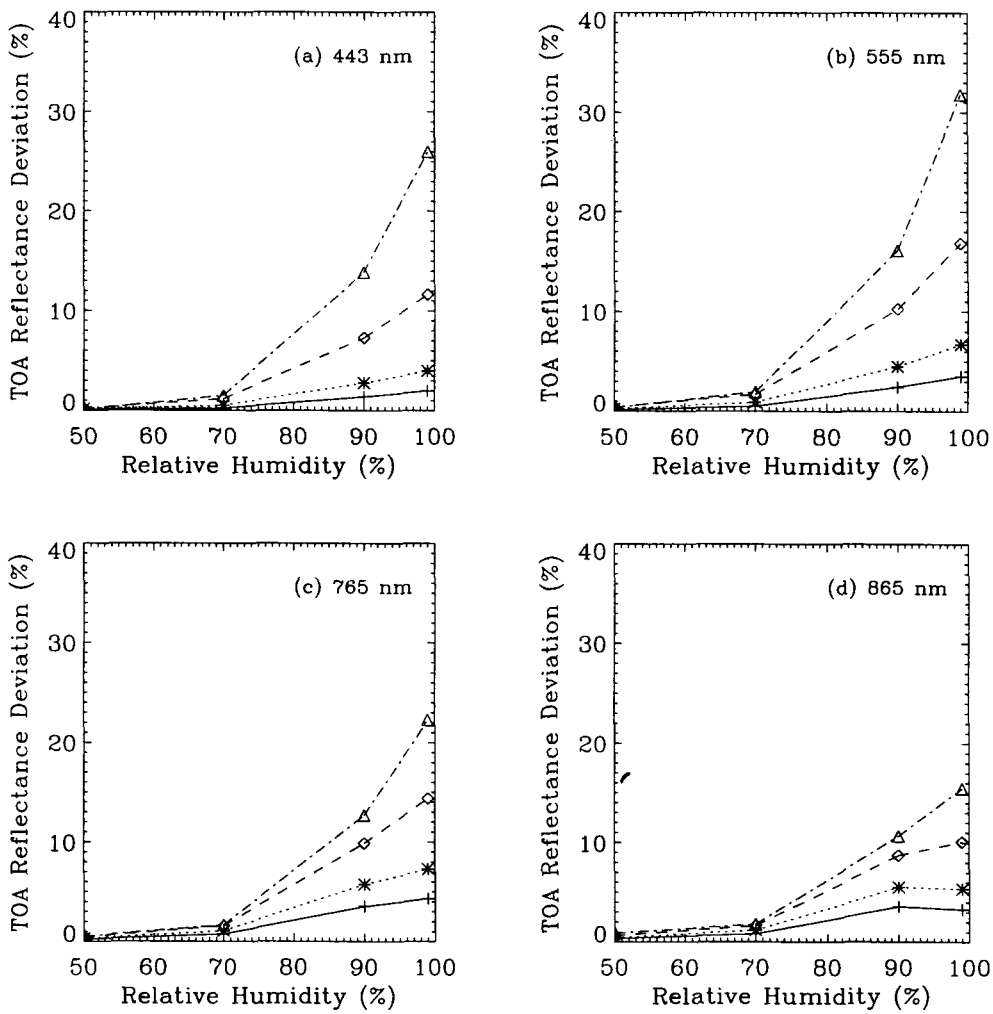

Figure 6.3 TOA reflectance deviation defined by Eq. (6.5) at 443, 555, 765 and 865 nm for the Tropospheric aerosol model. Solid curve: $\tau(865) = 0.05$; dotted curve: $\tau(865) = 0.1$; dashed curve: $\tau(865) = 0.3$; dashed-dotted curve: $\tau(865) = 0.8$.

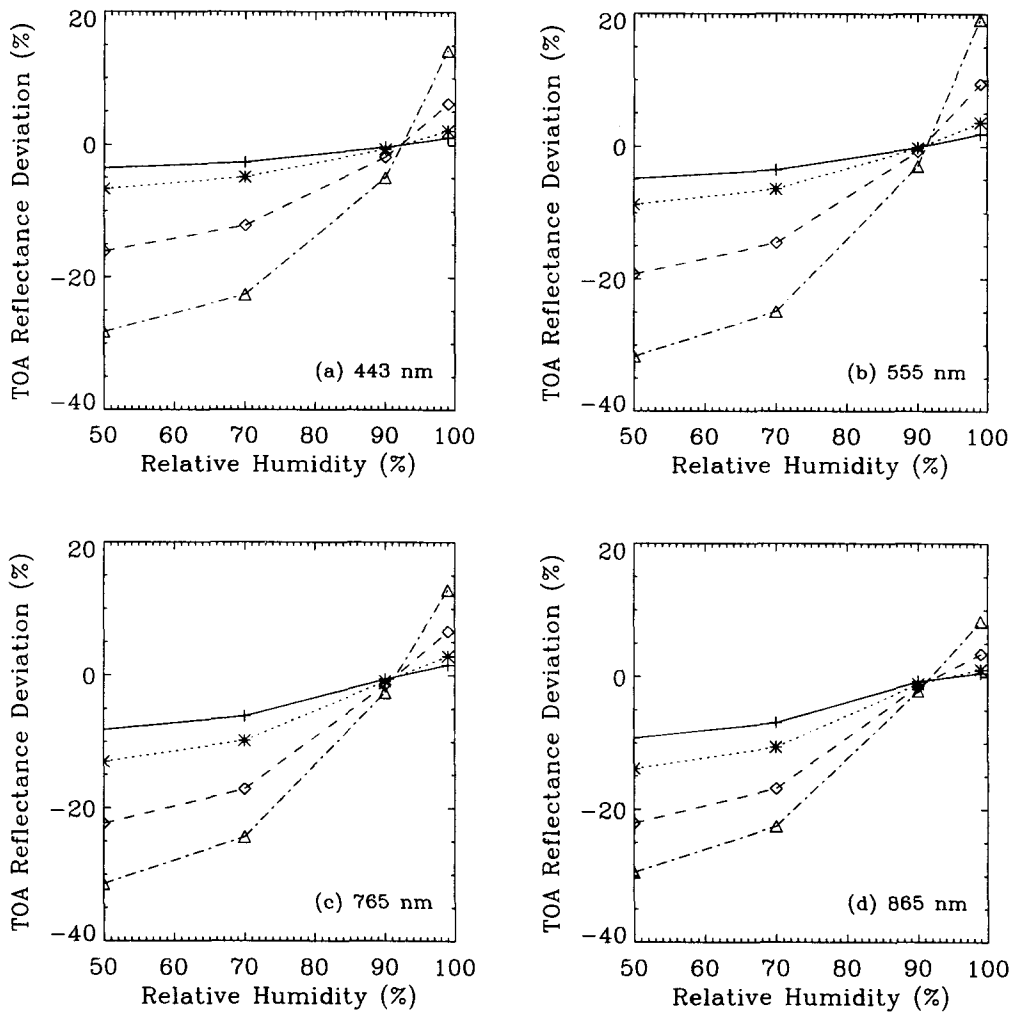

Figure 6.4 Same as Fig. 6.3 but for the Urban aerosol model.

reflectance. The ratio

$$\gamma(\lambda) = \rho_{path}(\lambda)/\rho_r(\lambda)$$

has been used for atmospheric correction purposes in the presence of strongly absorbing aerosols [13]. Hence, we show in Figs. 6.5 (a)-(d) the deviation in both $\epsilon_{ms}(765, 865)$ and $\gamma(765)$ between results obtained with the SC approach and corresponding results obtained with the MC approach. As in Eq. (6.5), the deviation is defined as the percentage difference between results generated with the SC approach as compared to the more realistic MC approach. Here Figs. 6.5 (a) and (b) pertain to the Tropospheric aerosol model, while (c) and (d) pertain to the Urban aerosol model. We note that there is a big difference between $\epsilon_{ms}(765, 865)$ and $\gamma(765)$ computed by the SC approach and by the more realistic MC approach. This implies that there will be an error in the retrieval of aerosol optical properties.

6.4 Conclusions

Many factors, such as e.g. (i) the break-down of the black pixel assumption in the NIR spectral region due to the algal blooms, or air bubbles or other "particles" in the ocean, and (ii) insufficient or inadequate aerosol models adopted for atmospheric correction, influence the accuracy of the atmospheric correction and thereby of ocean color retrievals. Aerosols in the atmosphere consist of a mixture of different components. Thus, their computed optical properties will depend on the assumptions we make about how they mix, and how they grow in size and change their indices of refraction when the humidity increases. For the purpose of atmospheric correction of ocean color imagery, it has been customary to assume that an effective particle model, in which aerosols with different compositions are averaged so as to arrive at a single-component (SC) aerosol model characterized by a "pseudo-particle" with an effective refractive index. This "pseudo-particle" is then

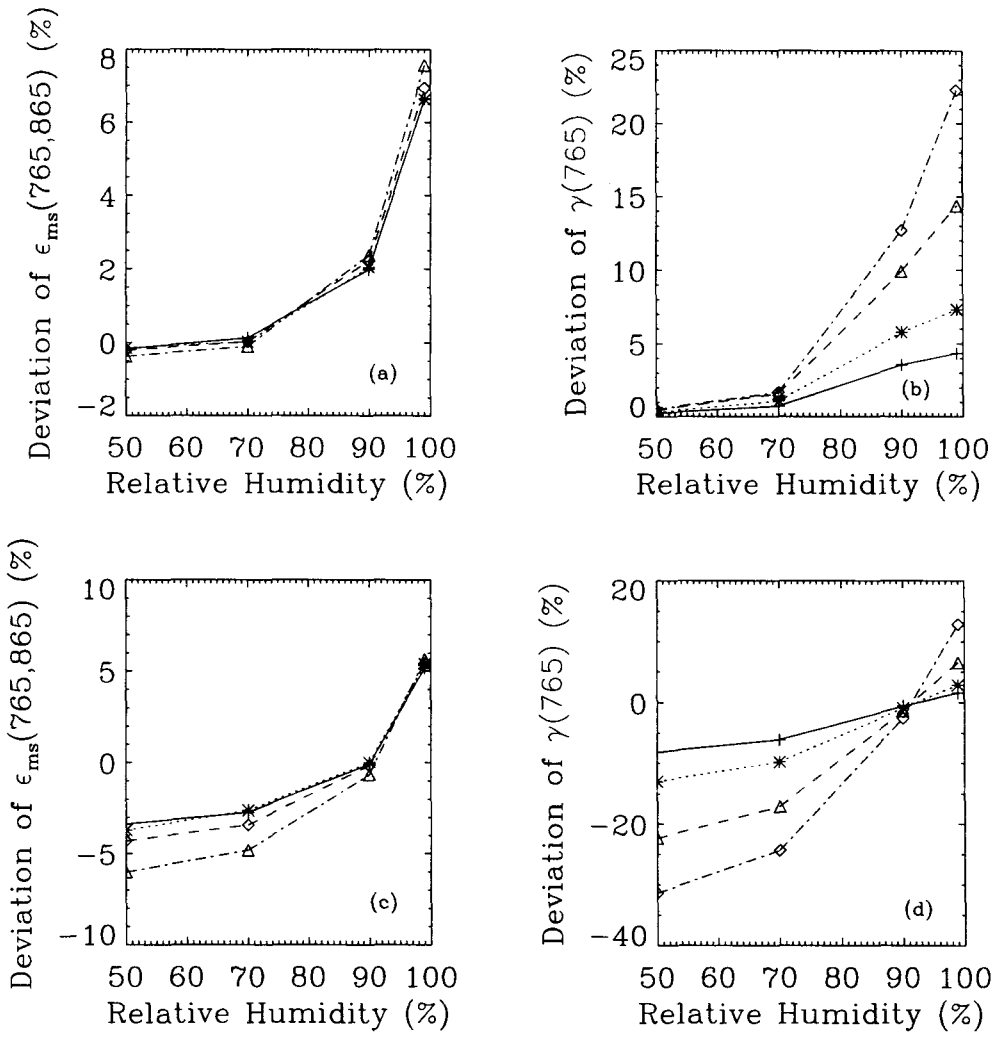

Figure 6.5 Deviations of $\epsilon_{ms}(765, 865)$ and $\gamma(765)$ computed with the SC approach as compared to the MC approach for several optical depths. Solid curve: $\tau_{865} = 0.05$; dotted curve: $\tau_{865} = 0.1$; dashed curve: τ_{865}=0.3; dashed-dotted curve: $\tau_{865} = 0.8$. (a) and (b) for the Tropospheric aerosol model. (c) and (d) for the Urban aerosol model.

allowed to grow and change its refractive index as the humidity increases. We have compared this approximate SC approach with the more realistic multi-component (MC) approach, in which each aerosol particle keeps its identity (characterized by its original size and refractive index), and is allowed to grow and change its refractive index with increasing humidity, independently of all the other particles. We have used the candidate aerosol models employed in the operational SeaWiFS atmospheric correction algorithm to assess the consequences of using the approximate SC approach instead of the more realistic MC approach in the retrieval process. The results show that the differences in the optical properties (the single scattering albedo, asymmetry factor and spectral dependence of the aerosol optical depth) obtained with the SC approach as compared to the MC approach are non-negligible. These differences in the optical properties lead to sufficiently large differences in the TOA reflectances that the resulting inaccuracy in the ocean color retrieval is significant and must be corrected. This implies that it becomes important to treat the light scattering by the aerosols correctly in order to obtain accurate and reliable atmospheric correction, and thus be able to retrieve the water-leaving radiance with sufficient accuracy that it can be used to infer chlorophyll concentrations and other marine constituents with known and reasonable accuracy. Retrieval of aerosol chemical and optical properties has received considerable attention in the atmospheric community due to their significance in atmospheric chemistry, and in climate investigations concerned with the direct and indirect (through clouds) influence of aerosols on the atmospheric radiation balance [116, 117, 118]. Correct treatment of aerosol optical properties is of paramount importance in all these investigations.

Chapter 7

Discussion and conclusions

Forward modeling of the propagation of radiation in the atmosphere-ocean system plays an important role in the remote sensing of ocean color imagery. The accuracy of the atmospheric correction depends crucially on the peformance of the forward model. Jin and Stamnes [1994] developed and numerically implemented the discrete ordinate method (DISORT) to compute radiances at the quadrature points (the discrete ordinates) by solving the radiative transfer equation pertinent for the coupled atmosphere-ocean system. Based upon this work, expressions for the radiance at arbitrary polar angles and at arbitrary levels in the coupled atmosphere-ocean system has been derived and numerically implemented in the first part of this thesis. Many factors, in addition to inadequate solution of the radiative transfer equation, such as (i) the break-down of the black pixel assumption in the NIR due to algal blooms or air bubbles in the ocean, and (ii) insufficient or inadequate optical properties of candidate aerosol models adopted for atmospheric correction, influence our ability to perform accurate atmospheric corrections and thereby accurate ocean color retrieval. Thus, in the second part of this thesis, radiative transfer modeling is used to study how the above factors impact the accuracy of atmospheric correction of ocean color imagery.

7.1 Derivation of expressions for the radiance at arbitrary polar angles in the coupled atmosphere-ocean system

The iteration of the source-function technique is utilized to derive analytic expressions for the radiance at arbitrary polar angles and at arbitrary levels in the coupled atmosphere-ocean system. These analytic expressions have been numerically implemented into an existing DISORT code pertinent for the coupled atmosphere-ocean system. The performance of the method is tested by applying it to three cases. It is shown that the analytic expressions yield not only the same solutions when evaluated at the quadrature points (as those provided by the quadrature scheme) (Appendix C gives a mathematical derivation in support of this conclusion) but are also superior to a spline interpolation that has previously been used in connection with the coupled atmosphere-ocean DISORT code. Since the propagation of the radiation in this coupled system occurs throughout the two media with different indices of refraction, the change in the line-of-sight direction across the interface between the atmosphere and the ocean must be taken into account when integrating the upward and downward radiances across this interface. This implies that the "bookkeeping" becomes somewhat complicated in this coupled system. This complexity explains in part why angular distributions of the radiation field in the coupled system had not been developed although the radiances at the quadrature points had been available for several years [Jin and Stamnes, 1994]. With this new extension, the ability of the DISORT code is significantly enhanced for applications to the coupled atmosphere-ocean system and to other systems that need to consider a change in the index of refraction between two strata.

Validation of the theoretical expressions and their subsequent numerical imple-

mentation plays a significant role in the development of radiative transfer modeling. In spite of the increasingly important role that the DISORT code for the coupled atmosphere-ocean system is playing in optical oceanography, the model has not been extensively tested against measured values of the quantities it predicts. This desirable model-data comparison is not presently possible because comprehensive oceanic optical data sets are not available due to limited measurements of the required physical variables. In this situation, model-model comparisons provides a valuable means to identify errors in coding or weaknesses in the mathematical representation of physical phenomena. Consequently, a comparison between the DISORT code and a Monte Carlo model is carried out by applying both codes to four test cases related to the coupled atmosphere-ocean system. A good agreement is obtained but comparison of simulated angular distributions of in-water light fields remains to be carried out.

7.2 Application of the DISORT code for the coupled atmosphere-ocean system to the remote sensing of ocean color

Atmospheric correction of ocean color imagery is a non-trivial task because a few percent error in the TOA reflectance in the near-infrared (NIR) bands will lead to a non-negligible error (e.g., an error larger than 5 % in the water-leaving radiance at 443 nm) in the retrieval of ocean color. Both atmospheric aerosols and the black pixel assumption invoked at NIR wavelengths play a critical role because the existing algorithms for atmospheric correction of ocean color are closely related to them. Our studies have shown that errors in the following three areas will significantly impair the accuracy of the atmospheric correction of ocean color imagery if

these errors are not properly corrected: 1) an inadequate bio-optical model used to compute the TOA water-leaving radiance at NIR wavelengths; 2) violation of the black pixel assumption due to water-leaving radiances resulting from oceanic air bubbles; 3) inadequacy of the optical properties of the candidate aerosol models computed by the SC approach.

7.2.1 Evaluation of a bio-optical model for the remote sensing reflectance at near-infrared wavelengths: Implication for ocean color retrieval

The performance of the bio-optical model for the NIR remote sensing reflectance used to compute the TOA water-leaving radiance at NIR wavelengths is inadequate for two reasons. One is that compared to the measured $R_{rs}(0^-, 670)$ (the remote sensing reflectance at nadir) assembled in the SeaBAM data base, the bio-optical model for the NIR remote sensing reflectance adopted by Siegel and co-workers overestimates the reflectance by a few of percent for the majority of the observed points. The othe reason is that a strong bi-directional dependence of the remote sensing reflectance just below the ocean surface is apparent in the simulations. This implies hat the isotropic assumption used in the operational algorithm for SeaWiFS imagery when computing the NIR water-leaving radiance to remedy the black pixel assumption would lead to erroneous atmospheric correction, because the bi-directional dependence of the NIR water-leaving radiance just below the ocean surface is not taken into account in the retrieval of ocean color imagery. Our simulations show that when the chlorophyll concentration is larger than 10.0 $mg{\cdot}m^{-3}$, the TOA NIR water-leaving reflectance deviation is up to 4 % and thus should be accounted for in atmospheric correction of ocean color imagery.

7.2.2 The role of oceanic air bubbles in atmospheric correction of ocean color imagery

This study focuses on the effect of oceanic air bubbles on the retrieval of the water-leaving reflectance at visible wavelengths through (i) the TOA reflectance deviation at both NIR and visible wavelengths, and (ii) the error in the retrieval of the TOA water-leaving reflectance in the visible. It is shown that the magnitude of the error incurred by ignoring oceanic air bubbles in the atmospheric correction of ocean color imagery depends on (i) the oceanic air bubble concentration, (ii) the coating thickness of the organic film surrounding the bubbles, (iii) the aerosol optical properties (scattering versus absorption), aerosol optical depth and phase function, and (iv) wavelength as follows.

7.2.2.1 The TOA reflectance deviation

The TOA reflectance deviation due to the contribution of oceanic air bubbles increases with increasing bubble concentration and coating thickness, and with decreasing aerosol optical depth. When the aerosol optical depth is less than 0.3, the bubble concentration is 10^7 m^{-3}, and the coating thickness is greater than 0.05 μm, this deviation is 2–4% in the NIR, and 7–17% in the visible. Thus, the NIR deviation is sufficiently large that the black pixel assumption becomes questionable, and the deviation in the visible will also incur an error in ocean color retrieval.

7.2.2.2 The error in the retrieval of the water-leaving reflectance

The error in the retrieval of the water-leaving reflectance in the visible due to the presence of oceanic air bubbles includes two parts: (i) extra upward radiance in the visible resulting from oceanic air bubbles, mistaken as water-leaving radiance due

to chlorophyll pigments; and (ii) erroneous atmospheric correction in the visible due to incorrect identification of aerosol model as a result of the violation of the black pixel assumption in the NIR. Simulations indicate that the first part of the error lies between 3 and 17% at 443 nm, and that the second part of the error lies between -4 and $+12\%$ at 443 nm.

7.2.3 Pitfalls in atmospheric correction of ocean color imagery: How should aerosol optical properties be computed?

In a humid environment optical properties of aerosols consisting of a mixture of several chemical components will depend on the assumptions we make about how they mix, and how they grow in size and change their indices of refraction when the humidity increases. For the purpose of atmospheric correction of ocean color imagery, it has been customary to assume that an effective particle model, in which aerosols with different chemical compositions are averaged so as to arrive at a single-component (SC) aerosol model characterized by a "pseudo-particle" with an effective refractive index. This "pseudo-particle" is then allowed to grow and change its refractive index as the humidity increases. We have compared this approximate SC approach with the more realistic multi-component (MC) approach, in which each aerosol particle keeps its identity (characterized by its original size and refractive index), and is allowed to grow and change its refractive index with increasing humidity, independent of all the other particles. The results show that the differences in the optical properties (the single scattering albedo, asymmetry factor and spectral dependence of the aerosol optical depth) obtained with the SC approach as compared to the MC approach are non-negligible. These differences in the optical properties lead to sufficiently large differences in the TOA reflectances

that the resulting inaccuracy in the ocean color retrieval is significant and must be corrected.

A few percent error in the TOA reflectance in the NIR bands will lead to a non-negligible error in the retrieval of ocean color. This amount can be caused by an inaccuracy in the computation of the optical properties of the candidate aerosol models or by the violation of the black-pixel assumption (BPA) in the NIR resulting from oceanic chlorophyll pigments as well as from oceanic air bubbles. The BPA is usually invoked in current algorithms for atmospheric correction of ocean color imagery. Since the differences in the optical properties of the candidate aerosol models computed using the SC approach compared to the more realistic MC approach lead to differences in the TOA reflectances which can be as large as or even larger than the contribution by the ocean to the TOA reflectance, it becomes extremely important to treat the light scattering by the aerosols correctly in order to obtain accurate and reliable atmospheric correction. An adequate algorithm for atmospheric correction of ocean color imagery should be based upon (i) adequate understanding and accurate computation of the inherent optical properties of the candidate aerosol models, and (2) an adequate bio-optical model for the dependence of the inherent optical properties on the chlorophyll pigment concentration. Thus, the findings in this thesis make an important contribution to the development of an adequate radiative transfer model for the coupled atmosphere-ocean system as well as to the algorithms for atmospheric correction of ocean color imagery. It is clear that a remaining challenge in the remote sensing of ocean color is to establish adequate procedures to measure the required physical variables related to atmospheric aerosols, oceanic chlorophyll pigments and air bubbles so that more convincing conclusions about these findings and an accurate algorithm for atmospheric correction of ocean color imagery can be obtained. Nevertheless, the findings presented in this study have provided a quantitative assessment of the

potential impact of atmospheric correction on ocean color imagery.

Appendix A

Derivation of the upward and downward source functions at arbitrary polar angles in the coupled atmosphere-ocean system in a slab geometry

In the discrete-ordinate approximation the integro-differental equations are replaced by a set of coupled linear differential equation as follows [63, 64]:

$$\mu_i \frac{dI^+(\tau,\mu_i)}{d\tau} = I^+(\tau,\mu_i) - S^+(\tau,\mu_i) \tag{A.1}$$

$$-\mu_i \frac{dI^-(\tau,\mu_i)}{d\tau} = I^-(\tau,\mu_i) - S^-(\tau,\mu_i) \tag{A.2}$$

$$S^+(\tau,\mu_i) = \frac{a}{2}\sum_{j=1}^{N} w_j p(\mu_j,\mu_i) I^+(\tau,\mu_j) + \frac{a}{2}\sum_{j=1}^{N} w_j p(-\mu_j,\mu_i) I^-(\tau,\mu_j) + S^{+*}(\tau,\mu_i) \tag{A.3}$$

$$S^-(\tau,\mu_i) = \frac{a}{2}\sum_{j=1}^{N} w_j p(\mu_j,-\mu_i) I^+(\tau,\mu_j) + \frac{a}{2}\sum_{j=1}^{N} w_j p(-\mu_j,-\mu_i) I^-(\tau,\mu_j) + S^{-*}(\tau,\mu_i). \tag{A.4}$$

Here we should explain carefully how the quadrature scheme is constructed. In the air (where we set $m_{ra} = 1$), we use $N = N_1$ qudrature angles in each hemisphere, and the corresponding qudrature points and weights are denoted by $\mu_i = \mu_i^a$ and $w_i = w_i^a$ $(i = 1, \cdots, N_1)$. Since the refractive index in the ocean, $m_{ro} = 1.34 > m_{ra}$, light incident on the air-ocean interface from above at the qudrature points μ_i^a; $i = 1, \cdots, N_1$ that span 2π steradians in the air, will be refracted into a cone less than 2π steradians in the ocean. Light in the ocean that is scattered out of this cone will suffer total reflection when it strikes the interface from below. To represent this light we must add additional quadrature angles. We therefore set $N = N_2 > N_1$ in the ocean where the additional points $(N_2 - N_1)$ cover the total reflection region. Thus, in the ocean we use $N = N_2$ qudrature angles in each hemisphere, and the corresponding qudrature points and weights are denoted by $\mu_i = \mu_i^o$ and $w_i = w_i^o$ $(i = 1, \cdots, N_2)$.

In view of these quadratue prescriptions we will for the sake of clarity rewrite Eqs. (A.3)and (A.4) separately for the air:

$$\begin{aligned} {S_{air}}^{\pm}(\tau,\mu) &= \frac{a}{2}\sum_{j=1}^{N_1} {w_j}^a p({\mu_j}^a, \pm\mu) I^+(\tau, {\mu_j}^a) \\ &\quad + \frac{a}{2}\sum_{j=1}^{N_1} {w_j}^a p(-{\mu_j}^a, \pm\mu) I^-(\tau, {\mu_j}^a) + S_{air}^{\pm *}(\tau,\mu_i) \end{aligned} \tag{A.5}$$

and the ocean:

$$S_{ocn}{}^{\pm}(\tau,\mu) = \frac{a}{2}\sum_{j=1}^{N_2} w_j{}^{o} p(\mu_j{}^{o},\pm\mu) I^{+}(\tau,\mu_j{}^{o}) + \frac{a}{2}\sum_{j=1}^{N_2} w_j{}^{o} p(-\mu_j{}^{o},\pm\mu) I^{-}(\tau,\mu_j{}^{o}) + S_{ocn}^{\pm *}(\tau,\mu_i) \quad (A.6)$$

where the beam source in the air is given by

$$S_{air}{}^{\pm *}(\tau,\mu_i) = X_0^{\pm}(\mu_i) e^{-\tau/\mu_0} + X_{01}^{\pm}(\mu_i) e^{\tau/\mu_0} \quad (A.7)$$

and in the ocean by

$$S_{ocn}{}^{\pm *}(\tau,\mu_i) = X_{02}^{\pm}(\mu_i) e^{-\tau/\mu_{0m}}. \quad (A.8)$$

Here

$$X_0^{\pm}(\mu) = \frac{aF^s}{4\pi} p(-\mu_0,\pm\mu) \quad (A.9)$$

$$X_{01}^{\pm}(\mu) = \frac{aF^s}{4\pi} \rho_s(-\mu_0; m_{rel}) e^{-\frac{2\tau_a}{\mu_0}} p(-\mu_0,\pm\mu) \quad (A.10)$$

and

$$X_{02}^{\pm}(\mu) = \frac{aF^s}{4\pi}\frac{\mu_0}{\mu_{om}} \mathcal{T}_b(-\mu_0,-\mu_{0m};m_{rel}) e^{-\tau_a(\frac{1}{\mu_0}-\frac{1}{\mu_{0m}})} p(-\mu_{0m},\pm\mu) \quad (A.11)$$

where $\mu_0 = cos\theta_0$, θ_0 is the solar enoth angle, $\mu_{om} = \sqrt{1-[(1-\mu_0{}^2)/m_{rel}^2]}$, $m_{rel} = m_{ocn}/m_{air}$, τ_a is the optical depth at the bottom of atmosphere, and $\rho_s(-\mu_0; m_{rel})$ and $\mathcal{T}_b(-\mu_0,-\mu_{om};m_{rel})$ are the specular reflectance and transmittance of the invariant intensity, respectively.

In the discrete-ordinate approximation, solutions to Eqs. (A.1) and (A.2) applicable to two adjacent slabs with different refractive indices (such as atmosphere-ocean system) are as follows [63, 64]:

$$I^{\pm}(\tau,\mu_i{}^a) = \sum_{j=1}^{N_1} C_{-j}g_{-j}(\pm\mu_i{}^a)e^{k_j{}^a\tau} + \sum_{j=1}^{N_1} C_j g_j(\pm\mu_i{}^a)e^{-k_j{}^a\tau} + Z_0(\pm\mu_i{}^a)e^{-\frac{\tau}{\mu_o}} + Z_{01}(\pm\mu_i{}^a)e^{\frac{\tau}{\mu_o}} \quad (A.12)$$

$$I^{\pm}(\tau,\mu_i{}^o) = \sum_{j=1}^{N_2} C_{-j}g_{-j}(\pm\mu_i{}^o)e^{k_j{}^o\tau} + \sum_{j=1}^{N_2} C_j g_j(\pm\mu_i{}^o)e^{-k_j{}^o\tau} + Z_{02}(\pm\mu_i{}^o)e^{-\frac{\tau}{\mu_{om}}} \quad (A.13)$$

where the $Z_0(\mu_i{}^a)$, $Z_{01}(\mu_i{}^a)$ and $Z_{02}(\mu_i{}^o)$ are determined by the following system of linear algebraic equations:

$$\sum_{j=-N_1}^{N_1,j\neq 0}\left[(1+\frac{\mu_j{}^a}{\mu_0})\delta_{ij} - w_j{}^a\frac{a}{2}p(\mu_i{}^a,\mu_j{}^a)\right]Z_0(\mu_j{}^a) = X_0(\mu_i{}^a) \quad (A.14)$$

$$\sum_{j=-N_1}^{N_1,j\neq 0}\left[(1-\frac{\mu_j{}^a}{\mu_0})\delta_{ij} - w_j{}^a\frac{a}{2}p(\mu_i{}^a,\mu_j{}^a)\right]Z_{01}(\mu_j{}^a) = X_{01}(\mu_i{}^a) \quad (A.15)$$

and

$$\sum_{j=-N_2}^{N_2,j\neq 0}\left[(1+\frac{\mu_j{}^o}{\mu_{0m}})\delta_{ij} - w_j{}^o\frac{a}{2}p(\mu_i{}^o,\mu_j{}^o)\right]Z_{02}(\mu_j{}^o) = X_{02}(\mu_i{}^o). \quad (A.16)$$

where $\mu_i{}^o = \sqrt{1-\frac{(1-(\mu_i{}^a)^2)}{m_{rel}{}^2}}$.

Substituting the expressions Eq. (1) into Eq. (2), finally we have

$$S^{\pm}{}_{air}(\tau,\mu^a) = \sum_{j=1}^{N_1} C_{-j}\tilde{g}_{-j}(\pm\mu^a)e^{k_j{}^a\tau} + \sum_{j=1}^{N_1} C_j\tilde{g}_j(\pm\mu^a)e^{-k_j{}^a\tau} + \tilde{Z}_0(\pm\mu^a)e^{-\frac{\tau}{\mu_0}} + \tilde{Z}_{01}(\pm\mu^a)e^{\frac{\tau}{\mu_0}} \quad (A.17)$$

where

$$\tilde{g}_j(\pm\mu^a) = \frac{a}{2}\sum_{i=1}^{N_1}\{w_i{}^a p(-\mu_i{}^a,\pm\mu^a)g_j(-\mu_i{}^a) + w_i{}^a p(+\mu_i{}^a,\pm\mu^a)g_j(+\mu_i{}^a)\} \quad (A.18)$$

and

$$\tilde{Z}_0(\pm\mu^a) = \frac{a}{2}\sum_{i=1}^{N_1}\{w_i{}^a p(-\mu_i{}^a, \pm\mu^a) Z_0(-\mu_i{}^a) + w_i{}^a p(+\mu_i{}^a, \pm\mu^a) Z_0(+\mu_i{}^a)\} + X_{01}(\pm\mu^a) \tag{A.19}$$

$$\tilde{Z}_{01}(\pm\mu^a) = \frac{a}{2}\sum_{i=1}^{N_1}\{w_i{}^a p(-\mu_i{}^a, \pm\mu^a) Z_{01}(-\mu_i{}^a) + w_i{}^a p(+\mu_i{}^a, \pm\mu^a) Z_{01}(+\mu_i{}^a)\} + X_{01}(\pm\mu^a) \tag{A.20}$$

Similarly, we obtain in the ocean

$$S^{\pm}{}_{ocn}(\tau, \mu^o) = \sum_{j=1}^{N_2} C_{-j}\tilde{g}_{-j}(\pm\mu^o) e^{k_j{}^o\tau} + \sum_{j=1}^{N_2} C_j \tilde{g}_j(\pm\mu^o) e^{-k_j{}^o\tau} + \tilde{Z}_{02}(\pm\mu^o) e^{-\frac{\tau}{\mu_{om}}} \tag{A.21}$$

where

$$\tilde{g}_j(\pm\mu^o) = \frac{a}{2}\sum_{i=1}^{N_2}\{w_i{}^o p(-\mu_i{}^o, \pm\mu^o) g_j(-\mu_i{}^o) + w_i{}^o p(+\mu_i{}^o, \pm\mu^o) g_j(+\mu_i{}^o)\} \tag{A.22}$$

and

$$\tilde{Z}_{02}(\pm\mu^o) = \frac{a}{2}\sum_{i=1}^{N_2}\{w_i{}^o p(-\mu_i{}^o, \pm\mu^o) Z_{02}(-\mu_i{}^o) + w_i{}^o p(+\mu_i{}^o, \pm\mu^o) Z_{02}(+\mu_i{}^o)\} + X_{02}(\pm\mu^o). \tag{A.23}$$

Appendix B

Derivation of the integral expression of the radiance at arbitrary polar angles in the atmosphere

B.1 Derivation of the integral expression of the upward radiance at arbitrary polar angles in the atmosphere ($\tau_0 \leq \tau \leq \tau_a$)

Consider

$$\int_{\tau_b}^{\tau} d(I^+(\tau,\mu)e^{-\frac{\tau}{\mu}}) = \int_{\tau_b}^{\tau} (-\frac{S^+(\tau,\mu)}{\mu} e^{-\frac{\tau}{\mu}}) d\tau \tag{B.1}$$

Due to the change in the LOS across the interface between the atmosphere and ocean, the integral of Eq. (B.1) from τ_b to τ is computed on the three sub-integrals as follows: (1) τ_b to ${\tau_a}^+$, (2) ${\tau_a}^+$ to τ_a and (3) τ_a to τ, where $\tau_0 \leq \tau \leq \tau_a$.

Firstly, the right hand side (RHS) of Eq. (B.1) becomes

$$RHS = -\int_{\tau_b}^{\tau} \frac{d\tau'}{\mu} e^{-\tau'/\mu} S^{+}(\tau', \mu) = -\int_{\tau_b}^{{\tau_a}^{+}} (ocean) - \int_{{\tau_a}^{+}}^{\tau_a} (interface) - \int_{\tau_a}^{\tau} (atmosphere) \tag{B.2}$$

where the integrands denoted by $(ocean)$, $(interface)$ and $(atmosphere)$ are to be replaced by the appropriate source function to be integrated.

Since ${\tau_a}^{+} = \tau_a + \varepsilon$ and the integrand denoted by $(ocean)$ is finite, the 2nd term will vanish on the right side of the equation when $\varepsilon \to 0$.

Thus, Eq. (B.2) is simplified to read

$$RHS = -\int_{\tau_b}^{{\tau_a}^{+}} \frac{d\tau'}{\mu^o} e^{-\tau'/\mu^o} {S^{+}}_{ocn}(\tau', \mu^o) - \int_{\tau_a}^{\tau} \frac{d\tau'}{\mu^a} e^{-\tau'/\mu^a} {S^{+}}_{air}(\tau', \mu^a) \tag{B.3}$$

where we have included the proper integrands into the equation.

The left hand side (LHS) of Eq. (B.1) becomes

$$LHS = \int_{\tau_b}^{\tau} d(I^{+}(\tau', \mu) e^{-\tau'/\mu}) = \int_{\tau_b}^{{\tau_a}^{+}} (ocean) + \int_{{\tau_a}^{+}}^{\tau_a} (interface) + \int_{\tau_a}^{\tau} (atmosphere) \tag{B.4}$$

where we omitted the integrands $[d(I^{+}(\tau, \mu) e^{-\frac{\tau}{\mu}})]$ on the right of the equation.

Similarly, one notes that the 2nd term on the equation vanishes when $\varepsilon \to 0$ because ${\tau_a}^{+} = \tau_a + \varepsilon$ and the integrand is finite (to be replaced by the interface condition).

Hence, Eq. (B.4) only leaves

$$LHS = \int_{\tau_b}^{{\tau_a}^{+}} d(I^{+}(\tau', \mu^o) e^{-\tau'/\mu^o}) + \int_{\tau_a}^{\tau} d(I^{+}(\tau', \mu^a) e^{-\tau'/\mu^a}) \tag{B.5}$$

where we have included the integrands into the equation and used $\mu = \mu^a$ in the atmosphere and $\mu = \mu^o$ in the ocean.

To simplify Eq. (B.3) and (B.5), we use Eq. (B.1) by setting $\tau = {\tau_a}^+$ (in a consistent integral region) as follows:

$$\int_{\tau_b}^{{\tau_a}^+} d(I^+(\tau,\mu)e^{-\frac{\tau}{\mu}}) = \int_{\tau_b}^{{\tau_a}^+} (-\frac{{S^+}_{ocn}(\tau,\mu)}{\mu} e^{-\frac{\tau}{\mu}}) d\tau \tag{B.6}$$

where the source function $S^+(\tau,\mu)$ has been replaced by ${S^+}_{ocn}(\tau,\mu)$.

With this simplification, we obtain from setting Eq. (B.3) equal to Eq. (B.5)

$$I^+(\tau,\mu^a) = I^+(\tau_a,\mu^a)e^{-(\tau_a/\mu^a - \tau/\mu^a)} + e^{\tau/\mu^a} \int_{\tau}^{\tau_a} \frac{d\tau'}{\mu^a} e^{-\tau_l/\mu^a} {S^+}_{air}(\tau',\mu^a) \tag{B.7}$$

where $I^+(\tau_a,\mu^a)$ is determined by [63, 64]:

(1) when μ^o is in the refraction region

$$I^+(\tau_a,\mu^a) = I^-(\tau_a,\mu^a)\rho_s(-\mu^a, m_{rel}) + \left[\frac{I^+({\tau_a}^+,\mu^o)}{{m_{rel}}^2}\right] \mathcal{T}_s(+\mu^o, m_{rel}) \tag{B.8}$$

(2) when μ^o is in the totally reflected region

$$I^+(\tau_a,\mu^a) = I^-(\tau_a,\mu^a)\rho_s(-\mu^a, m_{rel}) \tag{B.9}$$

B.2 Derivation of the integral expressions of the downward radiance at arbitrary polar angles in the ocean ($\tau_b \geq \tau \geq {\tau_a}^+$)

Consider

$$\int_{\tau_0}^{\tau} d(I^-(\tau,\mu)e^{\frac{\tau}{\mu}}) = \int_{\tau_0}^{\tau} (\frac{S^-(\tau,\mu)}{\mu} e^{\frac{\tau}{\mu}}) d\tau \tag{B.10}$$

One notes that the integrand in Eq. (B.10) is discontinuous in this integral region when $\tau_b \geq \tau \geq {\tau_a}^+$ due to the discontinuity across the interface between the atmosphere and ocean, and thus will be integrated in the three regions as follows.

From the RHS of Eq. (B.10), we have

$$RHS = \int_{\tau_0}^{\tau} d\tau' \left(\frac{S^-(\tau',\mu)}{\mu} e^{\frac{\tau'}{\mu}}\right) = \int_{\tau_0}^{\tau_a} (atmosphere) + \int_{\tau_a}^{\tau_a{}^+} (interface) + \int_{\tau_a{}^+}^{\tau} (ocean) \tag{B.11}$$

where the integrands denoted by (*ocean*), (*interface*) and (*atmosphere*) are to be replaced by the appropriate source function to be integrated.

One notices that the second term on the right side of equation $\rightarrow 0.0$ when $\varepsilon \rightarrow 0$ because $\tau_a{}^+ = \tau_a + \varepsilon$ and the integrated function is finite. Thus, Eq. (B.11) is simplified to be

$$RHS = \int_{\tau_0}^{\tau_a} \frac{d\tau'}{\mu^a} e^{\tau'/\mu^a} S^-{}_{air}(\tau', \mu^a) + \int_{\tau_a{}^+}^{\tau} \frac{d\tau'}{\mu^o} e^{\tau'/\mu^o} S^-{}_{ocn}(\tau', \mu^o) \tag{B.12}$$

where we put proper integrands into the expressions and use $\mu = \mu^a$ in the atmosphere and $\mu = \mu^o$ in the ocean.

We integrate the LHS of Eq. (B.10) as follows:

$$LHS = \int_{\tau_0}^{\tau_a} d(I^-(\tau,\mu)e^{\tau/\mu}) + \int_{\tau_a}^{\tau_a{}^+} d(I^-(\tau,\mu)e^{\tau/\mu}) + \int_{\tau_a{}^+}^{\tau} d(I^-(\tau,\mu)e^{\tau/\mu}) \tag{B.13}$$

Similarly, we note that the 2nd term vanishes when $\varepsilon \rightarrow 0.0$ because $\tau_a{}^+ = \tau_a + \varepsilon$ and the integrand is finite (to be replaced by the interface condition).

So Eq. (B.13) simplifies to

$$LHS = \int_{\tau_0}^{\tau_a} d(I^-(\tau,\mu)e^{\tau/\mu}) + \int_{\tau_a{}^+}^{\tau} d(I^-(\tau,\mu)e^{\tau/\mu}) \tag{B.14}$$

Similarly, we use Eq. (B.10) by setting $\tau = \tau_a$ as follows

$$\int_{\tau_0}^{\tau_a} d(I^-(\tau,\mu)e^{\frac{\tau}{\mu}}) = \int_{\tau_0}^{\tau_a} \left(\frac{S^-{}_{air}(\tau,\mu)}{\mu} e^{\frac{\tau}{\mu}}\right) d\tau \tag{B.15}$$

where the source function $S^-(\tau,\mu)$ has been replaced by $S^-{}_{air}(\tau,\mu)$.

With this simplification we obtain from setting Eq. (B.12) equal to Eq. (B.14)

$$I^-(\tau,\mu) = I^-(\tau_a{}^+,\mu^o)e^{(\tau_a{}^+/\mu^o - \tau/\mu^o)} + e^{-\tau/\mu^o} \int_{\tau_a{}^+}^{\tau} \frac{d\tau'}{\mu^o} e^{\tau'/\mu^o} S^-{}_{ocn}(\tau', \mu^o) \tag{B.16}$$

where $I^-(\tau_a{}^+,\mu^o)$ is determined by [63, 64]:

1. when μ^o is in the refraction region, $I^-(\tau_a{}^+, \mu^o)$ is determined by

$$\frac{I^-(\tau_a{}^+, \mu^o)}{{m_{rel}}^2} = \left[\frac{I^+(\tau_a{}^+, \mu^o)}{{m_{rel}}^2}\right] \rho_s(+\mu^o, m_{rel}) + I^-(\tau_a, \mu^a)\Gamma_s(-\mu^a, m_{rel}) \quad \text{(B.17)}$$

2. when μ^o is in the totally-reflected region, $I^-(\tau_a{}^+, \mu^o)$ is determined by

$$I^-(\tau_a{}^+, \mu^o) = I^+(\tau_a{}^+, \mu^o) \quad \text{(B.18)}$$

Appendix C

Evaluation of the radiance expressions for arbitrary polar angles at quadrature angles

We may prove from the basic radiative transfer equations that

$$\tilde{g}_j(\pm\mu_i) = (1 \pm k_j\mu_i)g_j(\pm\mu_i) \tag{C.1}$$

and

$$\tilde{Z}_0(\pm\mu_i) = (1 \pm k_0\mu_i)Z_0(\pm\mu_i) \tag{C.2}$$

$$\tilde{Z}_{01}(\pm\mu_i) = (1 \mp k_0\mu_i)Z_{01}(\pm\mu_i) \tag{C.3}$$

where the $\tilde{g}_j(\pm\mu_i)$, $\tilde{Z}_0(\pm\mu_i)$ and $\tilde{Z}_{01}(\pm\mu_i)$ are as follows:

$$\tilde{g}_j(\pm\mu^a) = \frac{a}{2}\sum_{i=1}^{N_1}\{w_i{}^a p(-\mu_i{}^a, \pm\mu^a)g_j(-\mu_i{}^a) + w_i{}^a p(+\mu_i{}^a, \pm\mu^a)g_j(+\mu_i{}^a)\} \tag{C.4}$$

and

$$\tilde{Z}_0(\pm\mu^a) = \frac{a}{2}\sum_{i=1}^{N_1}\{w_i{}^a p(-\mu_i{}^a, \pm\mu^a)Z_0(-\mu_i{}^a)+w_i{}^a p(+\mu_i{}^a, \pm\mu^a)Z_0(+\mu_i{}^a)\}+X_{01}(\pm\mu^a) \tag{C.5}$$

$$\tilde{Z}_{01}(\pm\mu^a) = \frac{a}{2}\sum_{i=1}^{N_1}\{w_i{}^a p(-\mu_i{}^a, \pm\mu^a) Z_{01}(-\mu_i{}^a) + w_i{}^a p(+\mu_i{}^a, \pm\mu^a) Z_{01}(+\mu_i{}^a)\} + X_{01}(\pm\mu^a) \tag{C.6}$$

We will evaluate the radiance expressions derived using the iteration of source function at quadrature points and check whether they may yield to the simpler expressions using the quadrature scheme.

C.1 Evaluate upward radiances at quadrature points

C.1.1 $\tau_b \geq \tau \geq \tau_a{}^+$, i.e., in the ocean

We have obtained

$$I^+(\tau, \mu^o) = I^+(\tau_b, \mu^o) e^{-\frac{(\tau_b - \tau)}{\mu^o}} + \sum_{j=-N_2}^{N_2} \frac{C_j \tilde{g}_j(+\mu^o)}{(1 + k_j{}^o \mu^o)} \{e^{-k_j{}^o \tau} - e^{-\left[k_j{}^o \tau_b + \frac{(\tau_b - \tau)}{\mu^o}\right]}\} \tag{C.7}$$

with the notation

$$I^+{}_{ocn}(\tau, \mu^o) = \sum_{j=-N_2}^{N_2} \frac{C_j \tilde{g}_j(+\mu^o)}{(1 + k_j{}^o \mu^o)} \{e^{-k_j{}^o \tau} - e^{-\left[k_j{}^o \tau_b + \frac{(\tau_b - \tau)}{\mu^o}\right]}\} \tag{C.8}$$

We first evaluate $I^+{}_{ocn}(\tau, \mu^o)$ at the quadrature points and by substituting Eqs. (C.1) and (C.3) into Eq. (C.8) we obtain:

$$I^+{}_{ocn}(\tau, \mu^o) = \sum_{j=-N_2}^{N_2} C_j g_j(+\mu_i{}^o) \{e^{-k_j{}^o \tau} - e^{-\left[k_j{}^o \tau_b + \frac{(\tau_b - \tau)}{\mu_i{}^o}\right]}\} \tag{C.9}$$

According to the simple expressions of the radiance at quadrature points [63, 64], i.e.,

$$I^{\pm}(\tau, \mu_i{}^o) = \sum_{j=1}^{N_2} C_{-j} g_{-j}(\pm\mu_i{}^o) e^{k_j{}^o \tau} + \sum_{j=1}^{N_2} C_j g_j(\pm\mu_i{}^o) e^{-k_j{}^o \tau} + Z_{02}(\pm\mu_i{}^o) e^{-\frac{\tau}{\mu_{om}}} \tag{C.10}$$

we rewrite Eq. (C.9) as

$$I^{+}{}_{ocn}(\tau,\mu^{o})(\mu^{o}=\mu_{i}{}^{o}) = I^{+}(\tau,\mu_{i}{}^{o}) - I^{+}(\tau_{b},\mu_{i}{}^{o})e^{-\frac{(\tau_{b}-\tau)}{\mu_{i}{}^{o}}} \tag{C.11}$$

Thus substituting this equation into Eq. (C.7), we obtain

$$I^{+}(\tau,\mu^{o})(\mu^{o}=\mu_{i}{}^{o}) = I^{+}(\tau_{b},\mu_{i}{}^{o})e^{-\frac{(\tau_{b}-\tau)}{\mu_{i}{}^{o}}} + I^{+}(\tau,\mu_{i}{}^{o}) - I^{+}(\tau_{b},\mu_{i}{}^{o})e^{-\frac{(\tau_{b}-\tau)}{\mu_{i}{}^{o}}} = I^{+}(\tau,\mu_{i}{}^{o}) \tag{C.12}$$

Thus this proves that the upward radiance expressions derived using the iteration of the source function technique yields results at quadrature points identical to those found from the solutions using the quadrature scheme.

C.1.2 $\tau_a \geq \tau \geq \tau_0$, i.e., in the atmosphere

We have obtained

$$I^{+}(\tau,\mu^{a}) = I^{+}(\tau_{a},\mu^{a})e^{(\tau/\mu^{a}-\tau_{a}/\mu^{a})} + I^{+}{}_{air}(\tau,\mu^{a}) \tag{C.13}$$

with

$$\begin{aligned} I^{+}{}_{air}(\tau,\mu^{a}) &= \sum_{j=-N_1}^{N_1} \frac{C_j\tilde{g}_j(+\mu)}{(1+k_j{}^{a}\mu^{a})}\{e^{-k_j{}^{a}\tau} - e^{-\left[k_j{}^{a}\tau_a+\frac{(\tau_a-\tau)}{\mu^{a}}\right]}\} \\ &\quad + \frac{\tilde{Z}_{01}(+\mu^{a})}{(1+k_0{}^{a}\mu^{a})}\left[e^{k_0{}^{a}\tau_a-\frac{(\tau_a-\tau)}{\mu^{a}}} - e^{k_0{}^{a}\tau}\right] \end{aligned} \tag{C.14}$$

where$I^{+}(\tau_a,\mu^{a})$ is determined by the boundary condition.

To evaluate $I^{+}(\tau,\mu^{a})$ at quadrature points, we first obtain

$$\begin{aligned} I^{+}{}_{air}(\tau,\mu_{i}{}^{a}) &= \sum_{j=-N_1}^{N_1} \frac{C_j\tilde{g}_j(+\mu_i)}{(1+k_j{}^{a}\mu_{i}{}^{a})}\{e^{-k_j{}^{a}\tau} - e^{-\left[k_j{}^{a}\tau_a+\frac{(\tau_a-\tau)}{\mu_{i}{}^{a}}\right]}\} \\ &\quad + \frac{\tilde{Z}_{01}(+\mu_{i}{}^{a})}{(1+k_0{}^{a}\mu_{i}{}^{a})}\left[e^{k_0{}^{a}\tau_a-\frac{(\tau_a-\tau)}{\mu_{i}{}^{a}}} - e^{k_0{}^{a}\tau}\right] \end{aligned} \tag{C.15}$$

Substituting Eqs.(C.1) $\sim$ (C.3) into Eq. (C.15), we get

$$I^{+}{}_{air}(\tau,\mu_i{}^a) = \sum_{j=-N_1}^{N_1} C_j g_j(+\mu_i{}^a)\{e^{-k_j{}^a\tau} - e^{-\left[k_j{}^a\tau_a+\frac{(\tau_a-\tau)}{\mu_i{}^a}\right]}\} + Z_{01}(+\mu_i{}^a)\left[e^{k_0{}^a\tau_a-\frac{(\tau_a-\tau)}{\mu_i{}^a}} - e^{k_0{}^a\tau}\right] \quad \text{(C.16)}$$

Use the radiance expression at quadrature points [63, 64], i.e,

$$I^{\pm}(\tau,\mu_i{}^a) = \sum_{j=1}^{N_1} C_{-j} g_{-j}(\pm\mu_i{}^a)e^{k_j{}^a\tau} + \sum_{j=1}^{N_1} C_j g_j(\pm\mu_i{}^a)e^{-k_j{}^a\tau} + Z_0(\pm\mu_i{}^a)e^{-\frac{\tau}{\mu_{io}}} + Z_{01}(\pm\mu_i{}^a)e^{\frac{\tau}{\mu_{io}}} \quad \text{(C.17)}$$

Then we obtain

$$I^{+}{}_{air}(\tau,\mu_i{}^a) = I^{+}(\tau,\mu_i{}^a) - I^{+}(\tau_a,\mu_i{}^a)e^{-(\tau_a/\mu_i{}^a-\tau/\mu_i{}^a)} \quad \text{(C.18)}$$

Combining Eq. (C.13) at quadrature points and Eq. (C.18), all terms are cancelled except for $I^{+}(\tau,\mu_i{}^a)$, we have

$$I^{+}(\tau,\mu^a)(\mu^a = \mu_i{}^a) = I^{+}(\tau,\mu_i{}^a) \quad \text{(C.19)}$$

Thus this proves that the upward radiance expressions in the atmosphere derived using the iteration of source function yield to the solution at quadrature points.

C.2 Evaluate downward radiance at quadrature points

C.2.1 $\tau_a \geq \tau \geq \tau_0$, i.e., in the atmosphere

We have gotten

$$I^{-}(\tau,\mu^a) = I^{-}(\tau_0,\mu^a)e^{-\frac{(\tau-\tau_0)}{\mu^a}} + I^{-}{}_{air}(\tau,\mu^a) \quad \text{(C.20)}$$

where

$$I^{-}{}_{air}(\tau,\mu^{a}) = \sum_{j=-N_1}^{N_1}\frac{C_j\tilde{g}_j(-\mu^{a})}{(1-k_j{}^{a}\mu^{a})}\{e^{-k_j{}^{a}\tau}-e^{-\left[k_j{}^{a}\tau_0+\frac{(\tau-\tau_0)}{\mu^{a}}\right]}\} + \frac{\tilde{Z}_{01}(-\mu^{a})}{(1+k_0{}^{a}\mu^{a})}\{e^{k_0{}^{a}\tau}-e^{k_0{}^{a}\tau_0-\frac{(\tau-\tau_0)}{\mu^{a}}}\} \quad \text{(C.21)}$$

To evaluate at quadrature points, we first have,

$$I^{-}{}_{air}(\tau,\mu_i{}^{a}) = \sum_{j=-N_1}^{N_1}\frac{C_j\tilde{g}_j(-\mu_i{}^{a})}{(1-k_j{}^{a}\mu_i{}^{a})}\{e^{-k_j{}^{a}\tau}-e^{-\left[k_j{}^{a}\tau_0+\frac{(\tau-\tau_0)}{\mu_i{}^{a}}\right]}\} + \frac{\tilde{Z}_{01}(-\mu_i{}^{a})}{(1+k_0{}^{a}\mu_i{}^{a})}\{e^{k_0{}^{a}\tau}-e^{k_0{}^{a}\tau_0-\frac{(\tau-\tau_0)}{\mu_i{}^{a}}}\} \quad \text{(C.22)}$$

Then by substituting Eqs. (C.1) $\sim$ (C.3) into the Eq. (C.22), we obtain

$$I^{-}{}_{air}(\tau,\mu_i{}^{a}) = \sum_{j=-N_1}^{N_1} C_j g_j(-\mu_i{}^{a})\{e^{-k_j{}^{a}\tau}-e^{-\left[k_j{}^{a}\tau_0+\frac{(\tau-\tau_0)}{\mu_i{}^{a}}\right]}\} + Z_{01}(-\mu_i{}^{a})\{e^{k_0{}^{a}\tau}-e^{k_0{}^{a}\tau_0-\frac{(\tau-\tau_0)}{\mu_i{}^{a}}}\} \quad \text{(C.23)}$$

Use the radiance expression at quadrature points [63, 64], i.e,

$$I^{\pm}(\tau,\mu_i{}^{a}) = \sum_{j=1}^{N_1} C_{-j}g_{-j}(\pm\mu_i{}^{a})e^{k_j{}^{a}\tau} + \sum_{j=1}^{N_1} C_j g_j(\pm\mu_i{}^{a})e^{-k_j{}^{a}\tau} + Z_0(\pm\mu_i{}^{a})e^{-\frac{\tau}{\mu_{i_o}}} + Z_{01}(\pm\mu_i{}^{a})e^{\frac{\tau}{\mu_{i_o}}} \quad \text{(C.24)}$$

we have

$$I^{-}{}_{air}(\tau,\mu^{a})(\mu^{a}=\mu_i{}^{a}) = I^{-}(\tau,\mu_i{}^{a}) - I^{-}(\tau_0,\mu_i{}^{a})e^{-\frac{(\tau-\tau_0)}{\mu_i{}^{a}}} \quad \text{(C.25)}$$

Substituting Eq. (C.25) into Eq. (C.20) at quadrature points, finally we have

$$I^{-}(\tau,\mu_i{}^{a}) = I^{-}(\tau,\mu_i{}^{a}) \quad \text{(C.26)}$$

Thus this proves that the downward radiance expressions in the atmosphere derived using the iteration of source function is identical to the solution at quadrature points.

C.2.2 $\tau_b \geq \tau \geq {\tau_a}^+$, i.e. , in the ocean

We have obtained

$$I^-(\tau,\mu) = I^-({\tau_a}^+,\mu^o)e^{({\tau_a}^+/\mu^o-\tau/\mu^o)} + \sum_{j=-N_2}^{N_2} \frac{C_j\tilde{g}_j(-\mu^o)}{(1-{k_j}^o\mu^o)}\{e^{-{k_j}^o\tau} - e^{-\left[{k_j}^o{\tau_a}^+ + \frac{(\tau-{\tau_a}^+)}{\mu^o}\right]}\} \tag{C.27}$$

where $I^-({\tau_a}^+,\mu^o)$ is determined by the boundary conditions.

To evaluate at quadrature points, we have

$$\begin{aligned} I^-(\tau,\mu^o)(\mu^o={\mu_i}^o) &= I^-({\tau_a}^+,{\mu_i}^o)e^{({\tau_a}^+/{\mu_i}^o-\tau/{\mu_i}^o)} \\ &\quad + \sum_{j=-N_2}^{N_2} \frac{C_j\tilde{g}_j(-{\mu_i}^o)}{(1-{k_j}^o{\mu_i}^o)}\{e^{-{k_j}^o\tau} - e^{-\left[{k_j}^o{\tau_a}^+ + \frac{(\tau-{\tau_a}^+)}{{\mu_1}^o}\right]}\} \end{aligned} \tag{C.28}$$

Substituting Eqs. (C.1) $\sim$ (C.3) into the above expression, we have

$$\begin{aligned} I^-(\tau,\mu^o)(\mu^o={\mu_i}^o) &= I^-({\tau_a}^+,{\mu_i}^o)e^{({\tau_a}^+/{\mu_i}^o-\tau/{\mu_i}^o)} \\ &\quad + \sum_{j=-N_2}^{N_2} C_j g_j(-{\mu_i}^o)\{e^{-{k_j}^o\tau} - e^{-\left[{k_j}^o{\tau_a}^+ + \frac{(\tau-{\tau_a}^+)}{{\mu_i}^o}\right]}\} \end{aligned} \tag{C.29}$$

According to expressions of the radiance at quadrature points [63, 64], i.e.,

$$\begin{aligned} I^{\pm}(\tau,{\mu_i}^o) &= \sum_{j=1}^{N_2} C_{-j}g_{-j}(\pm{\mu_i}^o)e^{{k_j}^o\tau} \\ &\quad + \sum_{j=1}^{N_2} C_j g_j(\pm{\mu_i}^o)e^{-{k_j}^o\tau} + Z_{02}(\pm{\mu_i}^o)e^{-\frac{\tau}{\mu_{om}}} \end{aligned} \tag{C.30}$$

By combining all of these expressions we obtain

$$I^-(\tau,{\mu_i}^a) = I^-(\tau,{\mu_i}^a) \tag{C.31}$$

Thus this proves that the downward radiance expressions in the ocean derived using the iteration of source function is identical to the solution at quadrature points.

Appendix D

Description of the Monte Carlo model

The Monte Carlo (MC) code calculates the path for each photon, one by one, throught the coupled atmosphere-ocean system. In every situation where there is more than one possible outcome, the MC code generates a random number ρ uniformily distributed on the interval [0,1], this random number decides the outcome. When calculating the sum of all photons we get a picture of the energy flow throught the system. In this description the Greek letter ρ will always be a new generated random number.

The program sets up the IOPs such as absorption coefficient a, scattering coefficient b, Henyey-Greenstein asymetry factor g, Rayleigh polarization factor p, the ratio between Rayleigh and Henyey-Greenstein scattering η, and the medium M for each horizontal layer in the system.

A photon starts at the top of the atmosphere. Here it is given a position *(x,y,z)* and a direction of propagation $(\Omega_x, \Omega_y, \Omega_z)$. Next is to decide how far the photon

will travels before an extinction event occurs. The path length pl is found by

$$pl = -\frac{\ln \rho}{c_1}, \tag{D.1}$$

where $c_1 = a_1 + b_1$ is the extinction coefficient in layer 1. The photon may now have crossed one or several intersetion levels. Therefore it is necessary to calculate the position where it crossed the first intersection by reverse raytracing. Now we must find out of how much of the initial path length pl that is "consumed". We call the remaining part *plrest*. Since the photon now enters a new medium, we have to change the remaining path length

$$pl = plrest\,\frac{c_1}{c_2},$$

before it continues into the next layer, see the Fig. D.1. This process continues until the inital path length is "consumed". Then the single scattering albedo $\omega_0 = b/c$ decides whether the photon is absorb or scattered.

$$\rho \leq \omega_0 \Rightarrow \text{ scattering}$$

$$\rho > \omega_0 \Rightarrow \text{ absorption.}$$

If the photon is absorbed it is "dead" and we start all over again with the next photon. If it is scattered the number $\eta = b_{ray} \;/\; (b_{HG} + b_{ray})$ decides which kind of scattering that will occur.

$$\rho \leq \eta \Rightarrow \text{ Rayleigh}$$

$$\rho > \eta \Rightarrow \text{ HG.}$$

When a scattering event occurs the code calculate two angles: the polar scattering angle θ and the azimuth angle ϕ. For both HG and rayleigh scattering the azimuth angle is

$$\phi = 2\pi\rho.$$

The polar angle for HG scattering is found by

$$x = \frac{1+g^2}{2g} - \frac{(1-g^2)^2}{2g(2g\rho+1-g)^2},$$

where $x = \cos\theta$. The polar angle for rayleigh scattering is found by solving the following equation numerically:

$$px^3 + 3x + (3+p)(1-2\rho) = 0,$$

where$x = \cos\theta$ and p is the polarization factor. With the two angles (θ, ϕ) we calculate the new direction $(\Omega_x, \Omega_y, \Omega_z)$ for the photon. Now we have to use Eq. (D.1) to find new initial path length since the old one was all done.

If the photon crosses two layers where also the medium M changes, we have to calculate the reflection or refraction. First we calculate the direction of the normal vector $\hat{\mathbf{n}}$ of the surface. Then we need two angles, the angle between the normal vector and z-axis which we call β fig. D.2 and the azimuth angle α. By using the formula proposed by Cox and Munk we find:

$$\alpha = 2\pi\rho$$

$$\beta = \tan^{-1}(\sqrt{-\sigma^2 \ln\rho}),$$

where $\sigma^2 = 0.003 + 0.00512V$ and V is the wind speed in any direction. Note that even $V = 0$ gives some surface waves, so to compare with DISORT the normal vector is set parallel to the z-axis. Use Snell's law to find the refracted angle θ_t from the incident angle θ_i. Then the reflection coefficient is found

$$R = \frac{1}{2}\left(\frac{\sin^2(\theta_i - \theta_t)}{\sin^2(\theta_i + \theta_t)} + \frac{\tan^2(\theta_i - \theta_t)}{\tan^2(\theta_i + \theta_t)}\right).$$

R decides if there are going to be a refraction.

$$\rho \leq R \Rightarrow \text{ Reflection}$$

$$\rho > R \Rightarrow \text{ Transmittion}$$

Finally the code calculates the new direction for the photon.

To get some useful output we need to detect the photons somewhere. It is done at every intersection level. The irradiance is proportional to the number of photons that crosses the intersection level while the scalar irradiance is proprtional to the weighted sum of the photons, where each photon has been weighted by the factor $(\cos\theta_i)^{-1}$ and θ_i is the angle of incident. Thus we get the irradiance on each intersection level throught the whole system. It is posible to improve the code so that it could compute radiance As well as irradiance but that is future work.

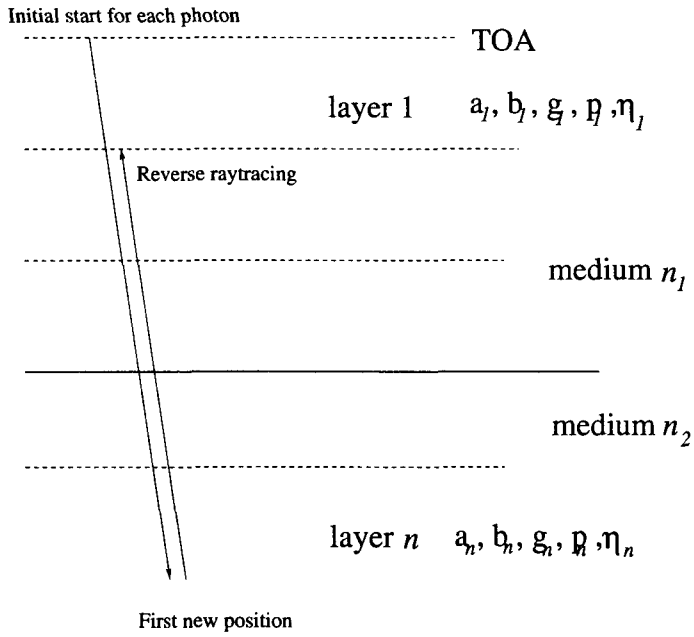

Figure D.1 Illustration of the atmosphere-ocean system..

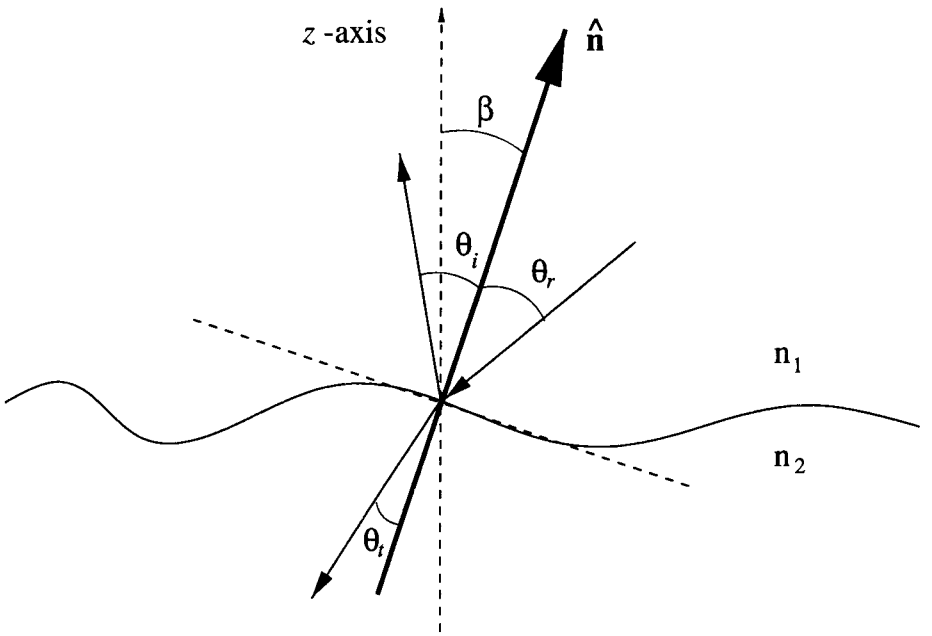

Figure D.2 Normal vector $\hat{\mathbf{n}}$ of a rough sea surface..

Bibliography

[1] Clarke, G. L., G. C. Ewing, and C. J. Lorenzen, Spectra of backscattered light from the sea obtained from aircraft as a measurement of chlorophyll concentration, Science, **33**, 167, 1119-1121 (1970).

[2] Gordon, H. R., D. K. Clark, J. L. Muller and W. A. Hovis, Phytoplankton pigments derived from the Nimbus-7 CZCS: initial comparisons with surface measurements, Science, **210**, 63-66 (1980).

[3] Hovis, W. A., D. K. Clark, F. Anderson, R. W. Austin, W. H. Wilson, E. T. Baker, D. Ball, H. R. Gordon, J. L. Muller, S. Y. E. Sayed, B. Strum, R. C. Wrigley and C. S. Yentsch, Nimbus 7 coastal zone color scanner: system description and initial imagery, Science, **210**, 60-63 (1980).

[4] Development of the coastal zone color scanner for Nimbus-7, vol. 2: Test and performance data, Final report, rev. A, NASA contract NAS5-20900, Rep. F78-11, pages 2-22, Ball Aerospace Division, Boulder, Colorado (1979).

[5] Evans, R. H. and H. R. Gordon, CZCS System Calibration: a retrospective examination, J. Geophys. Res., **99**, 7293-7307 (1994).

[6] Gordon, H. R., MODIS Normalized Water-leaving Radiance Algorithm Theoretical Basis Document, Version **3**, NASA (1996).

[7] Morel, A., and L. Prieur, Analysis of variations in ocean color, Limnol. Oceanogr., **22**, 709-722(1977).

[8] Morel, A. Optical modeling of the upper ocean in relation to its biogenous matter content (case 1 waters), J. Geophys. Res., **93**, 10,749-10,768 (1988).

[9] Shettle, E. P. and R. W. Fenn, Models for the Aerosols of the Lower Atmosphere and the Effects of Humidity Variations on their Optical Properties (Air Force Geophysics Laboratory, Hanscomb AFB, MA 01731) (1979).

[10] Yan, B., K. Stamnes and B. Chen, A generalized algorithm for the atmospheric correction of the ocean color imagery: feasibility simulation, Spring meeting of American Geophysical Union, S67 (1999).

[11] Gordon, H. R., T. Du, and T. Zhang, Remote sensing of ocean color and aerosol properties: resolving the issue of aerosol absorption, Appl. Opt., **36**, 8670-8684 (1997).

[12] Antoine, D. and A. Morel, Relative importance of multiple scattering by air molecules and aerosols in forming the atmospheric path radiance in the visible and near-infrared parts of the spectrum, App. Opt., **37**,2245-2259 (1998).

[13] Antoine, D. and A. Morel, A multiple scattering algorithm for atmospheric correction of remotely sensing ocean color (MERIS instrument): principle and implementation for atmospheres carrying various aerosols including absorbing ones, INT. J. Remote Sensing, **20**, 1875-1916 (1999).

[14] Morel, A., K. J. Voss, and B. Gentili, Bidirectional reflectance of oceanic waters: a comparison of modeled and measured upward radiance fields, J. Geophys. Res., **100**, 13,143-13,150 (1995).

[15] Chen, B., K. Stamnes, B. Yan, Ø. Frette, and J. J. Stamnes, Water-leaving radiance in the NIR spectral region and its effects on atmospheric correction of ocean color imagery, J. Adv. Mar. TSi. Tech. Soci. **4**, 329-338 (1998).

[16] Siegel, D. A., M. Wang, S. Maritorena, and W. Robinson, Atmospheric correction of satellite ocean color imagery: the black pixel assumption, Appl. Opt. **39**, 3582-3591 (2000).

[17] Gordon, H. R., O. B. Brown, and M. M. Jacobs, Computed relationships between the inherent and apparent optical properties of a flat homogeneous ocean, Appl. Opt., **14**, 417-427 (1975).

[18] Gordon, H.R., Ocean color remote sensing: Influence of the particle phase function and the solar zenith angle, EOS Trans. AGU, **14**, 1055 (1986).

[19] Gordon, H. R., O. B. Brown, R. H. Evens, J, W. Brown, R. C. Smith, K. S. Baker, D. K. Clark, A semianalytic radiance model of ocean color, J. Geophys. Res., **93**, 10,909-10,924 (1988b).

[20] Mobley, C. D., B. Gentili, H. R. Gordon, Z. Jin, G. W. Kattawar, A. Morel, P. Reinersman, K. Stamnes, and R. H. Stavn, Comparison of numerical models for computing underwater light fields, Appl. Opt., **32**, 7484-7504 (1993).

[21] Mobley, C. D., Light and water: radiative transfer in natural waters, Academic Press, San Diego, California (1994).

[22] Fraser, R. S., S. Mattoo, E.-N. Yeh, and C. R. McClain, Algorithm for atmospheric and glint corrections of satellite measurements of ocean pigment, J. Geophys. Res., **102**, 17107-17118 (1997).

[23] Gao, B.-C., M. J. Montes, Z. Ahmad, and C. O. Davis, Atmospheric correction algorithm for hyperspectral remote sensing of ocean color from space, Appl. Opt., **39**, 887-896 (2000).

[24] Tsay, S.-C., and G. L. Stephens, A physical/optical model for atmospheric aerosols with application to visibility problems, ISSN 0737-5352-16 (1990).

[25] d'Almeida, G. A., P. Koepke, E. P. Shettle, Atmospheric aerosols: global climatology and radiative characteristics, A. Deepak Publishing, (1991).

[26] Hale, G. M., M. R. Query, Optical constants of water in the 200-nm to 200-μm wavelength region, Appl. Opt., **12**, 555-563 (1973).

[27] Palmer, K. F., D. W. Williams, Optical properties of water in the near infrared, J. Opt. Soc. Amer., **64**, 1,107-1,110 (1974).

[28] Smith, R. C., K. S. Baker, Optical properties of the clearest natural waters, Appl. Opt., **20**, 177-184(1981).

[29] Gordon, H. R. , A. Y. Morel, Remote assessment of ocean color for interpretation of satellite visible imagery: a review, Spring-Verlag, New York, 114 pp (1983).

[30] Morel, A., Chlorophyll-specific scattering coefficient of phytoplankton- a simplified theoretical approach, Deep-Sea Res., Part A **34**, 1,093-1,105 (1987).

[31] Morel, A. and S. Maritorena, Bio-optical properties of oceanic waters: A reappraisal, J. Geophys. Res., **106**, 7163-7180 (2001).

[32] Garver, S. A., D. A. Siegel, Inherent optical property inversion of ocean color spectra and its biogeochemical interpretation: I.Time series from the Sargasso Sea, J. Geophys. Res., **102**, 18,607-18,625 (1997).

[33] Carder, K. L., F. R. Chen, Z. P. Lee, S. K. Hawes, D. Kamykowski, Semianalytic Moderate-Resolution Imaging Spectrometer algorithms for chlorophyll a and absorption with bio-optical domains based on nitrate-depletion temperatures, J. Geophys. Res., **104**, 5,403-5,421 (1999).

[34] Gordon, H. R. and A. Y. Morel, Remote assessment of ocean color for interpretation of satellite visible imagery: a review. Springer-Verlag, New York Inc (1983).

[35] Zaneveld, J. R. V., Remotely sensed reflectance and its dependence on the vertical structure: a theoretical derivation, Appl. Opt., **21**, 4146-4150 (1982).

[36] Zaneveld, J. R. V., A theoretical derivature of the dependence of the remotely sensed reflectance of the ocean on the inherent optical properties, J. Geophys. Res., **100**, 13,135-13,142 (1995).

[37] Medwin, H., In situ acoustic measurements of bubble populations in coastal ocean waters, J. Geophys. Res., **75**, 599-611 (1970).

[38] Johnson, B. D., and R. C. Cooke, Bubble populations and spectra in coastal waters: A photographic approach, J. Geophys. Res. **84**, 3761-3766 (1979).

[39] Walsh, A. L. and P. J. Mulhearn, Photographic measurements of bubble populations from breaking wind waves at sea, J. Geophys. Res., **92**, 14553-14565 (1987).

[40] O'Hearn, T. J., L. d'Agostino, and A. J. Acosta, Comparison of holographic and coulter counter measurement of cavitation nuclei in the ocean, Transactions of the ASME, J. Fluids Eng., **110**, 200-207 (1988).

[41] Medwin, H. and N. D. Breitz, Ambient and transient bubble spectral densities in quiescent seas and under spilling breakers, J. Geophys. Res., **94**, 12751-12759 (1989).

[42] Bukata, R. P., Optical Properties and Remote Sensing of Inland and Coastal Waters, CRC Press, Boca Raton, Fla. (1995).

[43] Stramski, D., Gas microbubbles: An assessment of their significance to light scattering in quiescent seas, SPIE **2258**, Ocean Optics XII, 704-710 (1994).

[44] Zhang, X., and M. Lewis, Scattering of light of bubbles and its effect on remote sensing, Proceedings of The 4th Pacific Ocean Remote Sensing Conference (PORSEC98, July 28-31, 1998, Qingdao, China), 167-171 (1998).

[45] Zhang, X. , M. Lewis, and B. Johnson, Influence of bubbles on scattering of light in the ocean, Appl. Opt. **37**, 6525-6536 (1998).

[46] Flatau, P. J., M. Flatau, J. R. Zaneveld, and C. D. Mobley, Remote sensing of bubble clouds in seawater, Quarterly Journal of the Royal Meteorological Society **126**, 2511-2524 (2000).

[47] Chandrasekhar, S., Radiative transfer, Dover, New York (1960).

[48] Devaux, C., Grandjean, P., Ishiguro, Y. and C. E. Siewert, On Multi-Region Problems in Radiative Transfer, Astrophys. Space Sci., **62**, 225-233 (1979).

[49] Garcia, R. D. M. and C. E. Siewert, Benchmark Results in Radiative Transfer, Transport Theory and Statistical Physics, **14**, 437-483 (1985).

[50] Lenoble, J., ed., Radiative Transfer in Absorbing and Scattering Atmospheres: Standard Computational Procedures, Deepak Publishing, Hampton, Virginia (1985).

[51] Nakajima, T. and M. Tanaka, Algorithms for Radiative Intensity Calculations in Moderately Thick Atmospheres Using a Truncation Approximation, J.Q.S.R.T., **40**, 51-69 (1988).

[52] Ozisik, M. and S. Shouman, Source Function Expansion Method for Radiative Transfer in a Two-Layer Slab, J.Q.S.R.T., **24**, 441-449 (1980).

[53] Stamnes, K. and R. Swanson, A New Look at the Discrete Ordinate Method for Radiative Transfer Calculations in Anisotropically Scattering Atmospheres, J. Atmos. Sci., **38**, 387-399 (1981).

[54] Stamnes, K. and H. Dale, A New Look at the Discrete Ordinate Method for Radiative Transfer Calculations in Anisotropically Scattering Atmospheres. II: Intensity Computations, J. Atmos. Sci., **38**, 2696-2706 (1981).

[55] Stamnes, K., On the Computation of Angular Distributions of Radiation in Planetary Atmospheres, J.Q.S.R.T., **28**, 47-51 (1982).

[56] Stamnes, K., Reflection and Transmission by a Vertically Inhomogeneous Planetary Atmosphere, Planet Space Science, **30**, 727-732 (1982).

[57] Stamnes, K. and P. Conklin, A New Multi-Layer Discrete Ordinate Approach to Radiative Transfer in Vertically Inhomogeneous Atmospheres, J.Q.S.R.T., **31**, 273-282 (1984).

[58] Sweigart, A., Radiative Transfer in Atmospheres Scattering According to the Rayleigh Phase Function with Absorption, The Astrophysical Journal Supplement Series, **22**, 1-80 (1970).

[59] Van de Hulst, H.C., Multiple Light Scattering, Tables, Formulas and Applications, **1 and 2**, Academic Press, New York (1980).

[60] Wiscombe, W., The Delta-M Method: Rapid Yet Accurate Radiative Flux Calculations, J. Atmos. Sci., **34**, 1408-1422 (1977).

[61] Stamnes, K., S.-C. Tsay, W. Wiscombe and K. Jayaweera, A Numerically Stable Algorithm for Discrete-Ordinate-Method Radiative Transfer in Multiple Scattering and Emitting Layered Media, Appl. Opt., **27**, 2502-2509 (1988).

[62] Stamnes, K., S.-C. Tsay, W. J. Wiscombe and I. Laszlo, DISORT, a General-Purpose Fortran Program for Discrete-Ordinate-Method Radiative Transfer in Scattering and Emitting Layered Media: Documentation of Methodology, Report, available from ftp://climate.gsfc.nasa.gov/pub/wiscombe/Multiple Scatt/, 2000.

[63] Jin, Z. and K. Stamnes, Radiative transfer in nonuniformly refracting layered media: atmosphere-ocean system, Appl. Opt., **33**, 431-442 (1994).

[64] Thomas, G. E., and K. Stamnes, Radiative Transfer in the Atmosphere and Ocean, Cambridge University Press, New York (1999).

[65] Schulz, F. M. and K. Stamnes, Angular distribution of the Stokes vector in a plane-parallel vertically inhomogeneous medium in the vector discrete ordinate radiative transfer (VDISORT) model, J.Q.S.R.T., **65**, 609-620 (2000)

[66] Elterman, L., UV, Visible, and IR attenuation for altitude to 50 km, AFCRL-68-0153, Bedford, MA, Air Force Cambridge Res. Lab (1968).

[67] Morel, A., and B. Gentili, Diffuse reflectance of oceanic waters: its dependence on sun angle as influenced by the molecular scattering contribution, Appl. Opt., **30**, 4427-4438 (1991).

[68] Morel, A., Optical properties of pure water and pure sea water, Optical Aspects of Oceanography, N. G. Jerlov and E. S. Nielsen, eds., Academic, New York, 1-24 (1974).

[69] Gordon, H. R. and M. Wang, Retrieval of water-leaving radiance and aerosol optical thickness over the oceans with SeaWiFS: A preliminary algorithm, Appl. Opt., **33**, 443-452 (1994).

[70] Gordon, H. R., Atmospheric correction of ocean color imagery in the Earth Observation System era, J. Geophys. Res., **102**, 17081-17106 (1997).

[71] Muller, J., C. McClain, R. Caddrey, G. Feldman, The NASA SIMBIOS Program, Backscatter, 29-32 (1998).

[72] Bricaud, A., A. Morel, M. Babin, K. Allali, H. Claustre, Variations of light absorption by suspended particles with chlorophyll a concentration in oceanic (case 1) water: Analysis and implications for bio-optical models, J. Geophys. Res., **103**, 31,033-31,044 (1998).

[73] Smith, R. C., and K. S. Baker, The analysis of ocean optical data II, Proc. SPIE Int. Soc. Opt. Eng., **637**, 95-107 (1984).

[74] Muller, J. L., Comparison of irradiance immersion coefficients for several marine environmental radiometers (MERs), in Case Studies for SeaWiFS Calibration and Validation, Part 3, **27**, NASA Tech. Memo., 104566-194610 (1995).

[75] Austin, R. W., and G. Halikas, The index of refraction of seawater, 121 pp., Scripps Institute Of Oceanography, La Jolla, California (1976).

[76] Dierssen, H. M. and R. C. Smith, Bio-optical properties and remote sensing ocean color algorithms for Antarctic Peninsula waters, J. Geophys. Res., **105**, 26,301-26,312 (2000).

[77] Petzold, T., Volume scattering functions fro selected ocean waters, SIO Ref. 72-78 (Scripps Institute of Oceanography, La Jolla, Calif.) (1792).

[78] Volten, H., J. F. de Haan, J. W. Hovenier, R. Schreurs, W. Vassen, A. G. Dekker, H. J. Hoogenboom, F. Charlton, and R. Wouts, Laboratory measurements of angular distributions of light scattered by phytoplankton and silt. Limnol. Oceanogr., **43**, 1180-1197 (1998).

[79] Morel, A., Optical modeling of the upper ocean in relation to its biogenous matter content (case 1 waters), J. Geophys. Res., **93**, 10,749-10,768 (1988).

[80] Ciotti, A. M., J. J. Cullen, and M. R. Lewis, A semi-analytical model of the influence of planktone community structure on the relationship between light attenuation and ocean color, J. Geophys. Res., **104**, 1559-1578 (1999).

[81] O'Reilly, J. E., Maritorena, S., Mitchell, B. G., Siegel, D. A., Carder, K. L., Garver, S. A., Kahru, M., McClain, C., Ocean color chlorophyll algorithms for SeaWiFS. Journal of Geophysical Research-Oceans, **103**, 24937-24953 (1998).

[82] Pegau, W. S., D. Gray J. R. V. Zaneveld, Absorption and attenuation of visible and near-infrared light in water: dependence on temperature and salinity, Appl. Opt., **36**, 6,035-6,046 (1997).

[83] Sydor, M., R. A. Arnone, Effect of suspended particulate and dissolved organic matter on remote sensing of coastal and riverine waters, Appl. Opt., **36**, 6,905-6,912 (1997).

[84] Gould, R.W., R. A. Arnone, P. M. Martinolich, Spectral dependence of the scattering coefficient in case 1 and case 2 waters, Appl. Opt., **38**, 2,377-2,383 (1999).

[85] Fox, F. E. and K. Herzfeld, Gas bubbles with organic skin as cavitation nuclei, J. Acoust. Soc. Am. **26**, 984-989 (1954).

[86] Yount, D. E., Skins of varying permeability: a microscopic investigation of bubble formation nuclei, J. Acoust. Soc. Am., **76**, 1511-1521 (1984).

[87] Mulhearn, P. J., Distribution of microbubbles in coastal waters, J. Geophys. Res., **86**, 6429-6434 (1981).

[88] Wu, J., Bubble populations and spectra in near-surface ocean: summary and review of field measurements, J. Geophys. Res., **86**, 457-463 (1981).

[89] Glazman, R. E., Effects of absorbed films on gas bubble radial oscillations, J. Acoust. Soc. Am., **74**, 980-986 (1983).

[90] Thorpe, S. A., The effect of langmuir circulation on the distribution of submerged bubbles caused by breaking wind waves, J. Fluid Mech., **14**, 151-170 (1984).

[91] Yount, D. E., E. W. Gillary, and D. C. Hoffman, A microscopic investigation of bubbles formation nuclei, J. Acoust. Soc. Am., **76**, 1511-1521 (1984).

[92] Johnson, B. D. and P. J. Wangersky, Microbubbles: stabilization by monolayers of adsorbed particles, J. Geophys. Res., **92**, 14641-14647 (1987).

[93] Baldy, S., Bubbles in the close vicinity of breaking waves: statistical characteristics of the generation and dispersion mechanism, J. Geophys. Res., **93**, 8239-8248 (1988).

[94] Wu, J., Bubbles in the near-surface ocean: a general description, J. Geophys. Res., **93**, 587-590 (1988).

[95] Isao, K., S. Hara, K. Terauchi, and K. Kogure, Role of sub-micrometer particles in the ocean, Nature, **345**, 242-244 (1990).

[96] King, M. D., L. F. Radke, and P. V. Hobbs, Optical properties of marine stratocumulus clouds modified by ships, J. Geophys. Res., **98**, 2729-2739 (1993).

[97] Prieur, L., and S. Sathyendranath, An optical classification of coastal and oceanic water based on the specific spectral absorption curves of phytoplankton pigments, dissolved organic matter, and other particulate materials, Limnol. Oceanogr., **26**, 671-689 (1981).

[98] Prieur, L., S. Sathyendranath, and A. Morel, A three-component model of ocean color and its application to remote sensing of phytoplankton pigments in coastal waters, Int. J. Remote Sensing, **10**, 1373-1394 (1989).

[99] Villevalde, Y. V., A. V. Smirnov, N. T. O'Neill, S. P. Smyshlyaev, and V. V. Yakovlev, Measurement of aerosol optical depth in the Pacific ocean and north Atlantic, J. Geophys. Res., **99**, 20983-20988 (1994).

[100] Schwindling, M., P. Deschamps, and R. Frouin, Verification of aerosol models for satellite ocean color remote sensing, J. Geophys. Res., **103**, 24919-24935 (1998).

[101] Heintzenberg, J., Light scattering parameters of internal and external mixtures of soot and non- absorbing material in atmospheric aerosols, Conference on Carbonaceous Particles in the Atmosphere, Berkeley, CA, 278-281 (1978).

[102] Chylek, P. and J. Wong, Effect of Absorbing Aerosol on Global radiation Budget, Geophys. Res. Lett., **22**, 929-931 (1995).

[103] Hanel, G., The properties of atmospheric aerosol particles as functions of the relative humidity at thermodynamic equilibrium with the surrounding moist

air, Advances in Geophysics (Edited by H. E. Landsberg and J. Van Mieghem, Academic Press, New Work), **19**, 73-188 (1976).

[104] Wulfmeyer, V., and G. Feingold, On the relationship between relative humidity and particle backscattering coefficient in the marine boundary layer determined with differential absorption lidar, J. Geophys. Res., **105**, 4729-4741 (2000).

[105] Fenn, R. W., Aerosol-Verteilungen und atmospharisches Streulicht, Beitr. Physik Atmos., **37**, 69-104 (1964).

[106] Whitby, K. T., R. B. Husar, and B. Y. H. Liu, The aerosol size distribution of Los Angles smog, J. Colloid Sci., **39**, 177-204 (1972).

[107] Whitby, K. T., W. E. Clark, V. A. Marple, G. M. Sverdrup, G. J. Sem, K. Willeke, B. Y. H. Liu, and D. Y. H. Pui, Characterization of California aerosols: I. Size distributions of Freeway aerosol, Atmos. Environ., **9**, 463-482 (1975).

[108] Willeke, K., K. T. Whitby, W. E. Clark, and V. A. Marple, Size distributions of Denver aerosols: A comparison of two sites, Atmos. Environ., **8**, 609-633 (1974).

[109] J. T. Twitty, R. J. Parent, J. A. Weinman, and E. W. Eloranta, Aerosol size distributions: Remote determination from airborne measurements of the solar aureole, Appl. Opt., **15**, 980-989 (1976).

[110] Harris, F. S., Jr. and M. P. McCormick, Mie scattering by three polydispersions, J. Colloid Sci., **39**, 536-545 (1972).

[111] Davies, C. N., Size distribution of atmospheric particles, J. Aerosol Sci., **5**, 293-300 (1974).

[112] Whitby, K. T., and B. Cantrell, Atmospheric aerosols - Characteristics and measurements, International Conf. on Environmental Sensing and Assessment, **2**, Las Vegas, Nevada, 14-19 (1975).

[113] Hanel, G. and M. Lehmann, Equilibrium size of aerosol particles and relative humidity: New experimental data from various aerosol types and their treatment for cloud physics application, Contr. Atmos. Phys., **54**, 57-71 (1981).

[114] Nair, P. V. N., and K. G. Vohra, Growth of aqueous sulfuric acid droplets as function of relative humidity, J. Aerosol Sci., **6**, 265-271 (1975).

[115] Sasano, Y., and E. V. Browell, Light scattering characteristics of various aerosol types derived from multiple wavelength lidar observations, Appl. Opt., **28**, 1670-1679 (1989).

[116] Yue, G. K., J. Lu, V. A. Mohnen, P.-H. Wang, V. K. Saxena, and J. Anderson, Retrieving aerosol optical properties from moments of the particle size distribution, Geophys. Res. Lett., **24**, 651-654, (1997).

[117] Quinn, P. K., T. S. Bates, T. L. Miller, D. J. Coffman, J. E. Johnson, J. M. Harris, J. A. Ogren, G. Forbes, T. L. Anderson, D. S. Covert, and M. J. Rood, Surface submicron aerosol chemical composition: What fraction is not sulfate? J. Geophys. Res., **105**, 6785-6805 (2000).

[118] Chiapello, I., G. Bergametti, B. Chatenet, F. Dulac, I. Jankowiak, C. Liousse, and E. S. Soares, Contribution of the different aerosol species to the aerosol mass load and optical depth over the northeastern tropical Atlantic, J. Geophys. Res., **104**, 4025-4035 (1999).